1. Introduction

The ocean covers approximately 71% of the earth surface and it significantly influences the global and regional climates and the weather and monsoon systems. Climate variability and its socio-economic impact clearly emphasizes the need to understand the system to enable better forecasts. Unlike land, where the operational networks of meteorological observations placed all over the world have enabled us to monitor changes in the global atmosphere, the global coverage of the subsurface observations in the ocean is largely under sampled. With the advent of Argo and moored buoy programs, there was a considerable increase in the amount of oceanic data during the last decade. However, the data is still inadequate to understand the dynamics and thermodynamics of the ocean on different spatial and temporal scale. Besides under-sampling, two additional limitations of the historical observational data set complicate the studies of ocean physics variability on inter-annual to decadal time scales. The first is due to changes in the observation bias resulting from the evolution of the observing system. The second limitation is due to changes in the vertical sampling of the historical temperature data set [*Carton and Santorelli,* 2008]. These limitations demand the importance of ocean modelling. Ocean modelling can provide a unique opportunity to understand the past and existing climatic conditions and to predict future climate changes. Hence a number of efforts have been initiated in recent years to apply data assimilation techniques to produce reanalysis data using a state of the art ocean general circulation model (OGCM). These data can be used to understand the physical state of the ocean (temperature, salinity, currents, sea level) on seasonal to decadal time scales.

At present several operational agencies around the world provide seasonal forecasting, which requires near-real-time knowledge of the ocean state. Seasonal forecasting systems are based on coupled ocean-atmosphere general circulation models that predict sea surface temperature (SST) and their impact on atmospheric circulation. Ultimately, the aim of seasonal forecasts is to predict climate anomalies about one or two seasons in advance. A

model that can skilfully predict future climate months and seasons ahead is a powerful tool to assist in planning and managing almost all socio-economic activities.

India is a country where the economy largely depends on agricultural production, which, in tern, is strongly dependent on the rainfall received over the Indian land mass during the summer monsoon months of June-September [*Rajeevan et al.,* 2008]. It is well known that the Indian summer monsoon rainfall shows large inter-annual variability both in terms of spatial distribution and intensity. A better forecast of the monsoon will aid the government in taking precautionary measures to tackle issues like deficits in food production, damage due to floods, etc. Therefore, the prediction of the interannual and seasonal variation of the Indian summer monsoon rainfall, particularly for the occurrence of extreme events like droughts and excessive rainfall is extremely important. However the skill of atmospheric and coupled models to predict the summer monsoon rainfall is not yet satisfactory [*Gadgil and Srinivasan,* 2011]. For example, almost all the model generated predictions by the leading centers in the world using general circulation models of the atmosphere or of the coupled ocean-atmosphere system did not anticipate the large deficit in rainfall during the summer monsoon of 2009 [*Nanjundiah,* 2009]. It is well known that the ocean SST plays a significant role in the modulation of the summer monsoon rainfall [*Shenoi et al.,* 2002*; Vecchi and Harison,* 2002*; Joseph et al.,* 2005*; Shankar et al.,* 2007*; Francis and Gadgil,* 2009]. In addition, earlier modelling studies also have highlighted the significance of better oceanic initial conditions, particularly with regard to the upper ocean thermal structure, for improving the skill of climate model forecasts at the seasonal time scale [*Balmaseda et al.,* 2009; *Balmaseda and Anderson,* 2009]. Any inaccuracy in the upper ocean thermal structure, particularly in the SST strongly influences the atmospheric circulation in the coupled model [*Balmaseda et al.,* 2009]. In addition [*Balmaseda and Anderson,* 2009] showed that ocean initialization has a significant impact on the mean state, variability, and skill of coupled forecasts at the seasonal time scale. It is well known that, model forcing fields (surface flux products and wind products) have

significant errors. These will inevitably lead to errors in the ocean model output. Data assimilation techniques are then used to improve the ocean state estimations. Hence the assimilation of ocean surface and subsurface data into a ocean general circulation model can improve the initial estimation of the ocean state, which in principle should improve the skill of seasonal forecasts.

To increase the understanding and predictive capability of the oceans role in future climate change scenarios, a new version of the Global Ocean Data Assimilation System (GODAS) has been developed at the National Centers for Environmental Prediction (NCEP). This new system is part of the new Climate Forecast System Reanalysis (CFSR) at NCEP [*Saha et al.,* 2010]. The GODAS has been configured at the Indian National Centre for Ocean Information Services (INCOIS) and two experiments have been performed. The details of the experiments will be discussed in section 3.

One of the important stages in building any hindcast/forecast system is to evaluate the model simulated parameters with independent *in situ* and satellite observations. The ultimate goal of validation of the model output is to determine to what extent the model is an accurate representation of the real system being modelled. The insights gained from model validation will be useful for the improvements of the model's ability to capture realistic scenarios and for establishing the limitations of a model.

Though the ocean parameters derived from the GODAS-MOM3 were validated for the IO by *Huang et al.* [2008] for the period 2001-2006, the newly developed GODAS based on MOM4p0 has not been validated, especially for the Indian Ocean (IO) region. This report aims to validate the GODAS simulations for the IO during the period of 2004-2009. The report is organised as follows: Section 2 describes the model configuration and assimilation scheme. Section 3 describes the model forcing fields and the experiments carried out with different wind products, NCEP2 and QuikSCAT. Section 4 describes the data sets used and the methodology employed for the validation. Section 5 describes the validation results for

different parameters obtained from the GODAS-MOM model output. Section 6 describes the dissemination procedure to get the ocean analysis products from the web GIS and LAS server. A summary of this report and future plans and recommendations are given in section7.

2. Model configuration, forcing field and assimilation system

2.1 The Ocean Model

The model which has been configured at INCOIS is the new version of the GODAS, which is based on the GFDL MOM4p0 with a 3DVAR data assimilation scheme. The MOM4p0 is fully global with an Arctic Ocean and an interactive ice model. The MOM4p0 is a hydrostatic, primitive equation, free surface, Boussinesq OGCM with z-coordinates in the vertical and generalized orthogonal horizontal coordinates. The model uses the tripolar grid developed by *Murray* [1996]. Northward of 65°N it uses a rotated bipolar grid that places two poles over land which eliminates the singularity in the northern ocean. Southward of 65°S it uses a regular latitude and longitude grid. The primitive equations are discretized on an Arakawa B-grid. The model domain is shown in Figure 2.1. The model has a uniform zonal resolution of 0.5°S and a variable meridional resolution of 0.25° within 10° of the equator, which decreases exponentially from 10°S (10°N) to 30°S (30°N) to maintain a 0.5 meridional resolution polewards from 30°S (30°N). There are 40 layers in the vertical with 27 layers in the upper 400 m, and the maximum bottom depth is approximately 4.5 km. The vertical resolution is 10 m from the surface to the 240 m depth and gradually increases to about 511 m in the bottom layer. The bathymetry is based on coarsened version of the topography data by Andrew Coward and David Webb at the Southampton Oceanography Centre [*Griffies et al.*, 2004]. Their topography is a montage of that developed by *Smith and Sandwell* [1997] using satellite data in the region of 72°S to 72°N, the *NOAA* [1988] 5-minute global topography ETOPO5 (Figure 2.1), and the International Bathymetric Chart of the Arctic Ocean (IBCAO).

Vertical mixing follows the nonlocal K-profile parameterization of *Large et al.* [1994]. The horizontal mixing of tracers uses the isoneutral method developed by *Gent and McWilliams* [1990] (see also *Griffies et al.* [1998]). The horizontal mixing of momentum uses the nonlinear scheme of *Smagorinsky* [1963] (see also *Griffies and Halberg,* [2000]). The baroclinic and barotropic time step of the model is 1800 s and 22.5 s respectively.

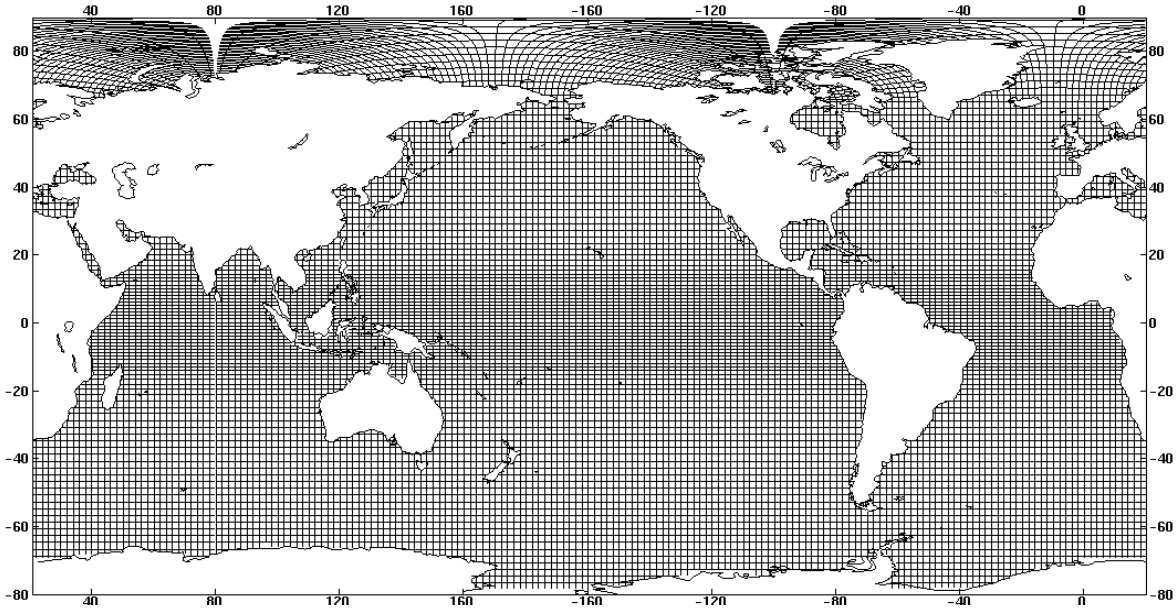

Figure 2.1. The schematic diagram of model domain and spatial grid resolution. The resolution of the grid is reduced by 4X for display. The resolution is 1/2° X 1/2° increasing to 1/2° X 1/4° within 10° of the equator. The grid is distorted in the Arctic.

2.2 Assimilation system

The GODAS uses a 3DVAR assimilation scheme, which was originally developed by *Derber and Rosati* [1989]. It was adopted for operational use at NCEP, where it has undergone further development to assimilate salinity profiles [*Behringer et al.,* 1998*; Huang et al*., 2008]. The functional to be minimized is

$$I = \frac{1}{2}\left(T^T E^{-1} T\right) + \frac{1}{2}\left\{\left[D(T) - T_0\right]^T F^{-1}\left[D(T) - T_0\right]\right\} \qquad (1)$$

where the vector T represents the correction to the first-guess prognostic tracers (temperature and salinity) computed by the model, E is the first-guess error covariance matrix,

T_0 represents the difference between the tracer observations and the first guess, *D* is an interpolation operator that transforms the first-guess tracers from the model grid to the observation locations, and *F* is the observation error covariance matrix for the tracers. In the present system, the first-guess error covariance matrix, E, is univariate and thus block diagonal with respect to temperature and salinity. The horizontal covariance is modelled as a Gaussian function that is stretched in the zonal direction with the stretching being greatest near the equator. The vertical covariance is also modelled as a Gaussian function with a scale that increases with depth as the model grid separation increases; near the surface, the scale is approximately 25 m. The estimated first-guess error variance is scaled by the square root of the local vertical temperature gradient computed from a previous model analysis. In the present study, the current 5 day analysis provides the data for estimating the first-guess error variance for the next 5 day analysis. The observational errors are assumed to be uncorrelated, so that *F* is a diagonal matrix of the estimated error variances of the observations

The errors assigned to a temperature profile vary with depth according to the square root of the vertical temperature gradient and are scaled to have values between 1^oC and 2.5^oC. The standard error assigned to a salinity profile is a constant 0.1 psu at all depths. Temperature and salinity profiles are assimilated at 6-hour intervals using all observations from the previous 10-day interval. The more distant a profile is in time, the less weight it receives in the assimilation. This approach allows relatively sparse ocean observations to have a greater impact on the model state [*Derber and Rosati,* 1989; *Behringer et al.,* 1998]. Upper 750 m depth (30 levels) temperature and salinity profiles from different in-situ ocean observational network (Research Moored Array for African-Asian-Australian Monsoon Analysis and predication (RAMA), TAO/TRITION, PIRATA moored buoys, XBTs, and ARGO) are being assimilated for the present study. It is worth mentioning here that, the number of temperature and salinity profiles assimilated in the model vary with time.

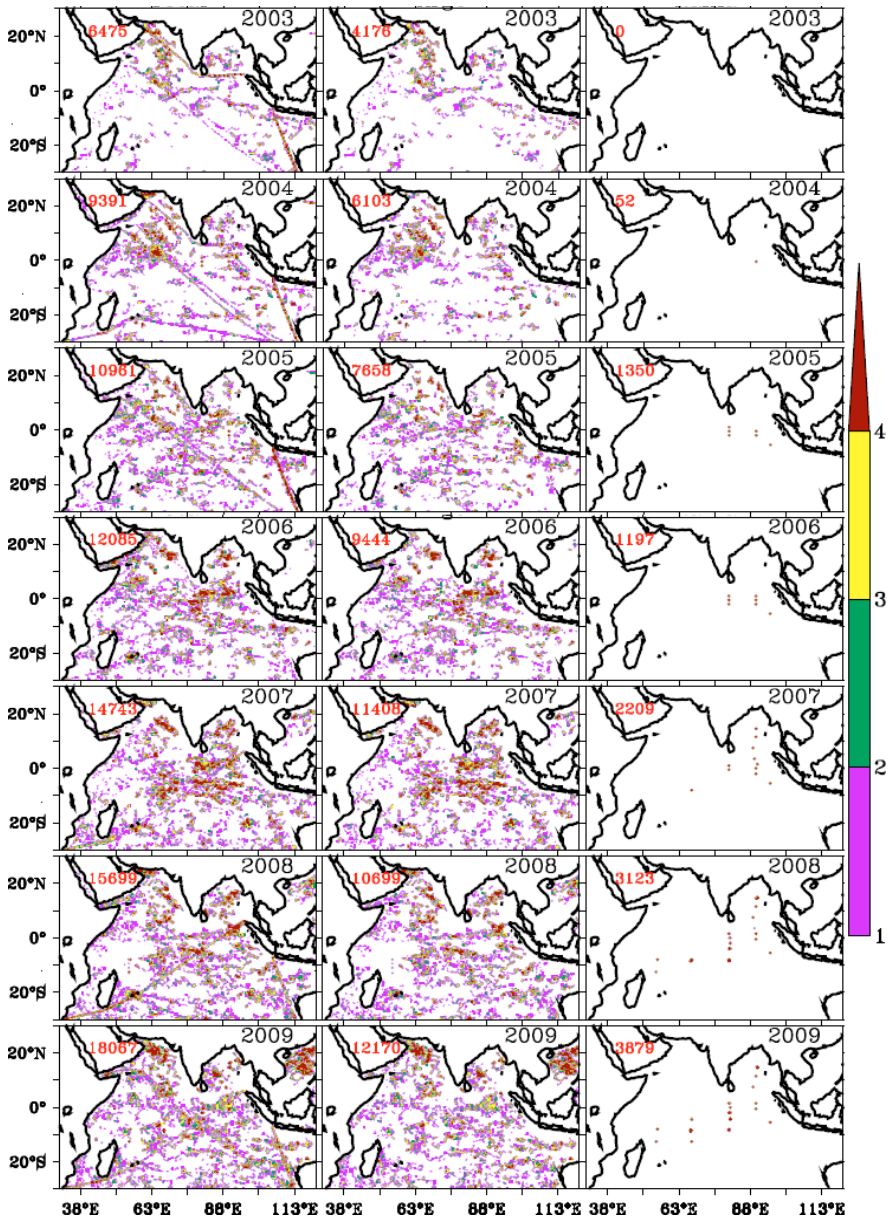

Figure 2.2. The yearly distribution of temperature profiles available in the IO for assimilation during the period 2004-2009. Total (ARGO+XBT+buoy) (left), ARGO (middle) and buoy (right). The total number of profiles available in the IO for assimilation is given in each panel. The colour bar indicates the number of profiles in 0.5° X 0.5° grid box.

GODAS salinity is not restored to climatology in the sense of Salinity(z), z is depth. Instead it assimilates synthetic salinity based on the local climatological temperature and salinity correlation and the observed Temperature(z). So, for each Temperature(z) observation there is a corresponding Salinity(z) = F(Temperature(z)), where F represents the local correlation. The objective is to conserve water mass properties. The Quality Control

(QC) code which preprocesses the input data for the GODAS generates the synthetic salinity profiles, taking observed temperature profile as input. For the top level of the model (5 m), the temperature analysis is strongly relaxed using daily optimally interpolated (OI) SST analysis [*Reynolds et al.,* 2007]. The purpose of using relaxation at the surface is to provide a strong constraint on the ocean at the interface with the atmosphere, and compensate for possible model drift due to errors in the surface heat and momentum fluxes.

Figure 2.2 shows the yearly distribution of temperature profiles available in the IO for assimilation during the period 2004-2009. The left panel shows the observation frequency distribution for total temperature profiles acquired from XBT, Argo and buoys. The middle and right panels show the observation frequency distributions for Argo and buoy temperature profiles assimilated into the model respectively.

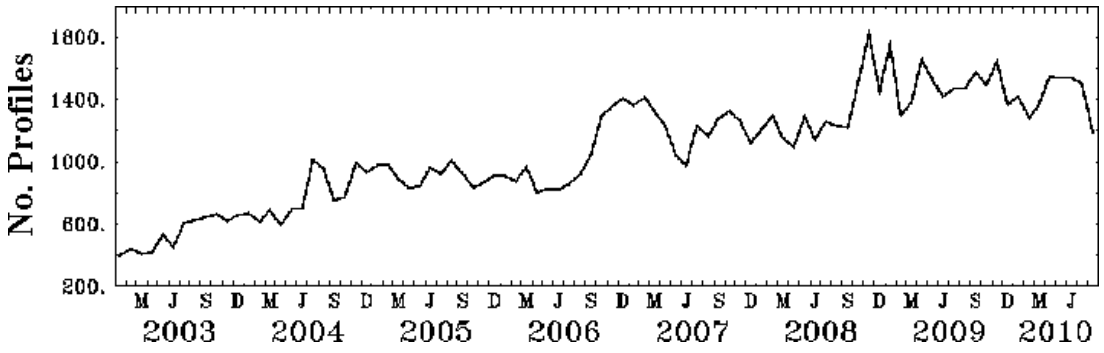

Figure 2.3. Monthly evolution of number of temperature profiles avilable for assimaltion in the IO during 2003-2009.

Figure 2.3 shows the monthly evolution of number of temperature profiles available in the IO during 2003-2009. It can be seen from the Figure 2.2 and 2.3 that in 2004 the sparse observations which went into the assimilation system has improved as time passes and reasonably good coverage is achieved in 2007. The total number of observations has increased almost two fold in 2009 as compared to that in 2004 (Figure 2.3)

3. Experiments Performed

3.1 NCEP Experiment

In the first experiment the GODAS-MOM is forced with NCEP2 heat, momentum and freshwater fluxes [*Kanamitsu et al.,* 2002]. This experiment performed for 2003-2009 using a ocean initial condition provided by NCEP, is denoted as the NCEP experiment (NCEPEXP). The NCEP2 precipitation and annual mean value of UNESCO River runoff [*Vörösmarty et al.,* 1996] has been used for freshwater forcing. The river runoff is distributed over several grid points at the surface. The river run-off mixing scheme uses the upper 40 m of the water column as the river incursion thickness. The chlorophyll concentration is used from monthly SeaWiFS climatology. The turbulent fluxes of sensible and latent heat, were calculated in the model using the COARE-bulk algorithm [*Fairall et al.,* 2003] with the NCEP2 wind speed, specific humidity and air temperature, and model sea surface temperature.

3.2 Quikscat EXP

The wind simulated by numerical weather prediction models has a relatively coarse resolution (~1.5 or 2°) and hence it can capture only large scale features of the wind field over the world ocean, missing small scale features [*Chelton et al.,* 2004]. High-resolution measurements by the QuikSCAT scatterometer reveal a rich diversity of persistent small-scale features in the global wind stress field that cannot be detected by other means [*Chelton et al.,* 2004]. In addition, earlier studies have shown that high resolution wind fields can significantly improve ocean general circulation model results, particularly with regard to the simulation of subsurface features, coastal currents and coastal upwelling processes [*Dong and Oey,* 2005*; Jiang et al.,* 2008]. In addition, earlier studies highlighted the importance of an accurate representation of the subsurface temperature in numerical models for better SST prediction [*Kang and Kug,* 2000].

Goswami and Sengupta [2003] have shown that the NCEP1 reanalysis surface winds are underestimated in the equatorial IO. Subsequently *Swain et al.* [2009] have shown that

NCEP2 winds also underestimated in the south Eastern Arabian Sea. *Agarwal et al.* [2008] assessed the quality of the wind speed products from QuikSCAT and NCEP in the IO using the National Institute of Ocean Technology (NIOT) buoy winds for comparison. Their study shows that compared to NCEP2, the QuikSCAT winds show relatively less error and larger correlations with buoy measured winds. *Sharma et al.* [2007] showed improvements in model current and salinity structures in the equatorial IO, when the model was forced by QuikScat winds instead of NCEP winds. Another important feature of satellite winds are their relatively high spatial resolution compared to the reanalysis product. *Agarwal et al.* [2008] evaluated the relative performance of QuikSCAT and NCEP re-analysis winds through simulations by an ocean general circulation model (MOM3) for the IO region. Their study showed considerable improvements in model simulations when they are forced with QuikSCAT winds compared to NCEP winds. Considering, these results we designed one more experiment replacing NCEP winds with QuikSCAT winds for the same period (2003-2009), denoted as the QuikSCAT experiment (QSCATEXP).

This report presents the validation of the SST, sea surface height anomaly (SSHA), current, salinity, depth of 20°C isotherm (D20), Mixed Layer Depth (MLD), and Isothermal Layer Depth (ILD) from the two GODAS-MOM experiments: NCEPEXP and QSCATEXP.

4. Data set used for validation and methods

To validate model outputs the following observational products are used. Microwave based merged SST products from the Tropical Rainfall Measuring Mission (TRMM) onboard the TRMM Microwave Imager (TMI) and Aqua aboard the Advanced Microwave Scanning Radiometer (AMSR-E) OI SST product (TMIAMSRE) is used to validate the model near surface temperature. Merged altimeter gridded SSHA data [*AVISO,* 2009] was utilized to validate the model derived SSHA. The model derived SSHA was estimated as the difference between model sea surface height and its annual mean (2004-2009). All the data sets, which

were used for model validation, were interpolated to the horizontal and vertical grids of the model.

The depth of the 20°C isotherm is used as a measure of the ability of the model to capture the thermocline variability [*Yu,* 2003]. Although, in principle, the depth of thermocline is the depth of the maximum vertical temperature gradient, it is often specified in terms of the depth of a representative isotherm. It reduces the three-dimensional variability into a two-dimensional field, which can be mapped and studied conveniently [*Kessler,* 1990]. The ILD is defined as the depth where the temperature is 0.8°C less than SST [*Kara et al.,* 2000a]. The MLD is calculated as the depth where the density is equal to the sea surface density plus the increment in density by 0.125 kg m^{-3} [*Huang and Russel,* 1994*; Kara,* 2000b]

The temperature and salinity climatology obtained from World Ocean Atlas (WOA09) *Locarnini et al.* [2010] were used to validate the mean monthly evolution of the model derived sea surface salinity, D20, MLD, and ILD. The weekly gridded objective analysis fields of temperature and salinity data (2004-2007) from Ifremer (http://projets.ifremer.fr/coriolis) were used to examine the model's ability to capture the intraseasonal and interannual variability of D20, MLD, and ILD. During 2008-2009, the temperature and salinity measured by RAMA buoys [*Mcphaden et al.,* 2009] were used to validate the daily MLD and ILD from model output. It is worth mentioning here that both Argo and RAMA data are assimilated in the model, however, due to the lack of an independent data source for the validation of the subsurface temperature and salinity structure, we used this data set to explore how well the model assimilation tracks these observations. The ability of these gridded observations to represent the spatial structure of temperature field accurately depends primarily on the spatial density of the observations and also on how frequently the observations are made. It is important to mention here that we cannot rely absolutely on the Argo gridded temperature field to assess model output; however it does

provide a broad idea of the model performance on large spatial scales. The data from two Triangle Trans Ocean Buoy Network (TRITON) near equatorial locations (1.5°S, 90°E and 5°S, 95°E) in the IO were not assimilated during 2004, which provides a unique data source to validate the model vertical temperature section at these locations. The RAMA buoy measures time series of temperature and salinity continuously at depths of 1, 10, 13, 20, 40, 60, 80, 100, 120, 140, 180, 300 and 500 m and 1, 10, 20, 40, 60, 100 and 120 m respectively. We consider measurements at 1 m nominally as from the surface.

The seasonal climatology of surface current patterns simulated by the model is compared with Ocean Surface Current Analysis-Real Time (OSCAR) currents [*Bonjean and Lagerloef,* 2002*; Johnson et al.,* 2007] as well as with drifter currents produced by the Surface Velocity Program (SVP) of the Tropical Ocean Global Atmosphere (TOGA) experiment [*Lumpkin and Garraffo,* 2005]. The OSCAR currents represent an upper 30 m average of near surface currents and have the advantage of providing a more complete spatial and temporal coverage. It is important to mention that the OSCAR currents are not strictly observations; instead, they are computed from the geostrophic velocity calculated from satellite altimetry sea level data, the Ekman velocity calculated from surface winds, and the velocity associated with the surface buoyancy gradient using dynamical and statistical methods [*Lagerloef et al.,* 1999]. A comparison of OSCAR currents with currents from RAMA buoys in the IO shows large inconsistencies, both in magnitude and phase (figure not shown). It is worth to be noted that the drifter currents, highly interpolated due to the sparse sampling, and the smoothed OSCAR currents are not reliable sources for quantitative comparisons. However, for a qualitative evaluation of the surface circulation of the model, these two datasets are employed here.

We have also computed near-surface Ekman currents from the QuikSCAT surface wind vectors [*Wentz et al.,* 2001] following *Pond and Pickard* [1983] and geostrophic currents derived from the AVISO merged SSHA following *Fu and Cazenave* [2001] which

captured more realistically the spatial and temporal variation over the IO. The data were also utilized to assess the near-surface circulation pattern in the northern IO. The QuikSCAT and NCEP2 wind data are also used to explain the large discrepancy in the equatorial current between the NCEPEXP and QSCATEXP.

Horizontal currents at 10 m depth derived from RAMA Acoustic Doppler Current Profilers (ADCP) [*McPhaden et al.,* 2009] were used to validate the interannual and intraseasonal variability of ocean surface currents. Current observations from two ADCPs fitted to deep sea moorings deployed at 90˚E and 80.5˚E along the equator were also used to validate the vertical structure of the equatorial currents. These two data sets provide a unique opportunity to analyze quantitatively the model vertical current profiles. The ADCP measures currents from the sea surface down to 400 m depth, with vertical interval of 10 m. However, to avoid contamination of signals reflected at the surface as well as the limited data coverage in the deeper level, only the data between the depths of 40 m and 400 m are used in this study. Volume transport estimates provide another way of validating model current profiles and such estimates from ADCP measurements at 80.5˚E and 90˚E on the equator have been used for this purpose. The volume transport per unit width from 40 m to 200 m depth is computed by using the expression $\int_{200m}^{40m} udz$ (2)

In order to understand the model's ability to capture intraseasonal and interannual variability, we performed time series analysis at 8 selected regions of the IO and for whole IO basin for D20, MLD, SST and SSHA. Figure 4.1 shows boxes in the IO used for the time series analysis. The boxes are identified as the *Central Arabian Sea* (CAS-62.5°E, 67.5°E; 12.5°N, 17.5°N), the *Central Bay of Bengal* (CBOB-87.5°E, 92.5°E; 12.5°N, 17.5°N), the Lakshadweep Sea (LAK-70°E, 75°E; 5°N, 10°N), *Somalia* (SOM-50°E, 60°E; 0°, 10°N), the *Wyrtki Jet* (WYRT-80°E, 90°E; 2.5°S, 2.5°N) region, the *Indonesian Throughflow* (ITF-100°E, 110°E; 20°S, 10°S) region, the *South Equatorial Current* (SEC-65°E, 75°E; 17.5°S, 12.5°S) region and the whole *IO basin* (IO-30°S, 30°N; 30°E, 120°E). In order to understand

the ability of the model to capture the westward propagating features in SSHA and D20, longitude-time diagrams are plotted for these parameters along 10°N, 5°N, Equator, 5°S, 10°S and 25°S.

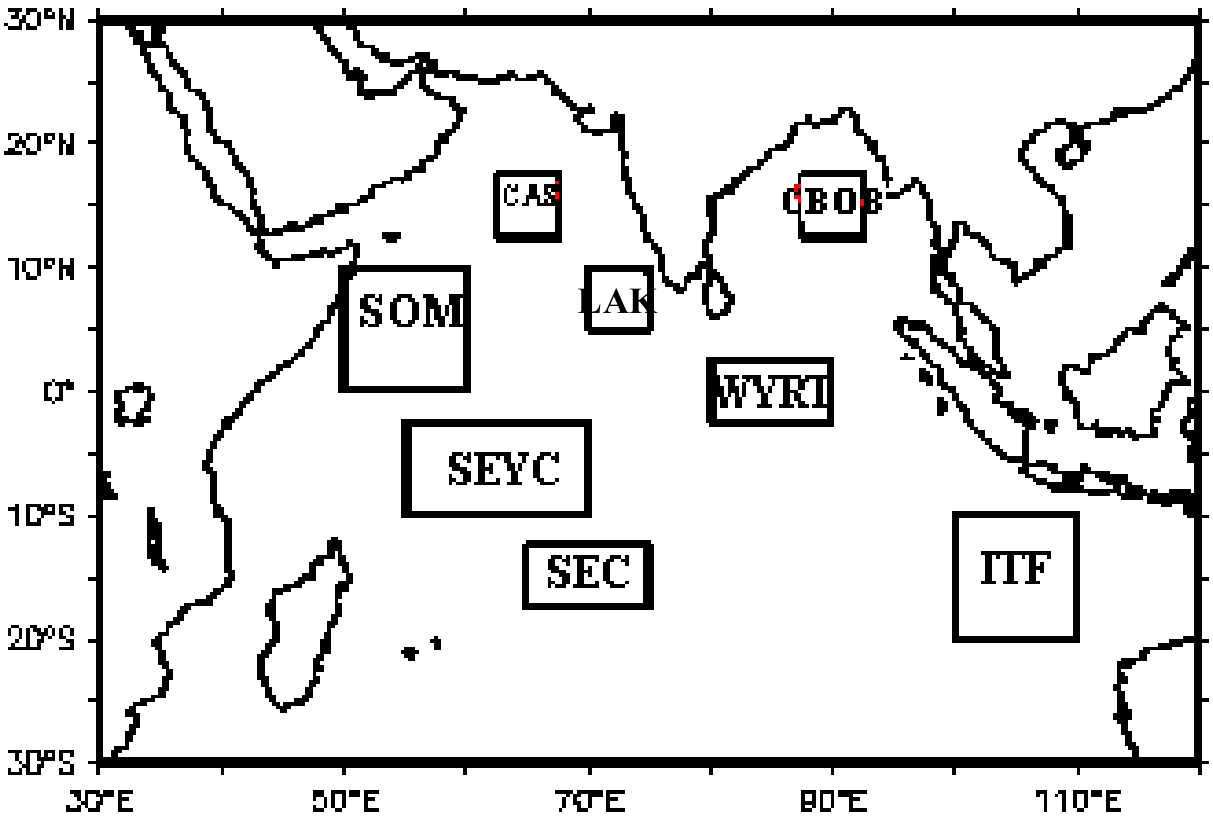

Figure 4.1. The boxes show the location of selected region in the IO used for the time series analysis. Central Arabian Sea (CAS, 62.5°E, 67.5°E; 12.5°N, 17.5°N), the *Central Bay of Bengal* (CBOB-87.5°E, 92.5°E; 12.5°N, 17.5°N), the Lakshadweep Sea (LAK-70°E, 75°E; 5°N, 10°N), *Somalia* (SOM-50°E, 60°E; 0°, 10°N), the *Wyrtki Jet* (WYRT-80°E, 90°E; 2.5°S, 2.5°N) region, the *Indonesian Throughflow* (ITF-100°E, 110°E; 20°S, 10°S) region, the *South Equatorial Current* (SEC-65°E, 75°E; 17.5°S, 12.5°S) region and the whole *IO basin* (IO-30°S, 30°N; 30°E, 120°E).

Quantitative analysis is performed by calculating statistical parameters such as standard deviation, correlation, mean difference (bias, model-observation) and root-mean-square error (RMSE). All of the statistical calculations are done only during the period when both data sets are available. For the validation analysis, the daily averaged observed parameters are further averaged to pentads (5 days) to match the resolution of the model data.

For better representation of these statistical parameters, we used Taylor diagrams [*Taylor,* 2001], which provide a unique way of graphically summarizing the statistical relationships between different model fields and observations. The Taylor plot summarizes the standard deviations of the observations and the model data, their correlation and the RMSE between them. In the Taylor diagram, the correlation is indicated by the angle from the vertical (radial lines are plotted for reference). The estimated variability (standard deviation) is indicated by the distance to the origin (a red dashed arc of a circle is plotted for reference; a green line is standard deviation of the observations). In the Taylor diagram the data points for QSCATEXP and NCEPEXP are shown as green and yellow circles respectively. The observation data point is marked as a black circle on the x-axis. The RMSE is represented by the radial distance between the observation and model data points. An amplitude spectrum based on the Fast Fourier Transform [*Emery and Thomson,* 1998] is used to examine the ability of the model to capture the amplitude of intraseasonal signals. The sources, resolutions, and the accuracies of the data sets utilized in this study are shown in Table 2.1.

Table 2.1. Source, temporal and spatial resolution and accuracy of data sets used in the validation

Parameter	Data source	Spatial and temporal resolution	Accuracy
AVISO Blended Sea surface height anomaly.	www.aviso.oceanobs.com	0.33°X0.33°, 7-day composite	2.5–4 cm
OI TMI+AMSRE SST	www.ssmi.com	0.25°, daily	--
RAMA Temperature	www.pmel.noaa.gov/tao	1, 10, 13, 20, 40, 60, 80, 100, 120, 140, 180, 300 and 500 m depth, daily	±0.003°C & ±0.05°C
RAMA Salinity	www.pmel.noaa.gov/tao	1, 10, 20, 40, 60, 100 and	±0.02

		120 m depth, daily	
OSCAR current	www.oscar.noaa.gov/	1°, 5-day	--
OI interpolated ARGO temperature and salinity	www.projets.ifremer.fr/coriolis	1°, weekly	--
WOA09 temperature and salinity	www.nodc.noaa.gov/	1°, monthly	--
Drifter current	www.nodc.noaa.gov	1°, monthly	--
ADCP current profiler	www.pmel.noaa.gov/tao	Daily	±5 cm s^{-1}, ±5°
Dopper current meter	www.pmel.noaa.gov/tao	Daily	±5 cm s^{-1}, ±2.5°

5. Validation of GODAS-MOM4p0 in the Tropical Indian Ocean.

5.1 Sea surface Temperature

5.1.1 Mean monthly evolution

Figure 5.1 shows the monthly evolution of multi-year average (2004-2009) SST from NCEPEXP, QSCATEXP and TMIAMSRE. The outputs obtained from two model runs show reasonably good agreement with the observations. The evolution of the seasonal cycle of spatial patterns has been captured realistically throughout the IO domain. Generally, the model shows a very small warm bias (0.3°C) compared to the observations with the exception of a very few localized regions such as the head-bay, the Somalia coast and the southwestern equatorial IO. The SST differences between model and observation in these regions are relatively large and have a strong seasonal dependence. Model SST in the head-bay shows a warm bias (>1°C) during the months of December, January and February (winter monsoon) and also during the months of July, August and September (summer monsoon). This warm bias disappears during March, after the winter season and during September at the end of the

summer monsoon season. Model SSTs along the coasts of Somali and Oman also show a warm bias (> 1°C) during June, July and August. These are the regions where strong wind induced upwelling occurs during the summer monsoon season. However, this warm bias dissipates in September. The similarity of the results obtained from each of the two model runs suggests that the wind forcing may not be the cause of these discrepancies. A study by *de Boyer Montégut et al.* [2007] showed that, during summer monsoon the heat budget in this region is strongly dominated by the upwelling along the Somali and Oman coasts. The model simulated D20 along Oman coast shows a narrow strip of relatively deeper thermocline compared to that of the observation (Figure 5.1.1). This suggests the possibility that upwelling in the model is too weak. In a nutshell, the large positive bias in the model SST in this region during this season may be associated with unresolved oceanic processes in the model. The southwestern equatorial IO region (Seychelles-Chagos thermocline ridge) shows a cold bias (of around 0.5°C) during December, January and February, and the spatial extent of the cold bias is relatively large in QSCATEXP. Except for these regions and time periods where there is bias, the model does a very good job in simulating SST. The probable reason for these large biases in certain locations has to be examined further in detail using the model heat budget analysis. It is worth mentioning here that there is no significant difference between the multi-year averages derived from NCEPEXP and QSCATEXP.

The mean and standard deviation of SST from the model and TMIAMSRE during 2004-2009 are shown in Figure 5.1.2. The similarity in these statistics for the model and the observations suggests that the variability and mean condition are represented by the model very realistically. It is notable that, there is not even a single location that could be singled out as showing a significant difference between the model and observed SST.

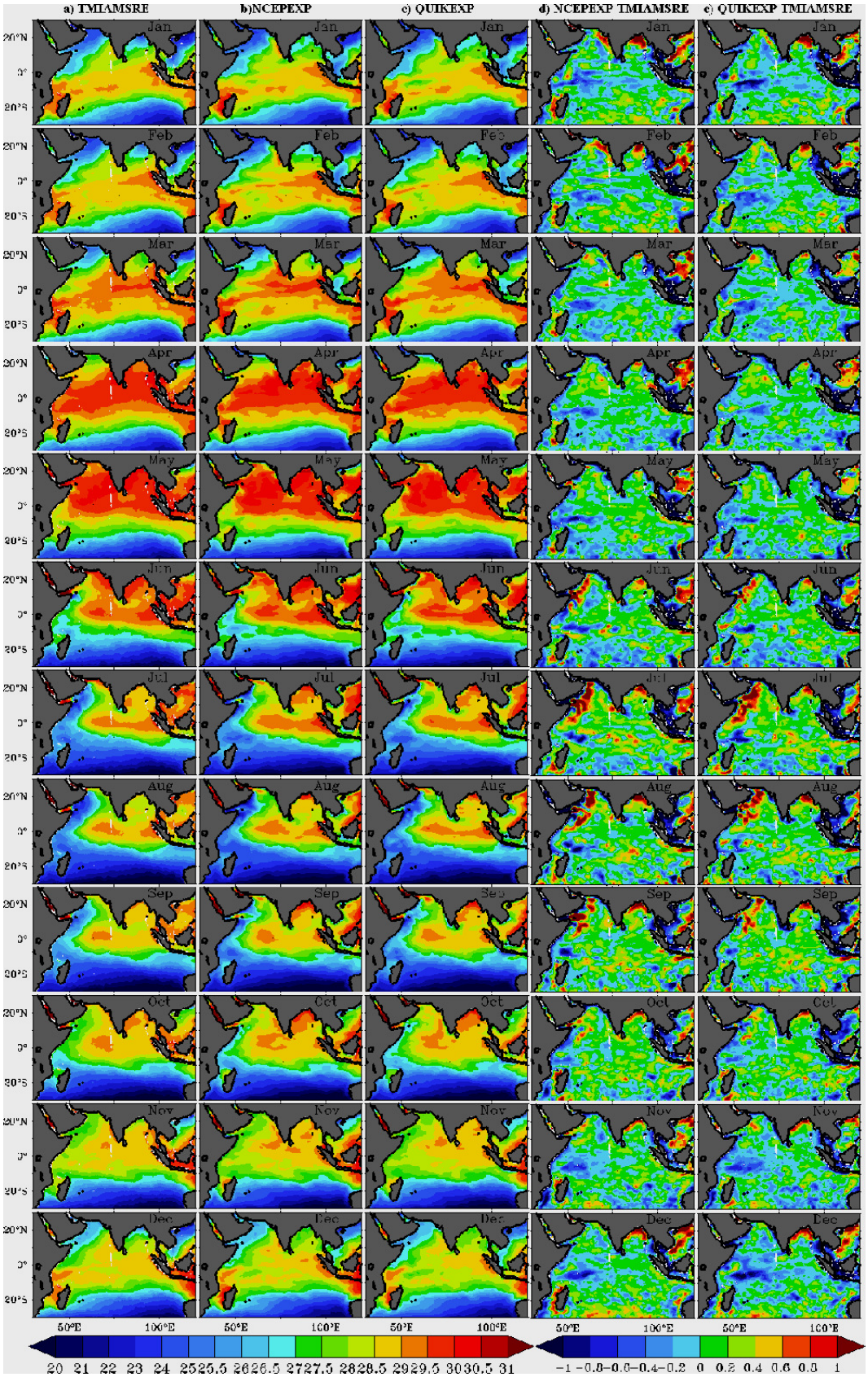

Figure 5.1.1. Monthly evolution of multiyear average of SST (ºC) derived from (a) TMIAMSRE (b) NCEPEXP (c) QUIKEXP and the difference between model and observation (d) NCEPEXP and TMIAMSRE and (e) QUIKEXP and TMIAMSRE.

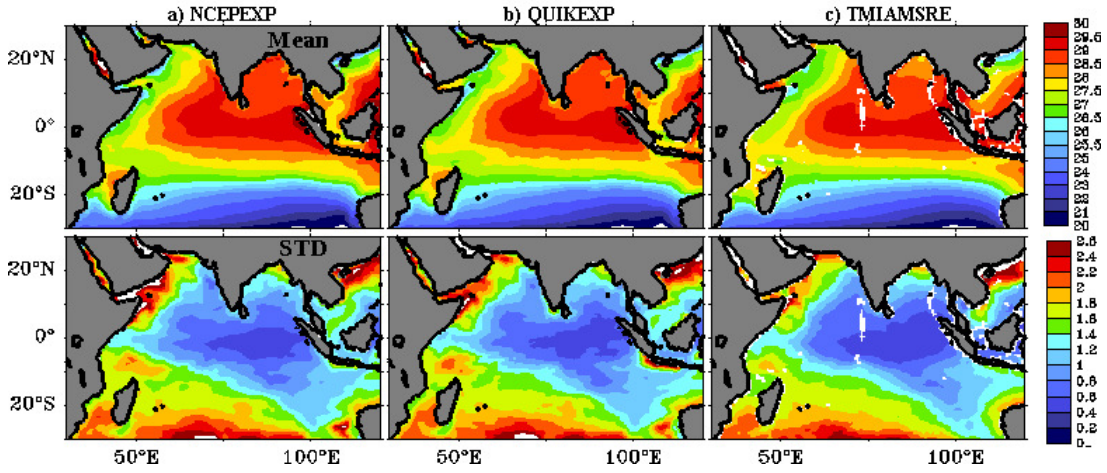

Figure 5.1.2. Multi-year (top panels) annual average and(bottom panels) standard deviation of SST (ºC) derived from (a) NCEPEXP (b) QUIKEXP and (c) TMIAMSRE during 2004-2009.

The bias of the model SST relative to the observations, their correlation and the RMSE of the model SST are shown in Figure 5.1.3. Overall, the model is about 0.2°C warmer. In the southwestern equatorial IO, the model SST is cooler than the observations above the thermocline ridge. The model also has a relatively shallow thermocline with respect to observations (10-15 m) in this same region (Figure 5.2.2). The recent study by *Vinayachandran and Saji* [2008] showed that the oceanic entrainment of cold thermocline water into mixed layer plays an important role in modulating the mixed layer temperature in this region. The relatively shallow thermocline might have caused the entrainment of cold thermocline water into the mixed layer in the model simulation leading to excessive cooling in the region of the thermocline ridge. A warm bias of 0.4°C is shown by the model offshore of the Oman coast and a bias of more than 0.5°C at the head-bay. Elsewhere the model-observation difference is only -0.2°C to +0.2°C. The correlation between the model SST and observations is larger than 0.8 in most regions. In the vicinity of the equator in the central IO and along the whole west coast of India the correlation is slightly less than 0.7. This suggests that regions of small amplitude variability have lower correlations compared to those having higher amplitude variations. The RMSE has a value of 0.5°C, which is less than the standard

deviation, as expected, in the IO domain. *Senan et al.* [2001] validated the TRMM SST in the IO region and found that the RMSE differences between satellite and *in-situ* observations fell within the range of 0.39-0.60. It is interesting to note that, the RMSE of the model SST is within in the range of the TRMM RMSE over a major part of the IO. However, in certain, locations such as the Northern part of the Somali coast, the Oman coast and the head bay the model RMSE exceeds 1°C.

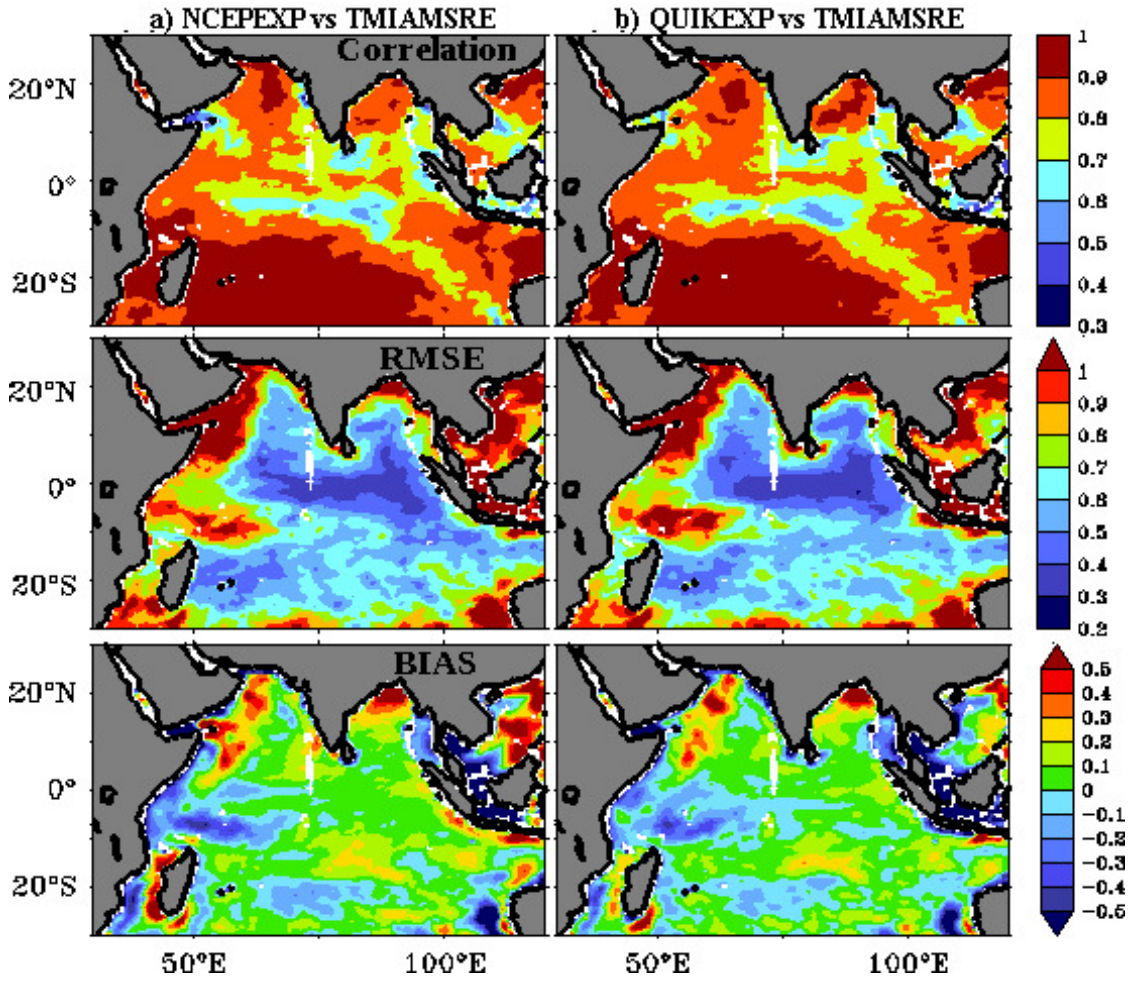

Figure 5.1.3. Bias (bottom panels) of the model derived SST (°C) with respect to observation, RMSE (middle panels) and correlation (top panels) between the model SST and TMIAMSRE SST for (a) NCEPEXP and (b) QUIKEXP during 2004-2009.

5.1.2 Intra-seasonal and inter-annual variability

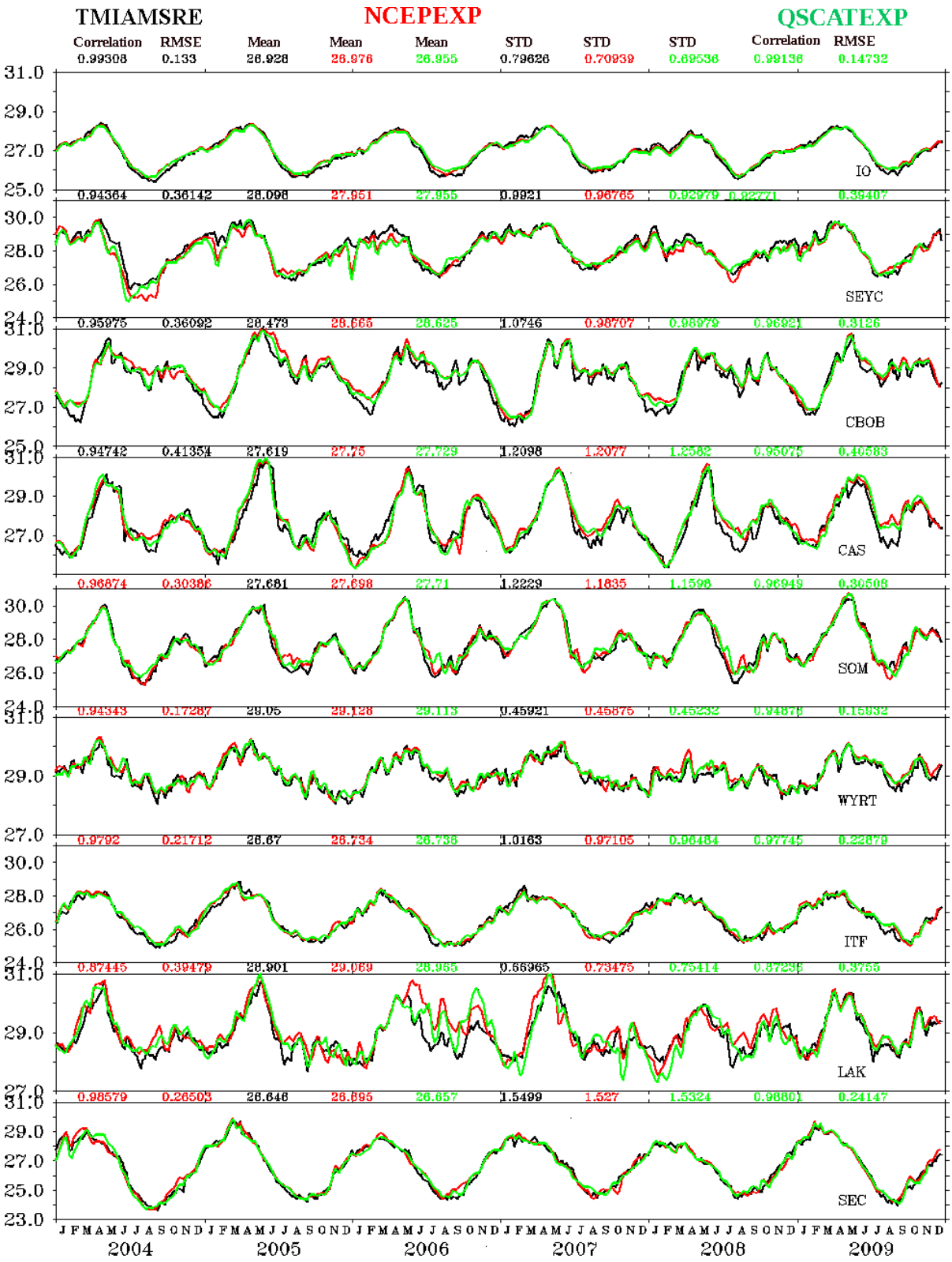

Figure 5.1.4. Time series plot of SST (ºC) (2004-2009) averaged over 8 selected regions in the IO and averaged over entire IO (as indicated in the legend). The statistical parameters are also shown along with the plot at the top of each panel.

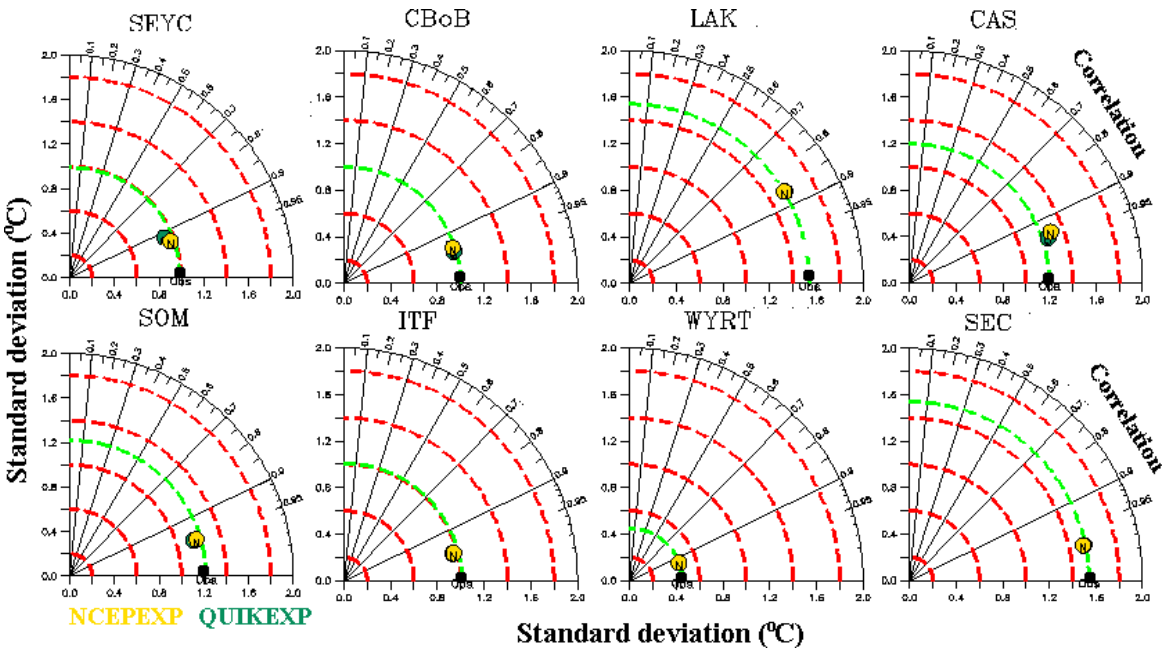

Figure 5.1.5. Taylor diagrams showing the SST (°C) performance of two model-runs in comparison with observation for 8-selected regions in the IO region. (The plot summarizes the correlation, and standard deviation of each of the QUIKEXP (green circle) and NCEPEXP (yellow circle) with respect to observation (black circle in the x-axis). The correlation is indicated by the angle from the vertical (straight lines are plotted for reference). The estimated variability (standard deviation) is indicated by the distance from the origin (a curved red dashed line is plotted for reference, green line is standard deviation of observation).

Figure 5.1.4 shows time series of SST from the model and the observations during the period of 2004 to 2009 at eight selected locations in the IO and averaged for the whole IO basin (the details of the box selected for this analysis has been discussed in section 4 covering the data and methodology). The location of each time series appears at the top of each panel in Figure 5.1.4 and the statistics for each is represented graphically in the form of a Taylor diagram in Figure 5.1.5. The plots along with the corresponding statistics clearly show that the model does an excellent job of capturing the intraseasonal as well as interannual variability both in magnitude and phase. The SST average for the whole IO basin shows a nearly perfect match in magnitude and variability. All the locations have a correlation of greater then 0.95 with the exception of Lakshadweep (LAK), where it is 0.87. At the LAK

region, during March-December 2006, an SST difference of 0.8°C is observed in both the experiments with respect to observation.

Earlier studies have reported the existence of strong intra-seasonal SST variations of 10-90 days periodicity in the Tropical IO [*Sengupta and Ravichandran,* 2001*; Rao et al.,* 2006a*; Parek et al.,* 2004]. In order to check the ability of the model to capture the amplitude of these intra-seasonal variations, we have computed the amplitude spectrum time series at eight locations. Figure 5.1.6 shows the amplitude spectrum of SST at each of these locations. The intraseasonal variations have been captured by the model at six of these locations, the exceptions being the LAK and SEC regions, where the time series showed disagreement.

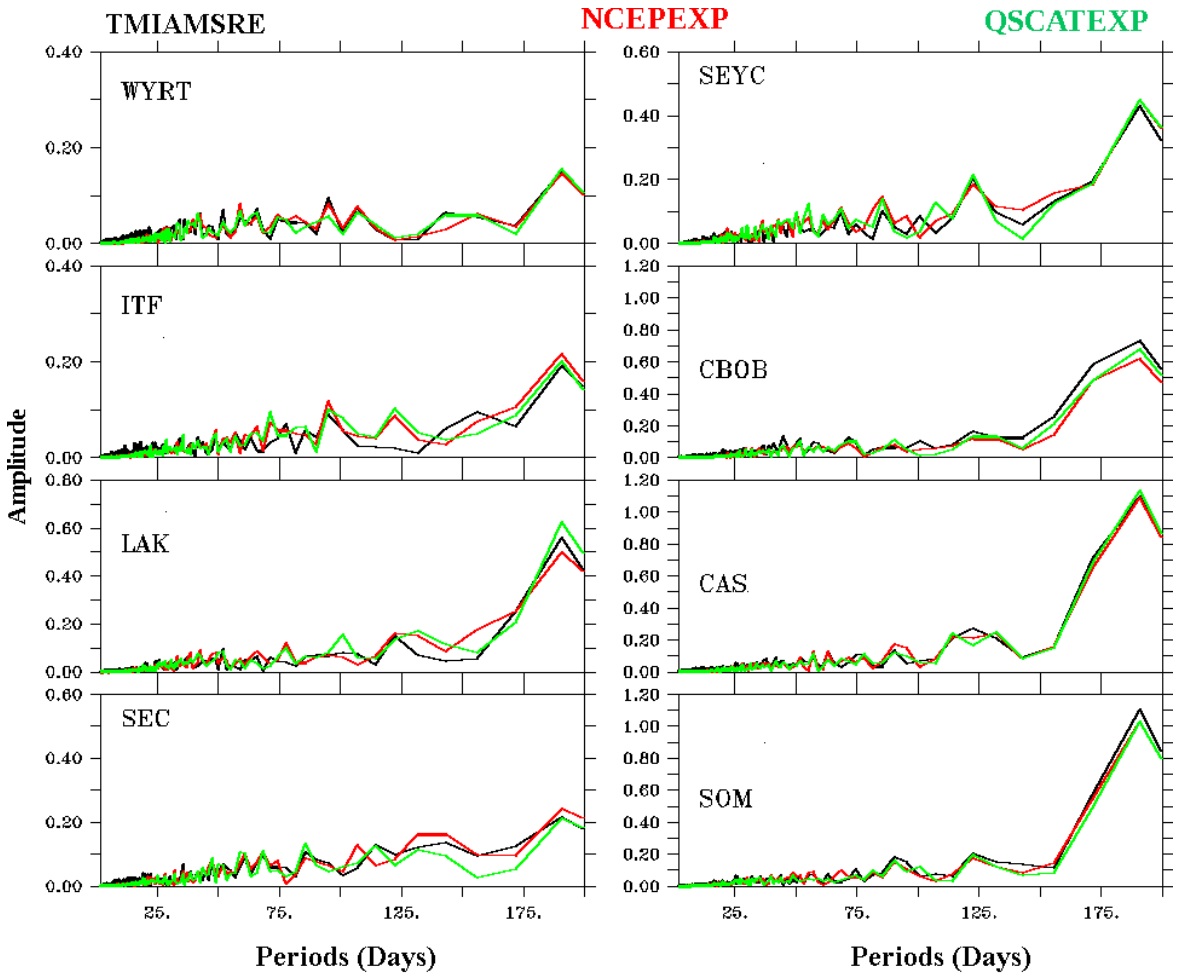

Figure 5.1.6. The FFT amplitude (°C) spectrum of SST at 8 regions in the IO.

5.2 The depth of 20°C isotherm and vertical temperature structure.

5.2.1 Mean monthly evolution

The ability of the model to reproduce the climatological monthly evolution of D20 is evaluated using WOA09. The monthly evolution of D20 derived from the WOA09 climatology, the multi-year average (2004-2009) of NCEPEXP and that of QSCATEXP are shown in Figure 5.2.1. The spatial variability of the observed D20 is accurately reproduced by both of the model runs. The location of the maxima and minima, their spatial extent and their phase are well captured by the model in both experiments. The differences between the model output and the observations show localized high values in some discrete locations south of 10°S, in the southwestern equatorial IO, and in the eastern equatorial IO. The D20 derived from observations shows some deficiency in resolving dynamical spatial structures at some locations which are seen in the model output. For example, during June and December, the model shows westward propagating Rossby waves at 5°N and 5°S in the eastern IO and the signature of these waves is also clearly evident in the SSHA climatology (Figure 5.4.1). But this feature is not visible in the D20 climatology derived from the WOA09. This discrepancy creates large differences between the model and the observations in the eastern equatorial IO during the above mentioned months. During summer monsoon, model captures upwelling in the form of the shoaling of the thermocline between the southern tip of India and the Sumatra-Java coast and this feature is also consistent with the SSHA climatology. Hence, differences in the D20 between the model and the WOA09, may not be solely due to errors in the model. The persistence of relatively large positive differences (+ 15 m) between the D20 derived from the model and the WOA09 south of 10°S will be discussed later in this section. In a nut-shell, both QSCATEXP and NCEPEXP capture all of the climatological features in a reasonably good manner. The multi-year averages (2004-2008) of D20 derived from the two model runs do not show any significant differences.

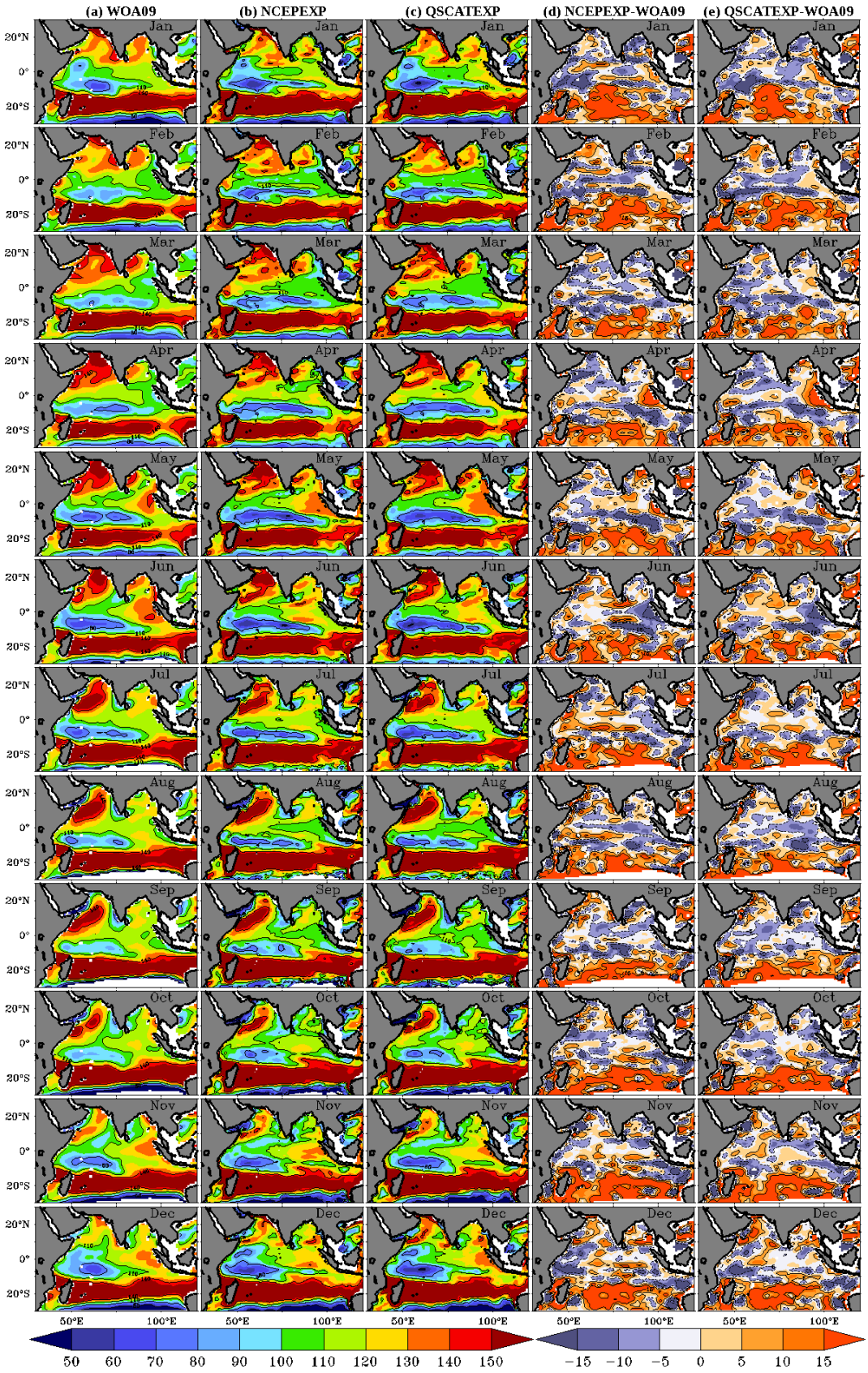

Figure 5.2.1. The monthly evolution of D20 (m) derived from (a) WOA09 climatology, multi year average (2004-2009) of (b) NCEPEXP, (c) QSCATEXP, difference between model and observation (d) NCEPEXP and WOA09 (e) QSCATEXP and WOA09.

Multi-year (2004-2008) annual mean and standard deviation of D20 derived from QSCATEXP, NCEPEXP and the Argo gridded product are shown in Figure 5.2.2. The model shows excellent skill in capturing the annual mean spatial pattern of D20 with respect to these observations. The spatial structure of the observed D20 variability is accurately reproduced by both the model runs. However, the magnitude of the variability is stronger in the model D20. The strongest variability is seen in the regions of Somalia coast, the west and east coasts of southern India and along 8°S in the southwestern IO. The least variability is seen in the central equatorial IO, the central Arabian Sea and the central Bay of Bengal. It is interesting to note that the spatial pattern of standard deviation of model D20 matches well with the standard deviation of the observed SSHA variability.

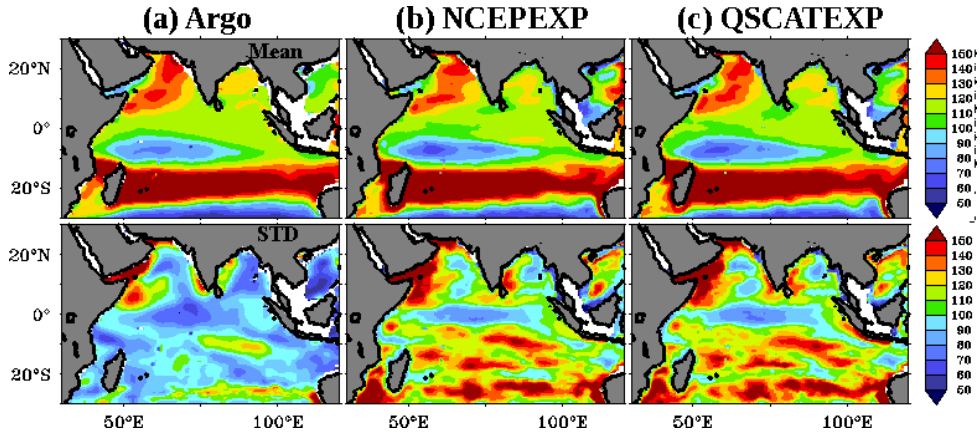

Figure 5.2.2. The annual mean (top panel) D20 (m) (bottom panel) standard deviation of D20 (2004-2008) derived from (a) ARGO (b) NCEPEXP (c) QSCATEXP during 2004-2008 (D20 is in m).

The bias (model-observation) between D20 derived from Argo gridded product and the model are shown in Figure 5.2.3 (bottom panel). Both the model runs show reasonably good agreement with observations with biases of ± 5 m north of 20°S. A relatively large positive bias (10-15 m) is seen south of 20°S. The RMSE between the D20 derived from the Argo gridded product and the model D20 are shown in Figure 5.2.3 (middle panel). The RMSE is large where the standard deviation is large. Generally the RMSE is small relative to

the amplitude of the variations observed in the IO. The correlation between the observed and the model D20 is shown in Figure 5.2.3 (top). The correlation coefficient is relatively high (> 0.70) over the major part of the basin, particularly north of 15°S, except at few locations such as the Andaman Sea and the northern Bay of Bengal. It is worth mentioning here that, these are the regions where Argo observations are relatively sparse. So the above analysis indicates that the model does a reasonably good job of estimating D20, both in magnitude and phase.

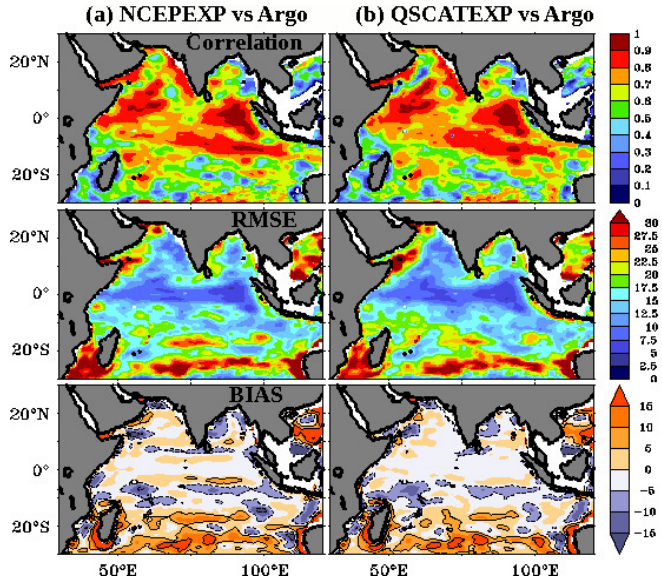

Figure 5.2.3. The bias (bottom panels) of the model derived D20 (m) with respect to observation, RMSE (middle panels) and correlation (top panels) between the model D20 and observation for (a) NCEPEXP and (b) QUIKEXP during 2004-2008.

5.2.2. Inter-annual and intra-seasonal variability.

The ability of model to capture the D20 variability at intraseasonal and interannual time scales is examined using the Argo gridded temperature product. Although it cannot be assumed that the Argo gridded temperature field is totally reliable for assessing the model output, particularly D20, it gives a broad idea about the model performance on large spatial scales. The satellite derived SSHA represents a first order approximation of the upper ocean thermal structure, except in the regions of large fresh water influx such as the northern Bay of Bengal [*Yu,* 2003]. The vertical movement of the thermocline is associated with variations in the heat storage of the ocean caused by anomalies in the subsurface temperature field and its

signature is clearly visible in the SSHA. Hence, the AVISO merged and blended SSHA data [A*VISO,* 2009] is used for qualitative assessments of the phase and amplitude variations of thermocline variability simulated by the model.

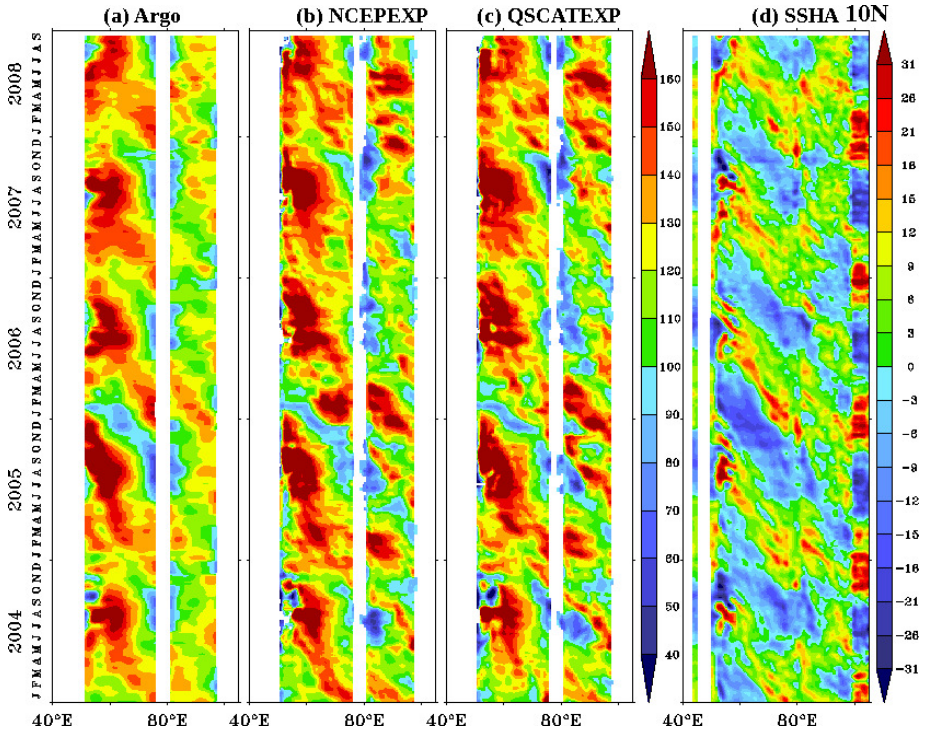

Figure 5.2.4.a. Longitude-time sections of D20 (m) derived from (a) gridded ARGO product (b) NCEPEXP (c) QSCATEXP and (d) SSHA (cm) along 10°N.

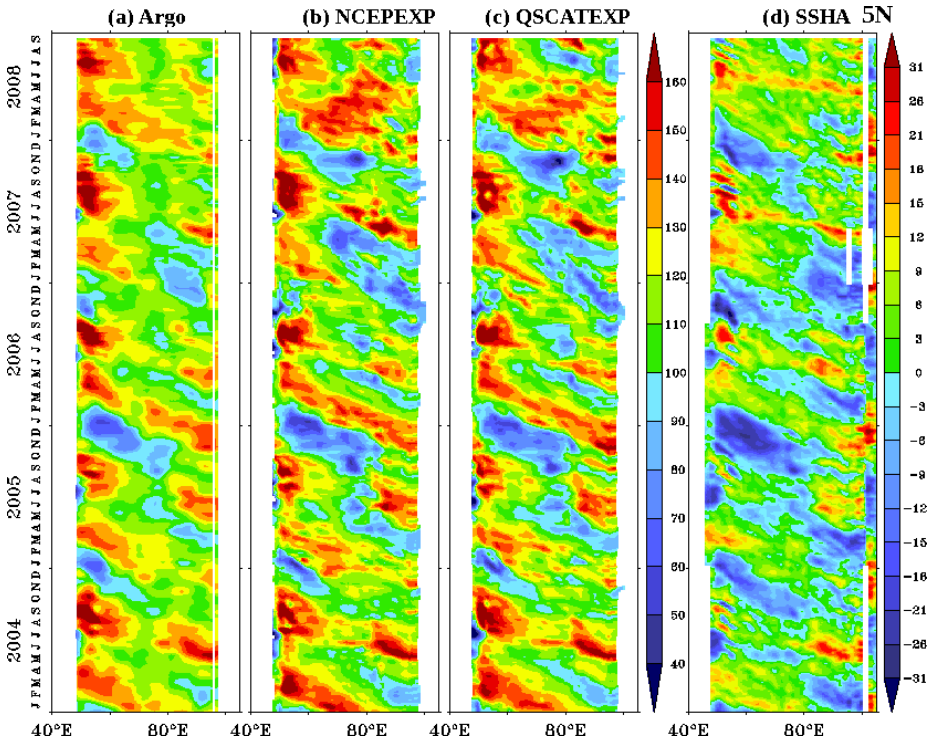

Figure 5.2.4.b. Same as Figure 5.2.4.a, but along 5°N.

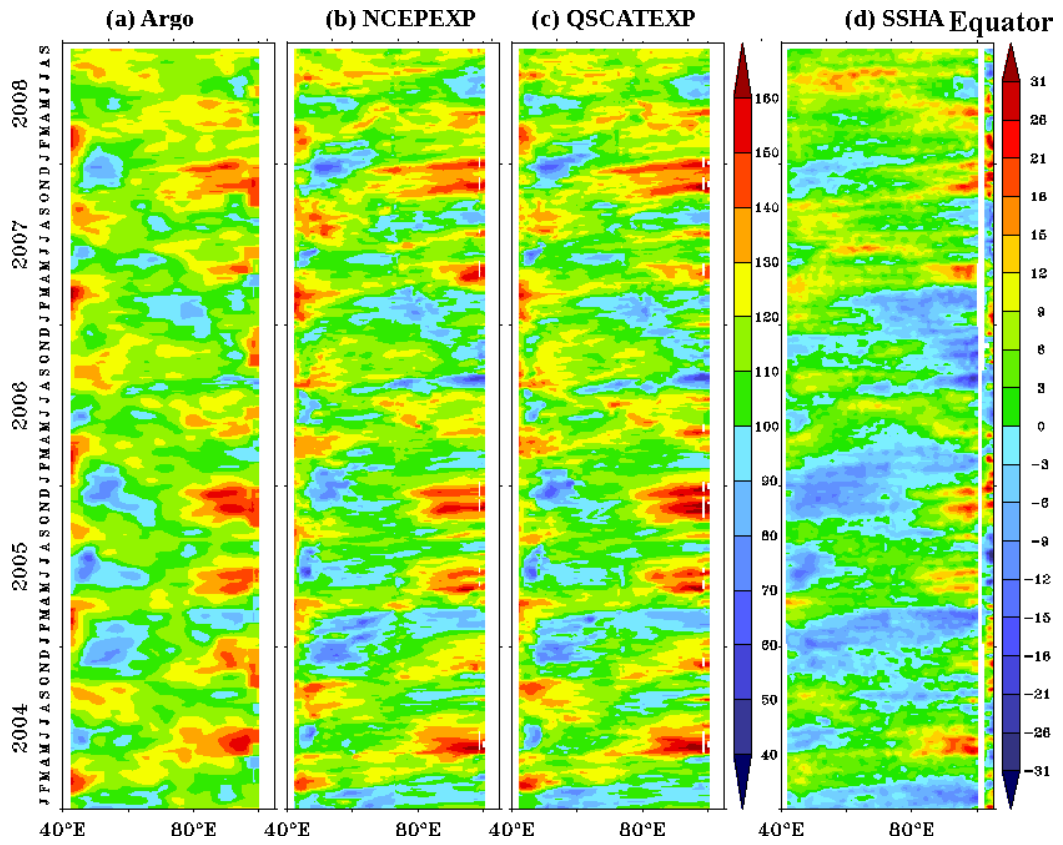

Figure 5.2.4.c. Same as Figure 5.2.4.a, but along Equator.

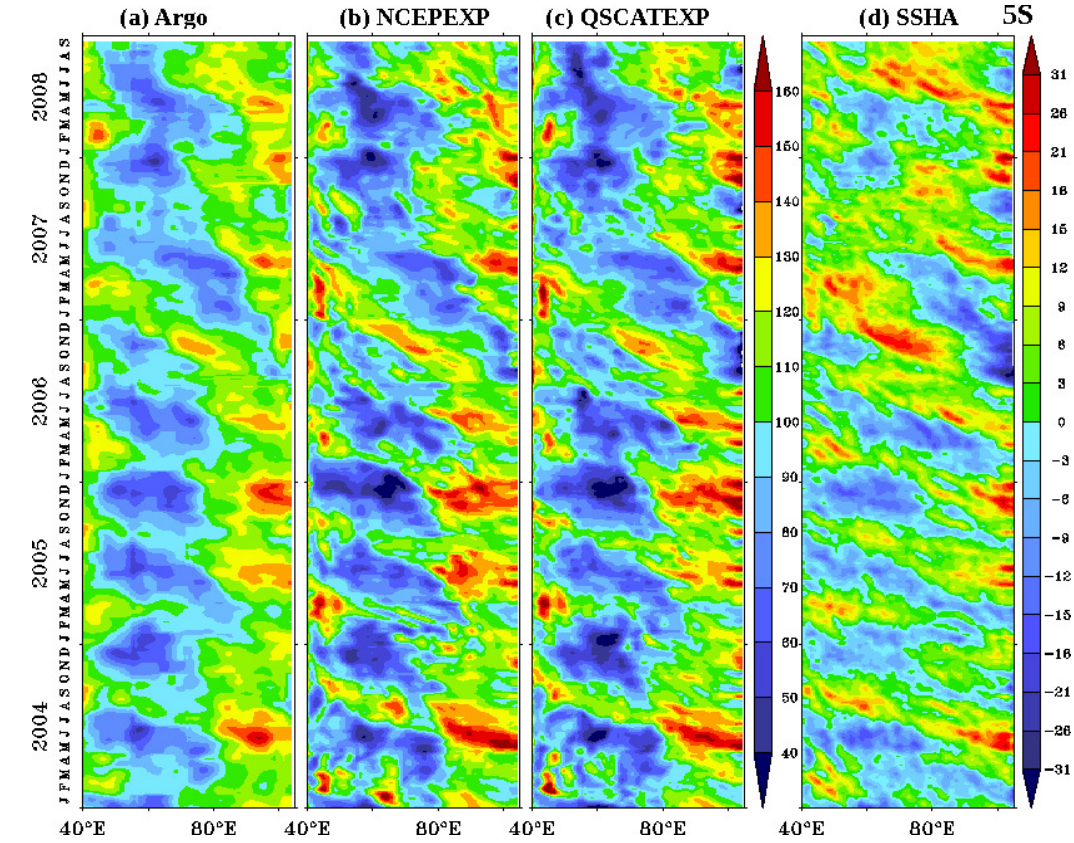

Figure 5.2.4.d. Same as Figure 5.2.4.a, but along 5°S.

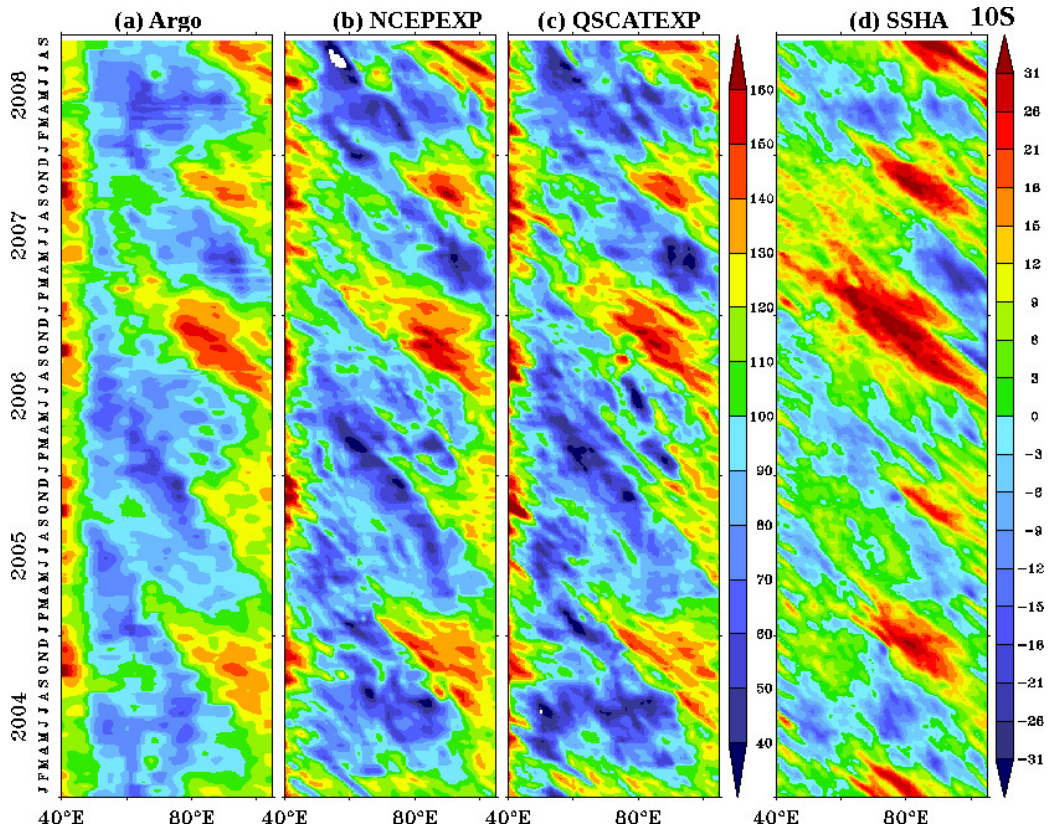

Figure 5.2.4.e. Same as Figure 5.2.4.a, but along 10°S.

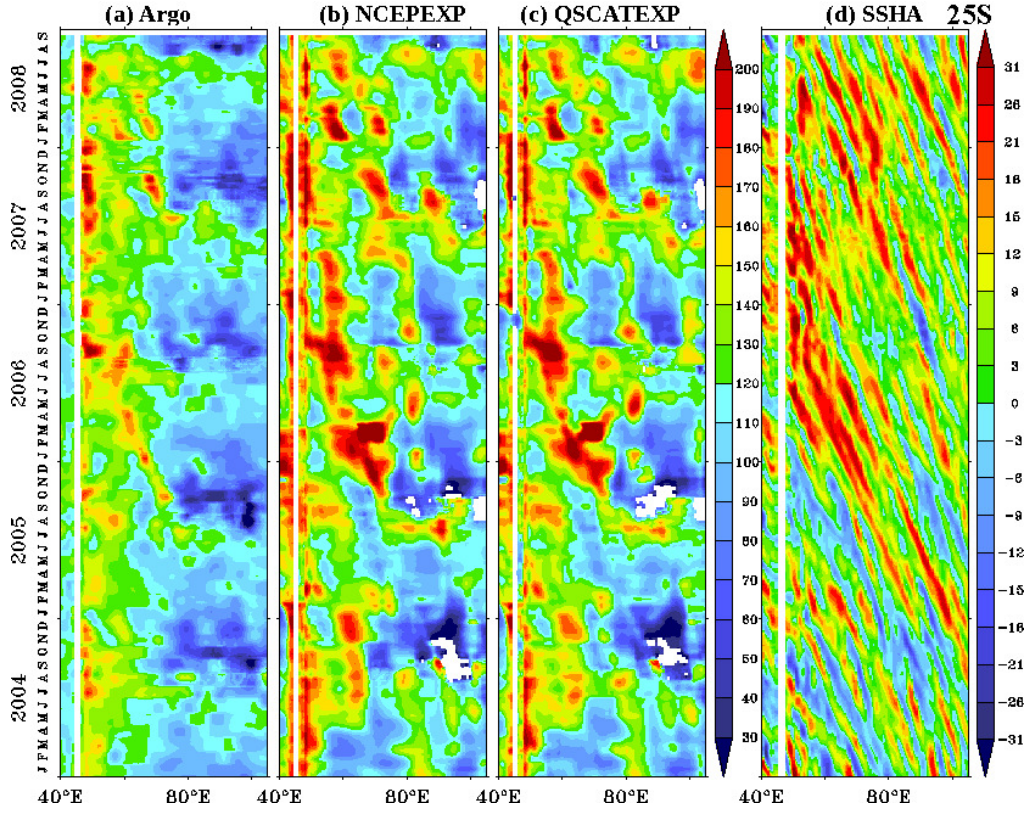

Figure 5.2.4.f. Same as Figure 5.2.4.a, but along 25°S.

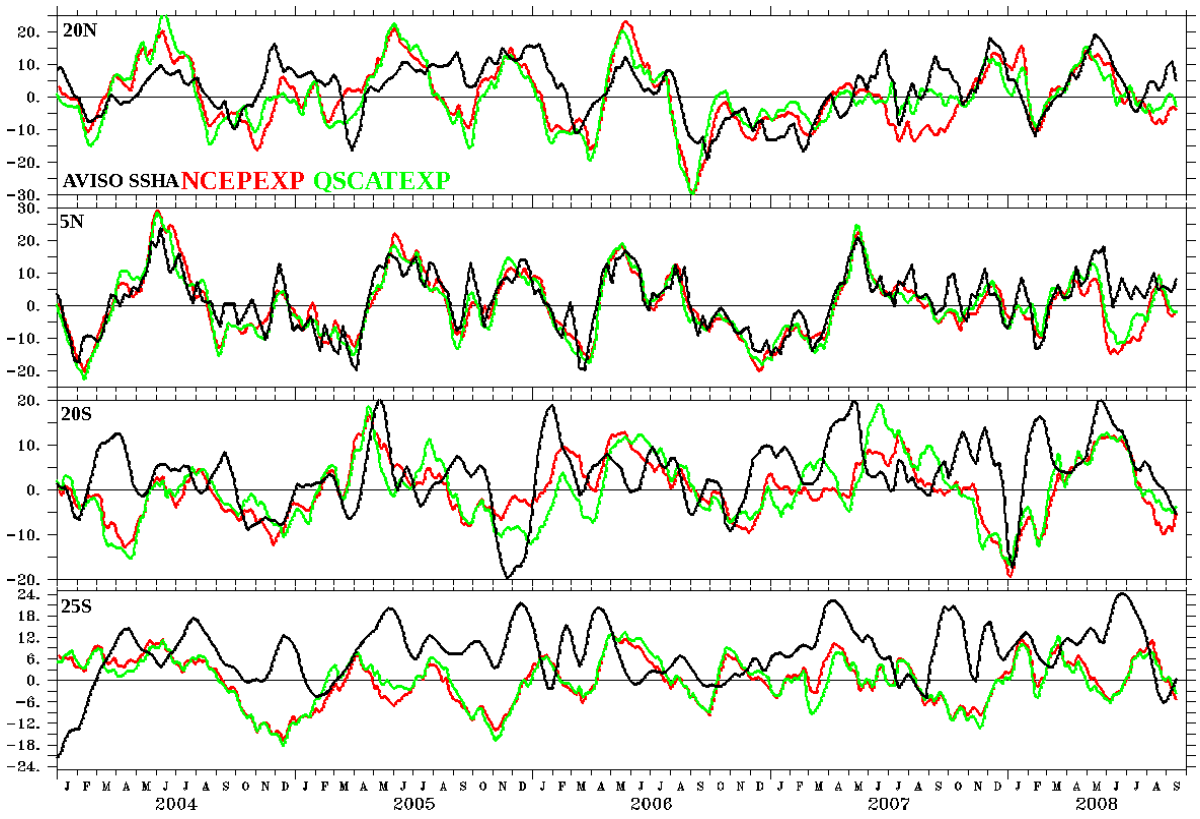

Figure 5.2.5. Temporal evolution of model derived SSHA (cm) from QUIKEXP (green), NCEPEXP (black) and satellite derived SSHA (black) (a) 20°N, 90°E, (b) 5°N, 90°E, (c) 20°S, 80°E and (d) 25°S, 80°E.

The IO experiences large variations in the wind field extending from intra-seasonal to inter-annual time scales and they have a significant influence on the vertical movement of the thermocline by local Ekman pumping and remotely by propagating Rossby and Kelvin waves [*Rao et al.,* 2008; *Rao et al.,* 2010]. In order to understand the ability of the model to capture these features, longitude–time plots of D20 and SSHA along 10°N, 5°N, the equator, 5°S, 10°S, and 25°S from 2004-2009 are shown in Figure 5.2.4. The D20 from both the model runs capture the westward propagating signal reasonably well in terms of magnitude and phase speed with respect to the observed D20 and SSHA. The shoaling of the D20 during the IOD year 2006 along the Sumatra and Java coasts and westward is reasonably well captured by both model simulations. However, the model and the observed (Argo gridded product) D20 could not capture the small westward propagating features in the SSHA as seen along 25°S (Figure 5.2.4.d). To understand the inability of the model to simulate the small westward

propagating features in the southern IO while it does so elsewhere, SSHA data from the altimeter and that derived from the model different locations (20°N, 90°E, 5°N, 90°E, 20°S, 80°E and 25°S, 80°E) are shown in Figure 5.2.5. It is interesting to note that model picks up the variability very well at 5°N, 90°E, but the coherence between the SSHA derived from model and observed decreases as latitude increases. The model resolution at 25°S is approximately 0.48° x 0.50°, which is very close to the Rossby deformation radius at this latitude. The spatial resolution of the model cannot resolve the small scale eddies that are seen in the SSHA at 25°S. It may be the primary reason for the discrepancies in the model at higher latitudes. Increasing the model horizontal resolution and using a better eddy parameterisation scheme would be able to solve this particular problem.

The temporal evolutions of D20 derived from both the model runs and the Argo gridded product at 8 selected locations in the IO and averaged over the whole IO basin are shown in Figure 5.2.6. The statistics of the model derived D20 with respect to the observations are written at the top of each panel in Figure 5.2.6 and they are graphically presented in a Taylor diagram in Figure 5.2.7. Figure 5.2.6 and Figure 5.2.7 clearly shows that in most of the regions, the model successfully captures the amplitude and the phase of the intra-seasonal and inter-annual variability. The correlation coefficient is reasonably high (> 0.80) at all locations except at CBOB, where the correlation is about 0.70. The standard deviations of the D20 derived from the Argo gridded product and the model for the periods when both data sets are available, are comparable at most of the locations. The RMSE in most regions is less than 10 m, and it is less than the standard deviation in all regions. The bias between the Argo and the model derived D20 is in the range of 1-4 m. It can be seen from the diagram that in most of the regions, the model D20 variability is within 2-6 m of the observed with the least difference off the Somali Coast. From the Figure, it is also clear that, both the models show excellent skill to capturing the variability of the D20 in the equatorial IO. To better understand the model's ability to capture the amplitude of the intraseasonal variability,

the amplitude spectrums of D20 for 8 selected locations over the IO are shown in Figure 5.2.8. The model shows reasonably good ability to resolve the amplitude of the observed periodicities of the intraseasonal signal.

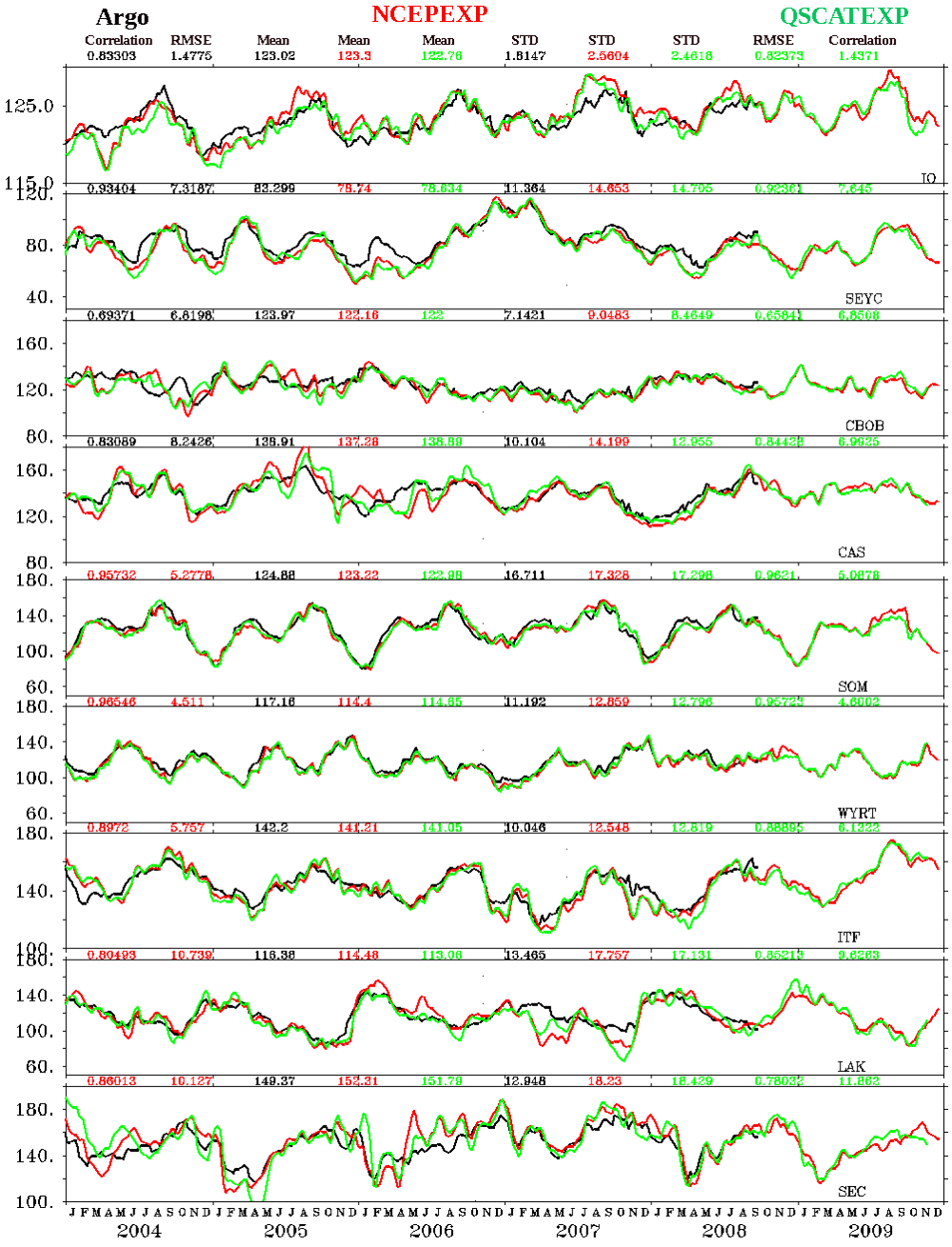

Figure 5.2.6. Time series of D20 (m) (2004-2009) derived from objectively analyzed ARGO gridded temperature data (black) NCEPEXP (red), QSCATEXP (green) averaged over 8 selected regions in the IO and averaged for the entire IO (as indicated in the legend) (see section 4 for the description about each region). (The statistical parameters such as mean, correlation, standard deviation and RMSE are shown in the top of each panel).

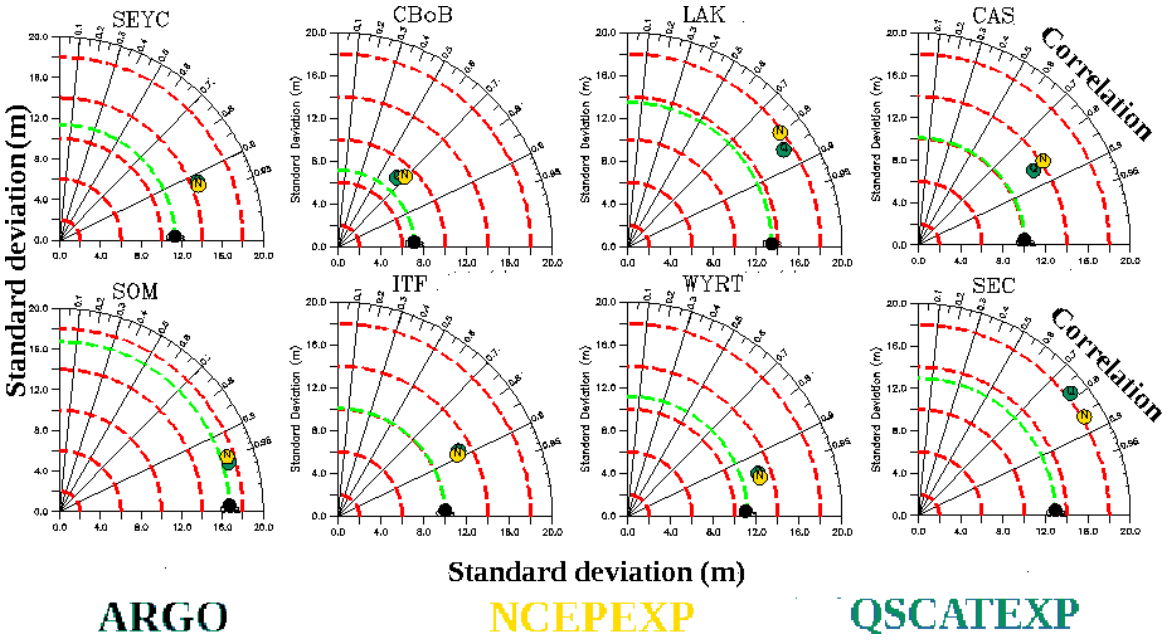

Figure. 5.2.7. Taylor diagram showing the D20 (m) performance of two model-runs in comparison with observation for 8-selceted region in the IO region (see section 4 for the description about each region).

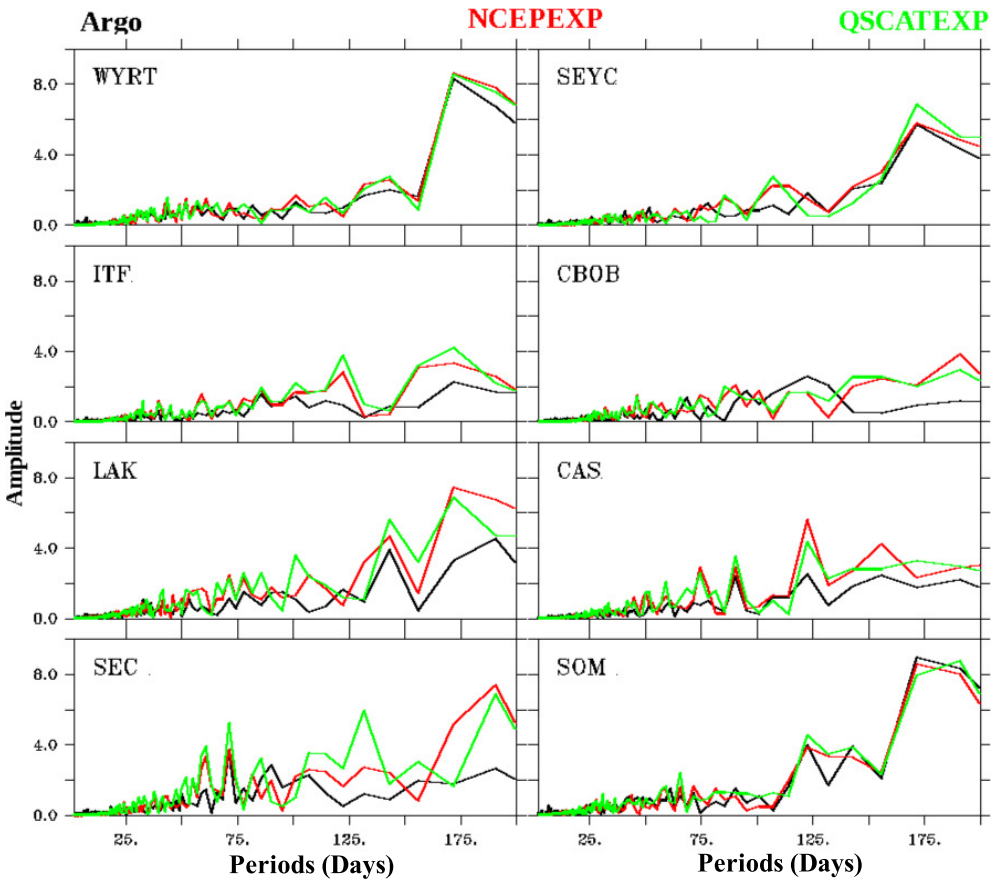

Figure 5.2.8. The FFT amplitude spectrum of D20 (m) at 8 regions in the IO (see section 4 for the description about each region).

5.2.3. Vertical temperature structure

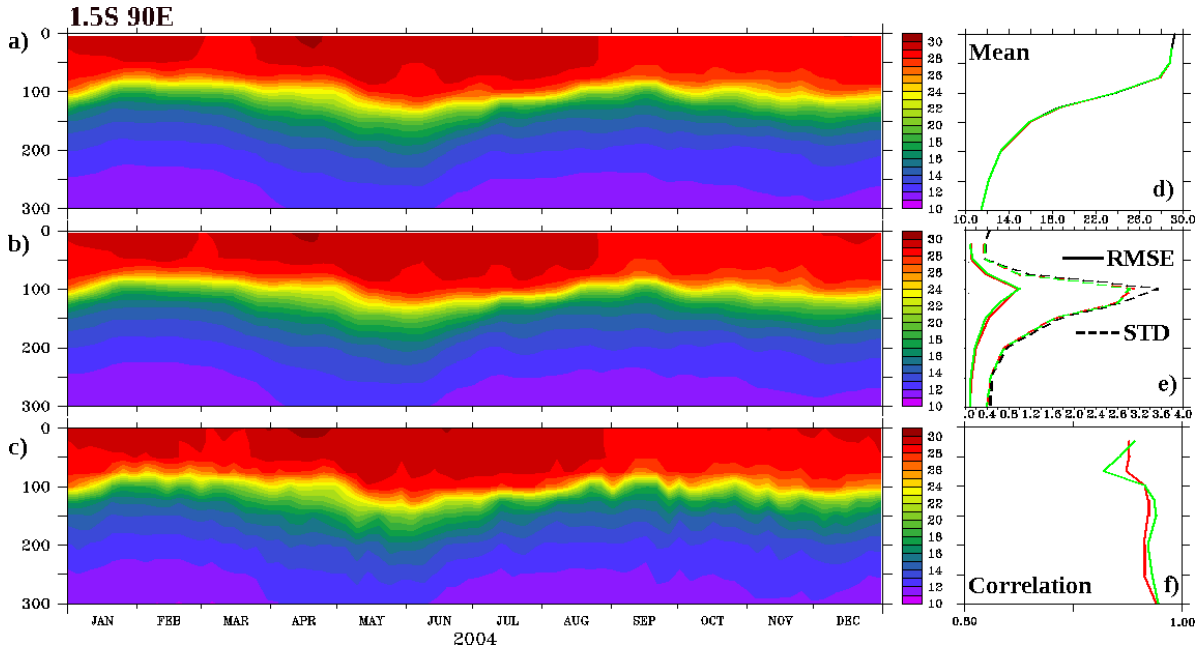

Figure 5.2.9.a. Depth-time section of temperature (ºC) from (a) QSCATEXP, (b) NCEPEXP and (c) from TRITON buoy at 1.5°S, 90°E. The right side of plot shows the statistical parameters such as (d) mean [QUIKEXP (green) NCEPEXP(red) and buoy (black)], (e) RMSE between model and observation [thin line, QUIKEXP vs buoy (green), NCEPEXP vs buoy (red)] and standard deviation of model and observation [dashed line, QUIKEXP vs buoy (green), NCEPEXP vs buoy (red)] and (f) correlation with model and observation [QUIKEXP vs buoy (green), NCEPEXP vs buoy (red)].

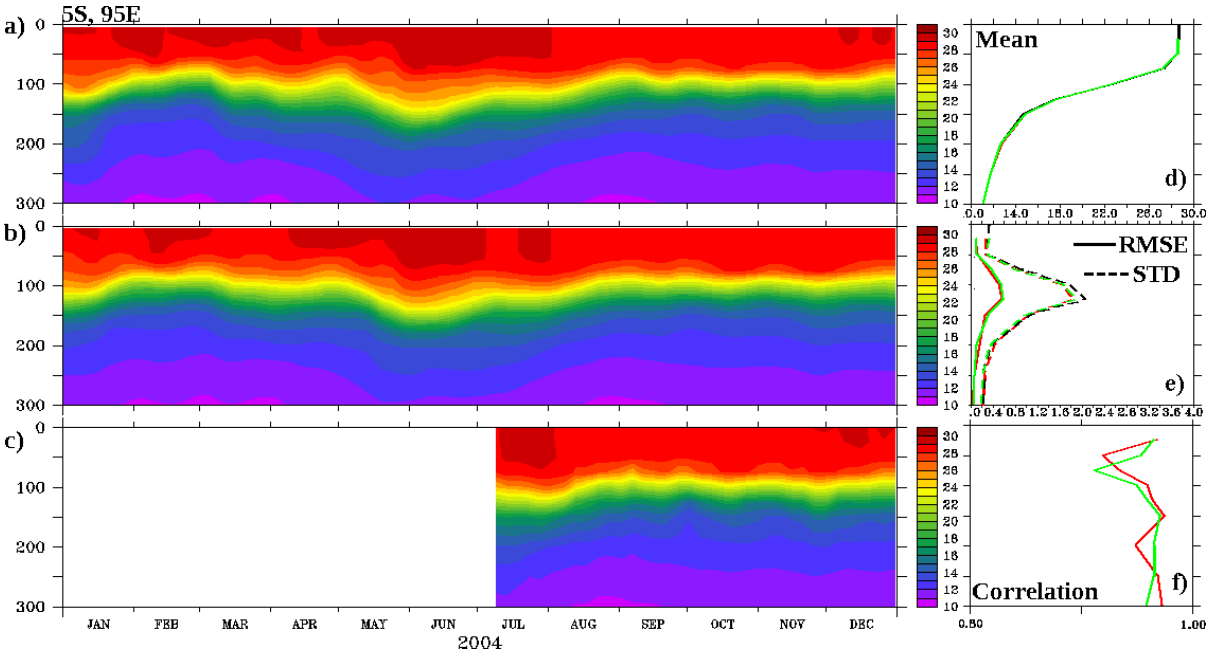

Figure 5.2.9.b. Same as Figure 5.2.9.a, but at 5°S and 95°E.

The ability of model to capture the vertical temperature profile is analysed in the equatorial IO. Figure 5.2.9.a and Figure 5.2.9.b shows depth vs. time sections of temperature from two TRITON buoy locations, 1.5°S, 90°E and 5°S, 95°E in the Equatorial IO, along with their statistics during 2004. The data from these 2 buoys have not been used for assimilation during 2004, and thus they provide a unique source of independent observations to evaluate the model performance in the eastern equatorial IO. The figure shows that both experiments capture the seasonal evolution with good reliability at both buoy locations. The standard deviations of the observations and the model reveal that both model experiments are able to reproduce the variability throughout the water column. The RMSE between the observations and the model is relatively large (~0.4°C) at depths of 60-100 m. However, the RMSE is generally less than the STD. In summary, both model experiments simulated the vertical temperature structure over time in good agreement with observations.

5.3 Sea Surface Salinity

Figure 5.3.1 shows spatial plots of the sea surface salinity from NCEPEXP, QSCATEXP and WOA09. The difference between the model (NCEPEXP) and observation is shown in Fig. 5.3.2. The analysis shows that throughout the region, with the exceptions of the southeastern Arabian Sea and the head-bay, the model does a very good job in simulating sea surface salinity such that the difference (model-observation) is only ±0.3 psu (Figure 5.3.2). In the regions of the southeastern Arabian Sea and the head Bay, the model shows large salinity biases (± 1) in the seasonal variability.

A large bias (> 1 psu) is seen in the surface salinity in the southeastern Arabian Sea. A positve bias appears in January, remains strong through February, March and April and disappears by June. It is interesting to note that this positive anomaly spreads westward seem to be associated with westward propagating downwelling Rossby waves [*Shankar and Shetye,* 1997*; Shankar et al.,* 2002] observed during this time. From September onwards, a negative

bias appears, strengthens into November and dissipates in December. The problem with surface salinity in the southeastern Arabian Sea will be discussed further below. *Rao and Sivakumar* [2003] showed that there is a dominant role for horizontal advection in redistributing salinity in the IO region. A more detailed analysis of currents and their influence on the model simulated salinity will be discussed in section 5.5.

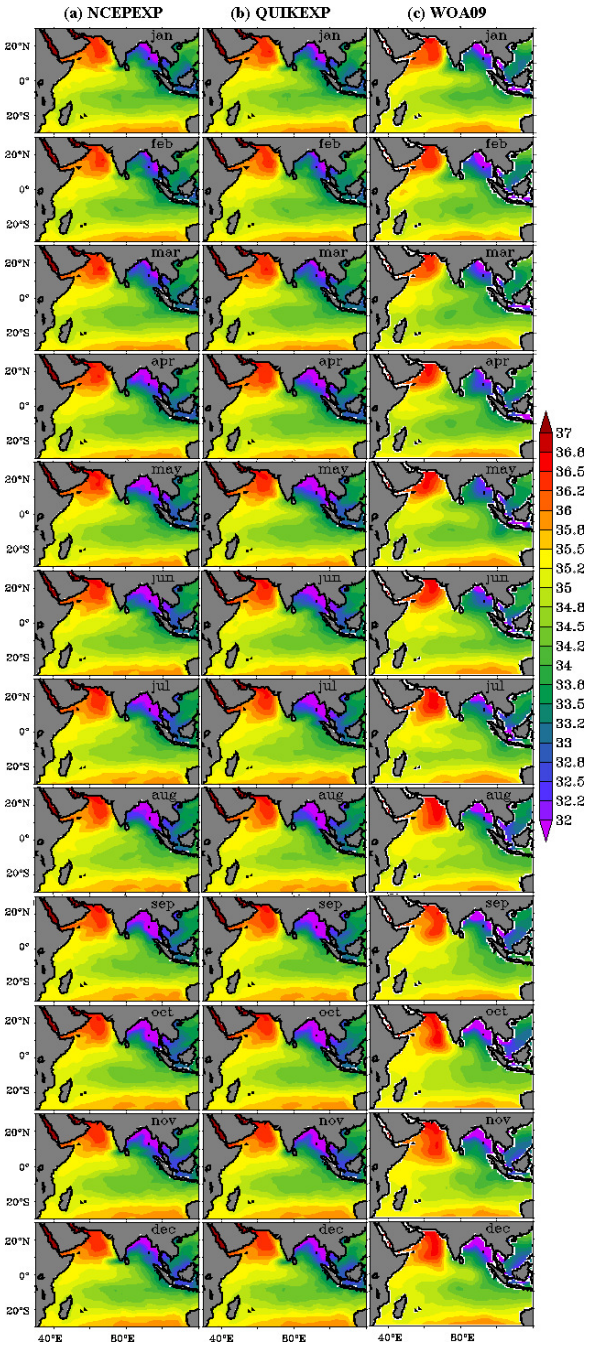

Figure 5.3.1. The climatology of sea surface salinity (psu) from (a) NCEPEXP (b) QUIKEXP and (c) WOA09.

The head Bay shows a positive bias (> 1 psu) in the sea surface salinity during July-February and a negative bias (< 1 psu) during April-June. *Rao and Sivakumar* [2003] have studied the seasonal cycle of the fresh water discharges from five major rivers along the east coast of India (Figure 5.3.3). Their study shows that, all these rivers have a pronounced annual cycle with peak discharges during the summer monsoon season. That is, the river discharges increase from June onward, peak in August-September and decrease afterwards. The annual average of the river discharge, which has been input to the model, will provide more (less) freshwater input in to the head Bay during January-May (June-September) compared to its seasonal cycle. The negative (positive) bias is seen during April-June (July-February) is associated with this use of a constant annual river discharge rather than a more realistic seasonally varying discharge. It suggests that using a monthly varying river discharge would help produce a reasonable surface salinity in the head Bay and the south eastern Arabian Sea. In the current GODAS-MOM we assimilate synthetic salinity profiles which might have led to significant problem in the salinity field. Assimilation of observed salinities would have improved the salinities.

A small negative bias (0.5 psu) in surface salinity is seen in the eastern and central equatorial IO at around 5ºS-10ºS during June-September. This is the region, where a tongue of low salinity waters with an east-west gradient driven by the Indonesian throughflow is found [*Masson et al.,* 2002; *Rao and Sivakumar,* 2003]. Earlier studies reported that, the Indonesian throughflow shows a strong seasonal variability with a maximum transport during June-July (15 Sv) and a minimum transport during February (5 Sv). The negative bias, which is seen along south of the equator in the model during June-September may be associated with the inability of the model to carry appropriate amount of freshwater by Indonesian throughflow. During July-August, there is a large negative salinity bias in the south eastern BoB. Southward current at eastern BoB (figure 5.5.1) along with anomalous equatorial westward current (see discussion in 5.5) may advect this low salinity bias from eastern BoB to

the region mentioned above. However, these effects also cannot be ruled out. The analysis provided here is qualitative in nature. In order to do a more quantitative analysis, the error in the precipitation and evaporation and its relative contribution to model derived salinity needs to be looked at in detail. The assimilation of observed salinity instead of synthetic salinity could have improved the model salinity field.

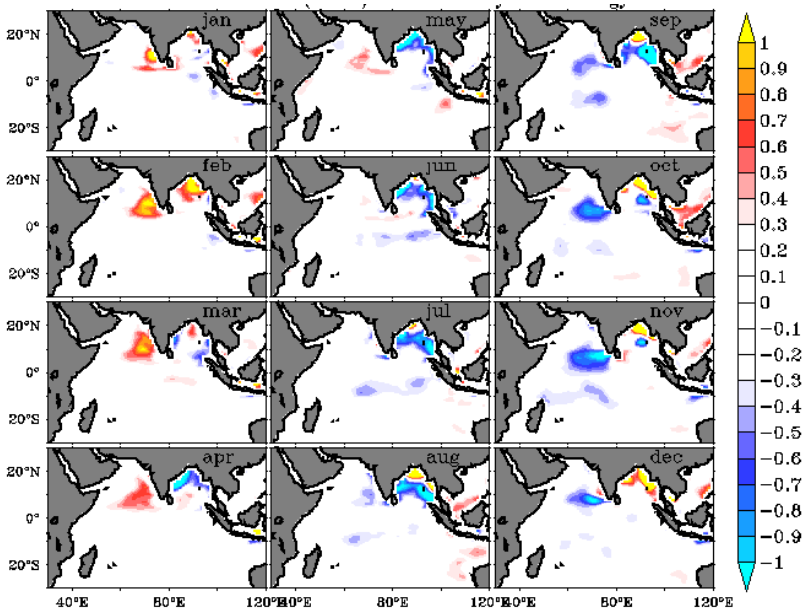

Figure 5.3.2. The sea surface salinity (psu) (averaged for 2004-2009) difference between NCEPEXP and WOA09.

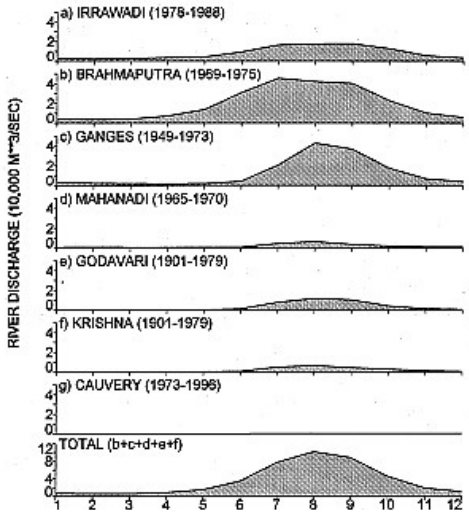

Figure 5.3.3. The annual cycle of discharge from major rivers into the Bay of Bengal (from Rao and Sivakumar , 2003).

5.4 Sea surface height anomaly

5.4.1 Mean Monthly evolution

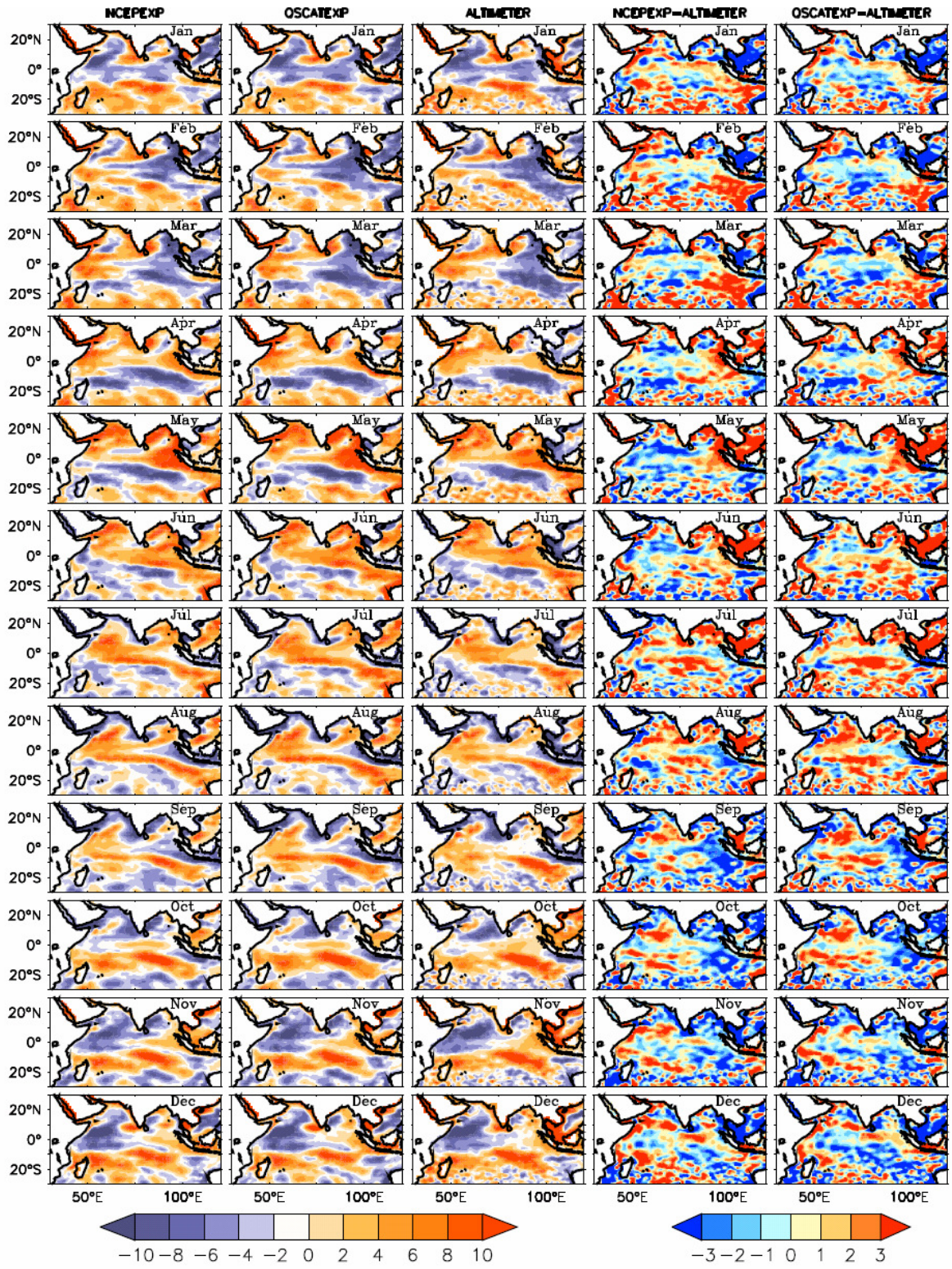

Figure 5.4.1. Monthly evolution of multiyear average (2004-2009) of SSHA (cm) derived from (a) NCEPEXP, (b) QUIKEXP and (c) altimeter, difference between model and observation, (d) NCEPEXP and altimeter and (e) QUIKEXP and altimeter.

The monthly evolutions of multi-year averages of (2004-2009) SSHA, which is derived from NCEPEXP, QSCATEXP and altimeter data, and the difference between NCEPEXP and QSCATEXP with respect to the altimeter data are shown in Figure 5.4.1. It reveals that both of the experiments are able to reproduce the seasonal evolution of SSHA as seen in the observations with significant accuracy. The seasonal cycle of the observed variability of planetary wave motions (Kelvin and Rossby waves) over the IO is reproduced with good skill in both model runs as reported in earlier studies [*Yang et al.,* 1998; *Prasad and Ikeda,* 2001*; Shankar et al.,* 2002*; Rao et al.,* 2010]. The difference in the SSHA between the model and the observations is around ± 3 cm. The accuracy of the altimetry product is 2-4 cm.

However, there are a few discrepancies such as the positive (negative) value of SSHA in the east and in the head bay is overestimated (underestimated) by > 3 cm (< 3 cm) in NCEPEXP and QSCATEXP during April-June (September-March). The Figure 5.3.2 shows the sea surface salinity difference between the model and the WOA09. It shows a negative (positive) bias of salinity in the model > 1 psu (< 1 psu) during April-June (July-February). Errors in the model salinity might be the cause of the model SSHA errors, since the salinity contribution to the sea level is significant in the head Bay [*Yu, 2003*]. For example, a salinity error of 3 units in a 30 m thick mixed layer will produce an error in the SSHA of approximately 6 cm. Neither experiment could capture the small scale eddy structures in the southern IO around 25°S. Although a strong positive (negative) bias appears west of Australia during December-April (August-October) in both experiments, there is significantly less bias in QSCATEXP compared with NCEPEXP over this region during these months. During July-August, in the south central equatorial IO (around 5°S), both of the experiments show a positive bias in the SSHA field, while at the same time showing a negative bias in salinity (0.5 psu). However, more detailed analysis is required to understand the relative contribution of

salinity, which leads to errors in SSHA over these regions. During October, in the North East Madagascar region, both model runs overestimated the SSHA.

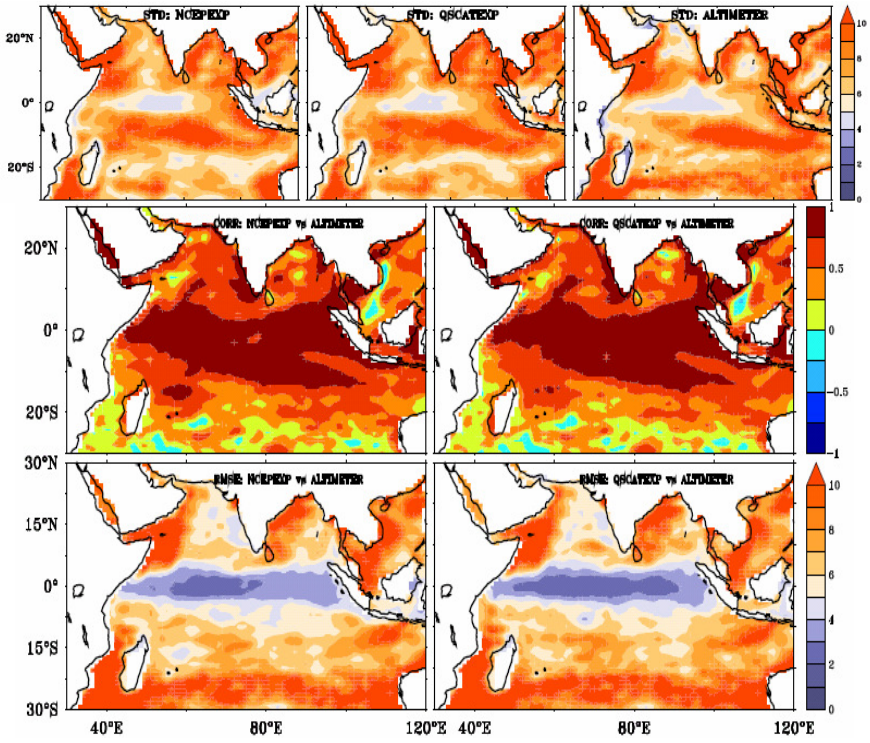

Figure 5.4.2. the standard deviation of SSHA (cm) (Top panel) derived from altimeter(left) NCEPEXP (middle) and QSCATEXP(right) during 2004-2009. The correlation (middle panel) and RMSE (bottom panel) between SSHA derived from the model and altimeter for (left) NCEPEXP and (right) QUIKEXP during 2004-2009.

Figure 5.4.2 shows the statistics of the model SSHA with respect to observations for the period 2004-2009. The analysis shows that, the model could capture the variability of the SSHA reasonably well. However, the model shows large variability than the observations in the northwestern Arabian Sea and west of the Andaman Island chain. The correlation between the model SSHA and the observed SSHA is large (> 0.75) within the latitude belt of 10°S-10°N, and decreases poleward. One possible reason for this kind of structure in the correlation may be associated with the model's horizontal resolution. The RMSE shows relatively small values in the equatorial IO, and relatively large values along the Somalia coast, in the western Bay of Bengal and in the southern IO. The RMSE is less than the STD.

5.4.2 The intraseasonal and interannual variability

The existence of large intraseasonal and interannual variability of SSHA in the TIO has been reported by earlier studies [*Iskandar et al.,* 2005; *Sakova et al.,* 2006*; Vialard et al.,* 2009*; Rao et al.,* 2010]. The ability of the model to capture the intraseasonal and interannual variability of SSHA has been examined. The 5.4.3 shows hovmoller diagrams of SSHA along 10°N, 5°N, the Equator, 5°S, 10°S and 25°S. The figure clearly shows that the model can reproduce the intraseasonal and interannual variability in both amplitude and phase with good accuracy, except at 25°S. At this latitude the model could not capture the westward propagation of small scale eddies, which is seen in the altimeter data. This is another instance where the model resolution may be a limiting factor. It is interesting to note that the model could reproduce the IOD signature in the SSHA field in Figure 5.4.3.c as a negative value of SSHA during 2006 (Figure 5.4.3.c) along the eastern end of the equator, with excellent accuracy in terms of the time of onset and westward extension.

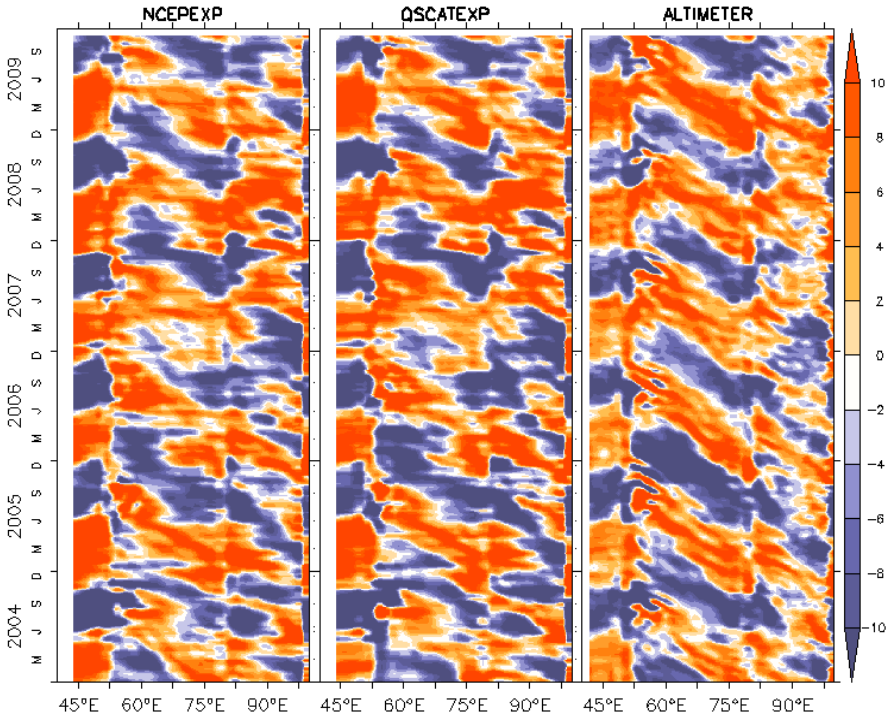

Figure 5.4.3.a. Longitude-time sections of SSHA (cm) derived from NCEPEXP (left), QSCATEXP (middle) and altimeter (right) along 10°N.

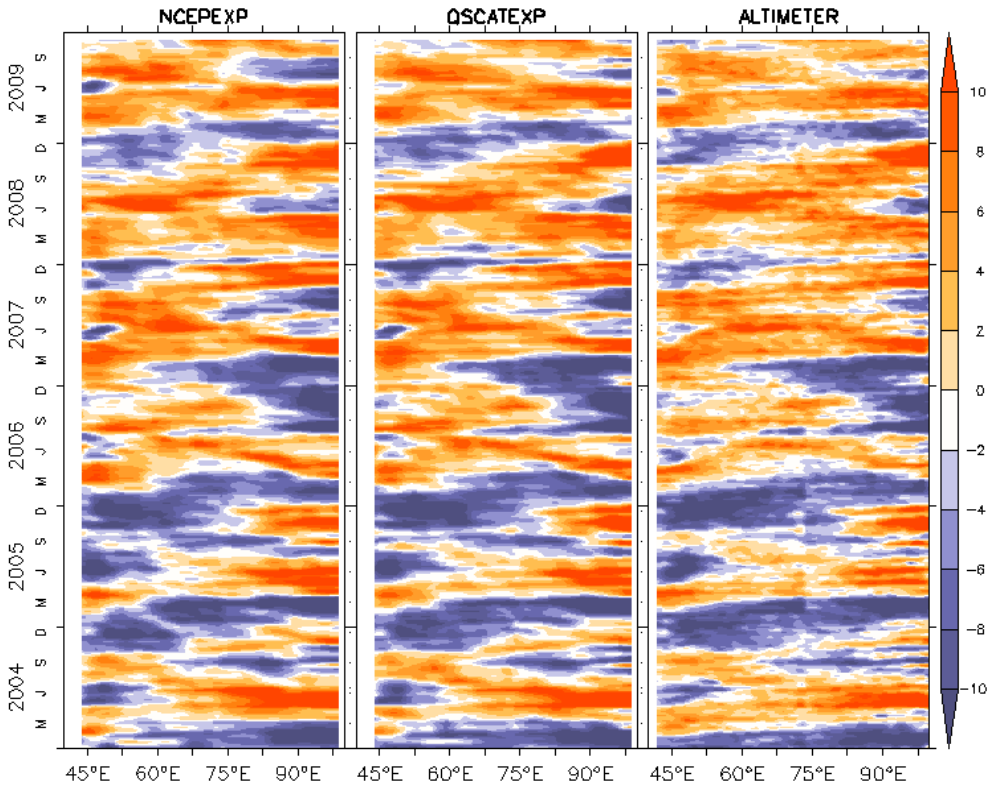

Figure 5.4.3.b. Same as Figure 5.4.3.a, but along 5°N.

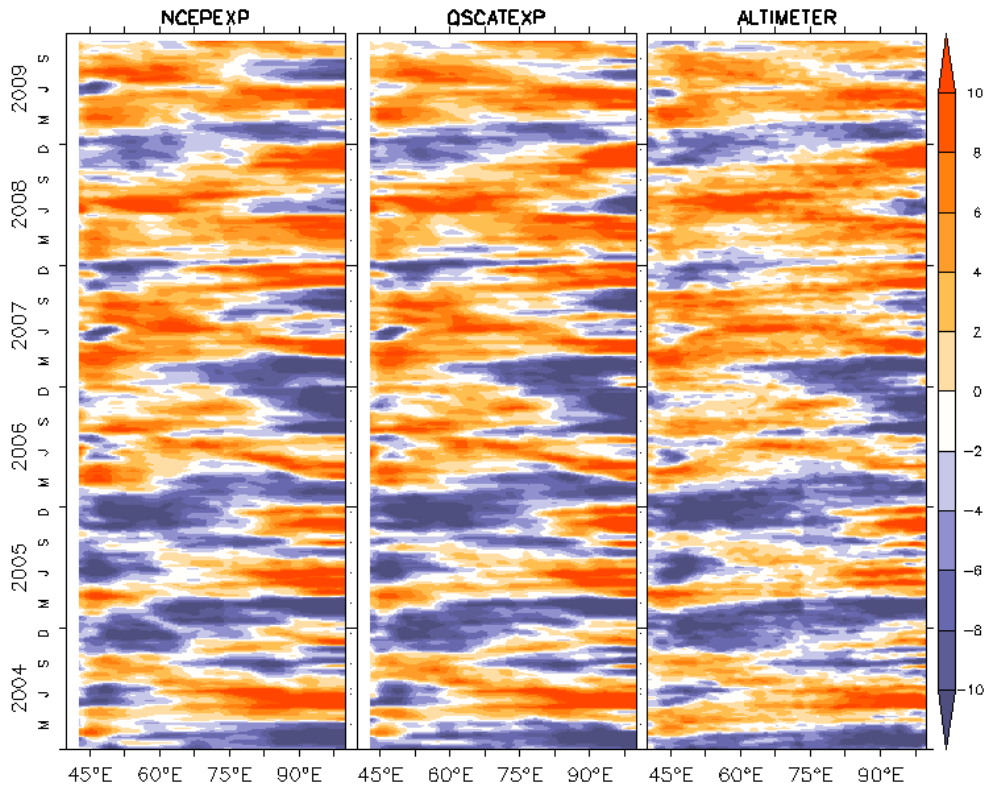

Figure 5.4.3.c. Same as Figure 5.4.3.a, but along equator.

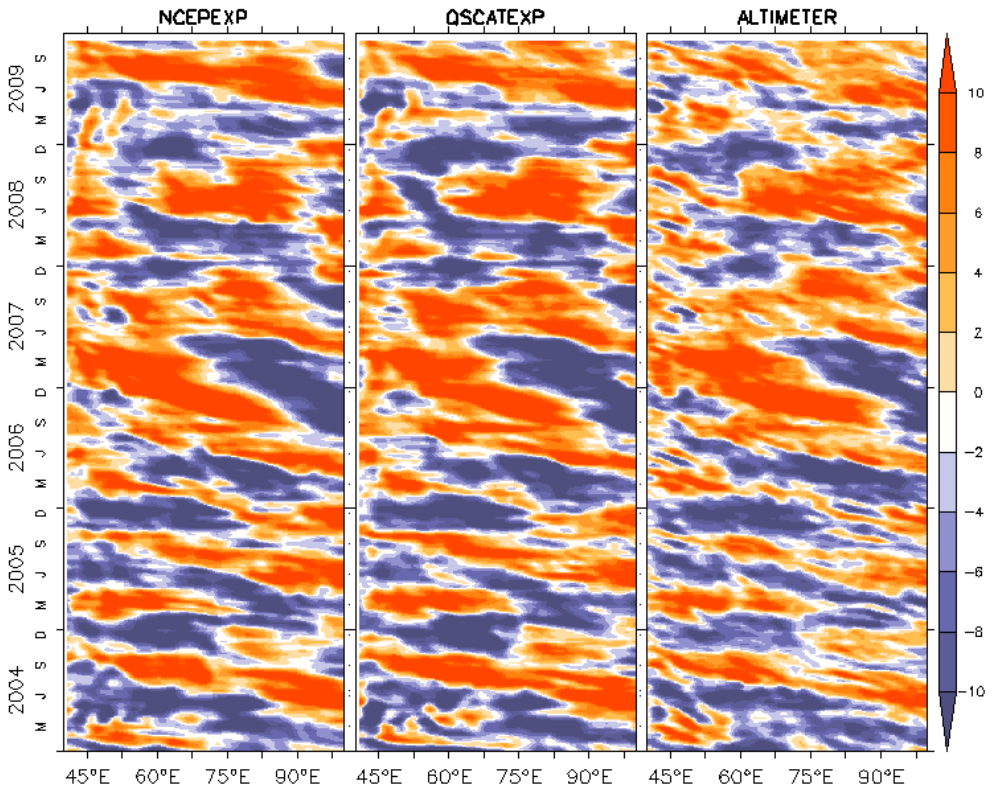

Figure 5.4.3.d. Same as Figure 5.4.3.a, but along 5°S.

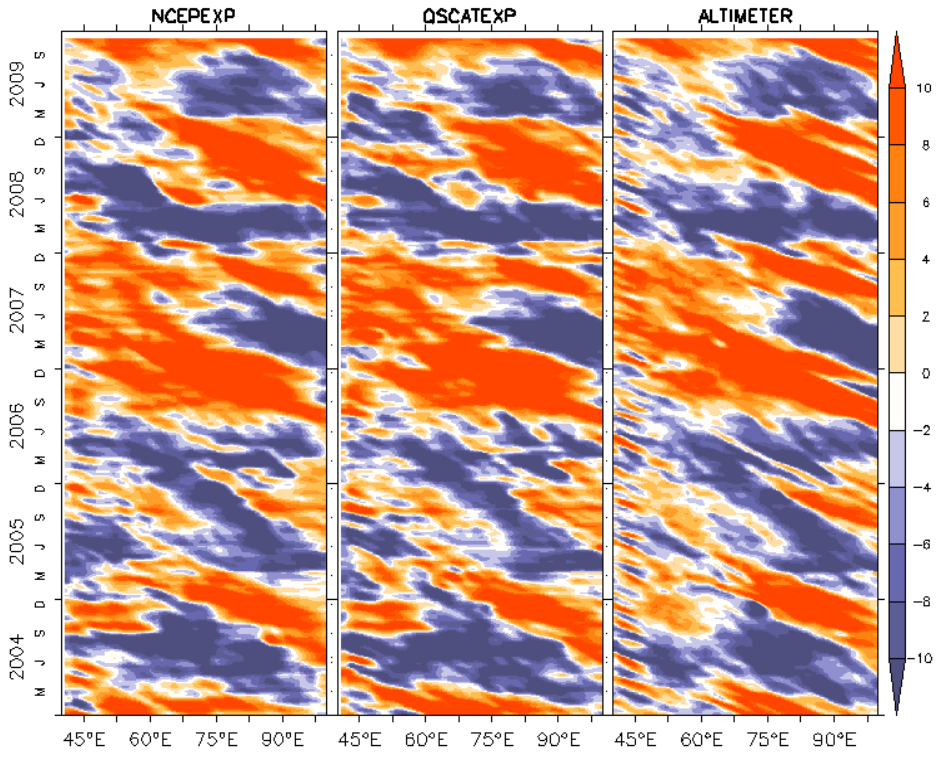

Figure 5.4.3.e. Same as Figure 5.4.3.a, but along 10°S.

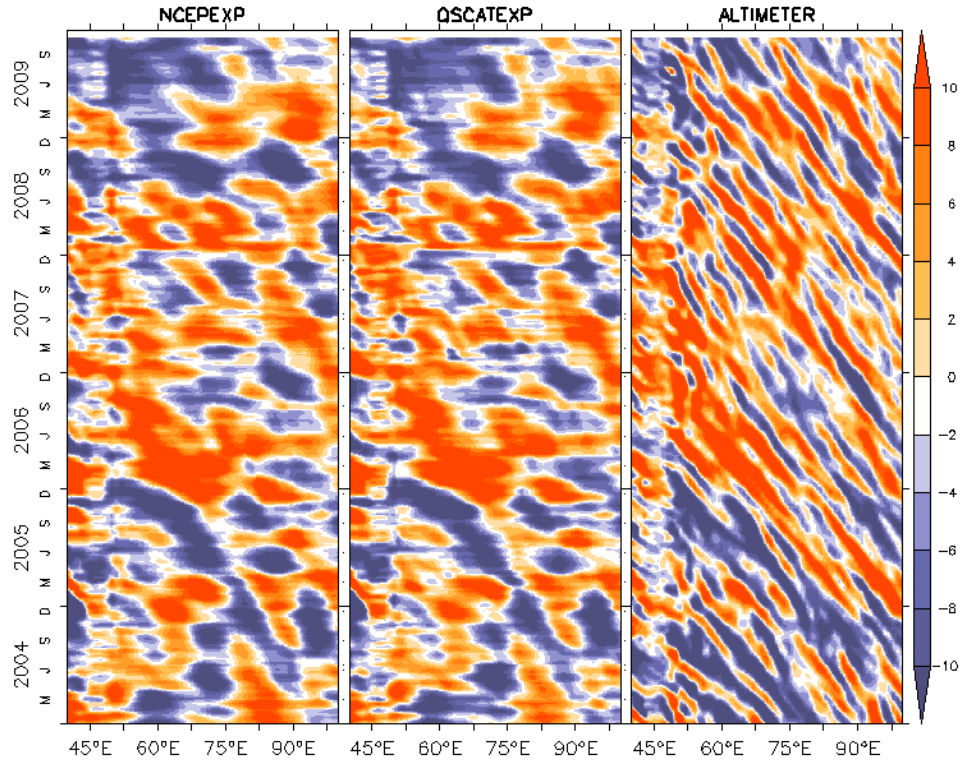

Figure 5.4.3.f. Same as Figure 5.4.3.a, but along 25°S.

Figure 5.4.4 shows the time series of SSHA (2004-2009) derived from the altimeter data, the NCEPEXP and the QSCATEXP averaged over the 8 selected locations in the IO and averaged over the whole IO. Time-series plots suggest that there is an excellent agreement between SSHA from the model and the observations, except CBOB and SEC. At all locations, the model follows the observed structure very well. Statistical parameters such as RMSE, standard deviation and correlation are given in the table 5.4.1. The correlation is generally higher than 0.70 at all locations except CBoB and SEC, where the correlation is slightly less than 0.70. Similarly, the standard deviation of the SSHA at SEC and CBoB shows relatively large values in the model compared to observations, while in other regions it is comparable with the observations. In addition, in the SEC and CBoB regions, the RMSE in the model with respect to the observations is larger than STD of the observations. The statistical relationships are summarized graphically in Taylor diagrams [*Taylor,* 2001] in Figure 5.4.5.

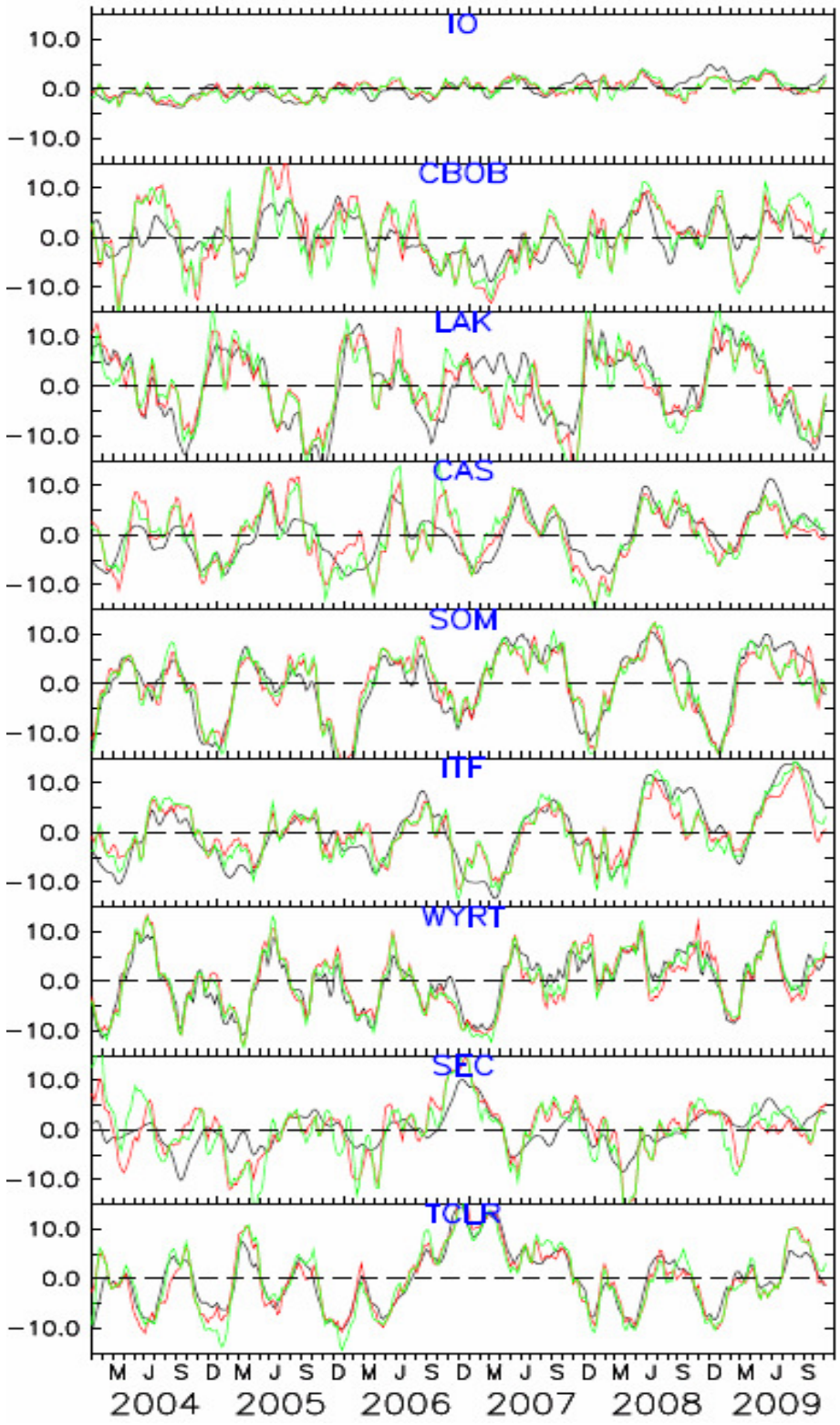

Figure 5.4.4. Time series of SSHA (cm) (2004-2009) derived from altimeter (black), NCEPEXP (red), QSCATEXP (green) averaged over 8 selected regions in the IO and averaged for entire IO (as indicated in the legend) (see section 4 for the description about each region).

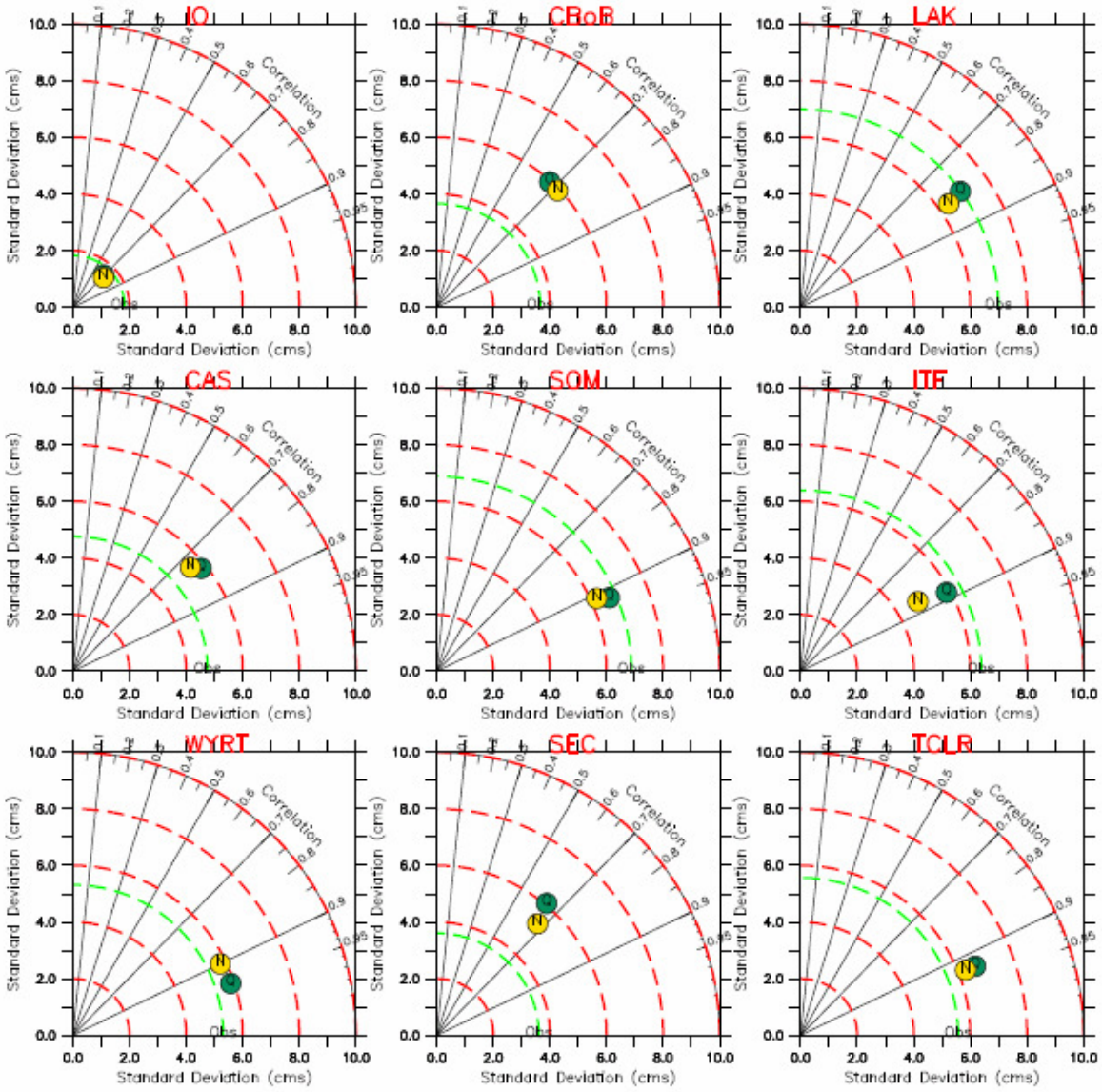

Figure. 5.4.5. Taylor diagram showing the SSHA (cm) performance of two model-runs in comparison with observation for 8 selected regions in the IO and for entire IO (see section 4 for the description about each region).

In order to understand the model's ability to capture the amplitude of intraseasonal variability, an amplitude spectrum was computed for the SSHA from the model and the altimeter. Figure 5.4.6 shows the results for the 8 selected regions in the IO and for the entire IO. The Figure 5.4.6 shows that the model is able to capture the amplitude of intraseasonal and seasonal signal reasonably well. In summary, the model performs well in simulating the SSHA in the IO.

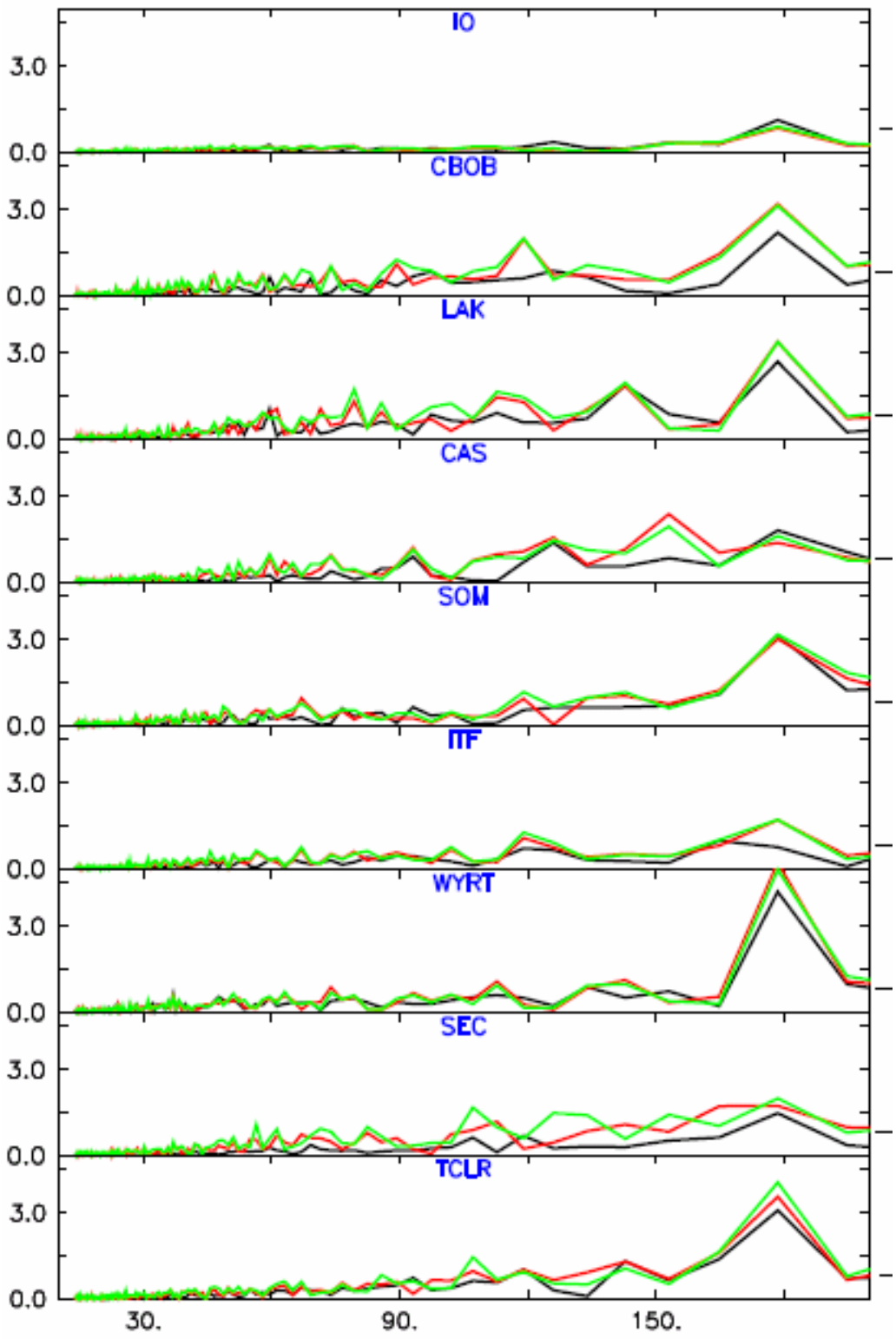

Figure 5.4.6. The FFT amplitude spectrum of SSHA (cm) derived from altimeter (black) NCEPEXP (red), QSCATEXP (green) for the 8 selected regions in the IO and for entire IO (see section 4 for the description about each region).

Table 5.4.1. Statistical comparison of model SSHA (cm) with altimeter data.

Region	STD			RMSE		CORRELATION	
	Altimeter	NCEPEXP	QSCATEXP	NCEPEXP vs altimeter	QSCATEXP vs altimeter	NCEPEXP vs altimeter	QSCATEXP vs altimeter
IO	1.83	1.50	1.57	1.28	1.35	0.72	0.69
CBOB	3.66	5.93	5.96	4.17	4.45	0.72	0.67
LAK	6.99	6.38	6.97	4.00	4.26	0.82	0.81
CAS	4.76	5.54	5.81	3.69	3.67	0.75	0.78
SOM	6.88	6.21	6.63	2.8	2.74	0.91	0.92
ITF	6.39	4.82	5.86	3.34	3.02	0.86	0.88
WYRT	5.31	5.79	5.87	2.47	1.83	0.90	0.95
SEC	3.61	5.31	6.07	3.96	4.69	0.67	0.64
SEYC	5.57	6.27	6.64	2.28	2.57	0.93	0.93

5.5. Ocean current

5.5.1 Mean monthly and seasonal cycle of surface currents

The tropical IO circulation exhibits a unique seasonal reversal of the major currents [*Schott et al.,* 2009] in phase with the monsoons. These current systems are the Somali current (SC), the North Equatorial Current (NEC), the West India Coastal current (WICC), and the East India Coastal current (EICC). The South Equatorial Current (SEC), westward flow south of 10°S, does not undergo any seasonal variation in direction. During the two transition periods between the monsoons (April-May and October-November), a strong eastward jet called the 'Wyrtki Jet' [*Wyrtki,* 1973], occurs in a narrow band trapped within 2º-3º of the equator driven by the equatorial westerly winds.

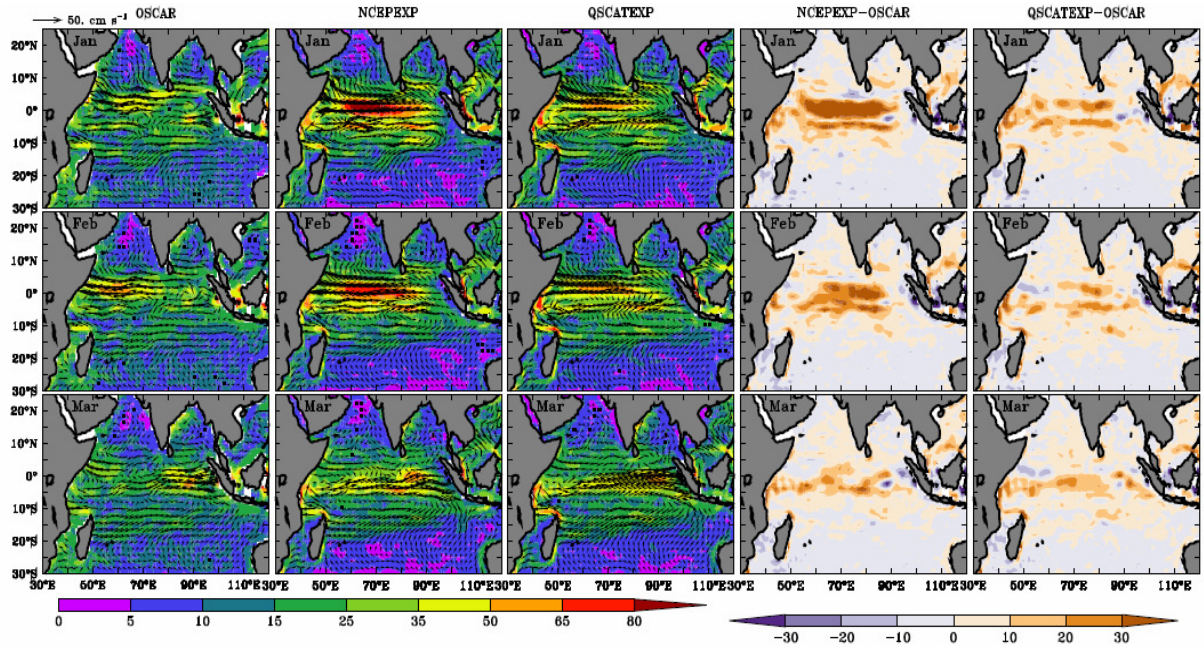

Figure 5.5.1. Monthly evolution of multiyear average of (2004-2009) of ocean surface currents (cm s^{-1}) derived from (a) OSCAR (b) NCEPEXP (c) QSACTEXP and difference between model and observation (d) NCEPEXP and OSCAR (e) QSCATEXP and OSCAR during January-March.

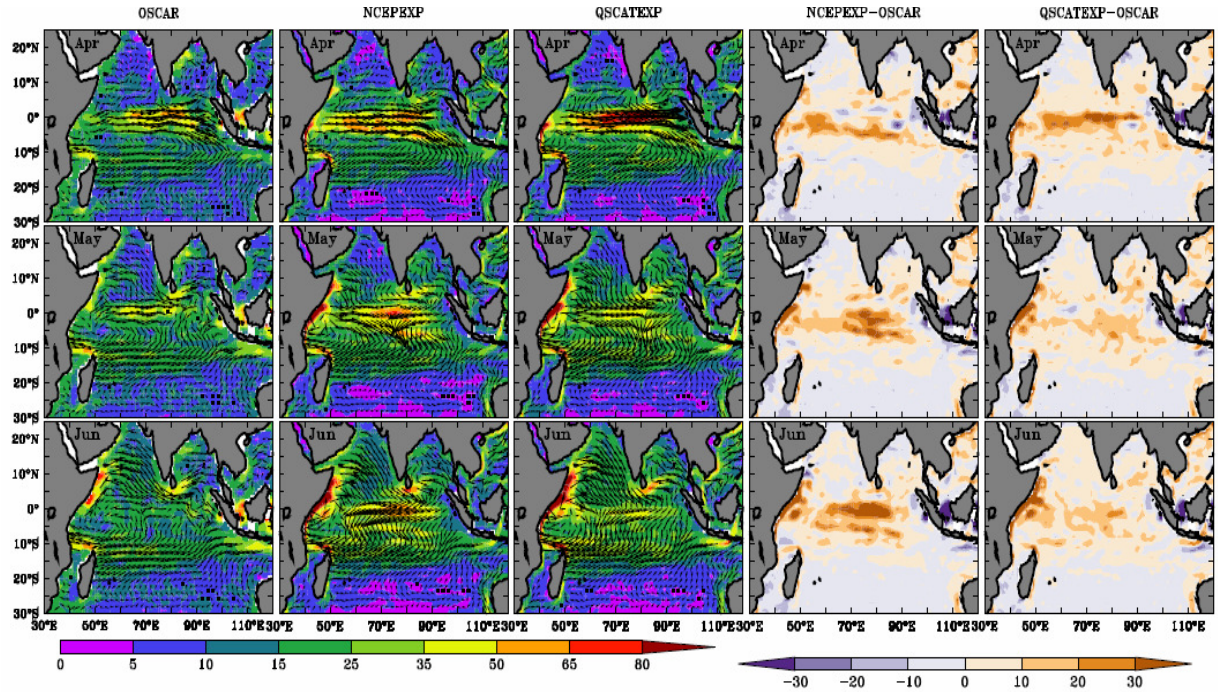

Figure 5.5.1. (continue) during April-June

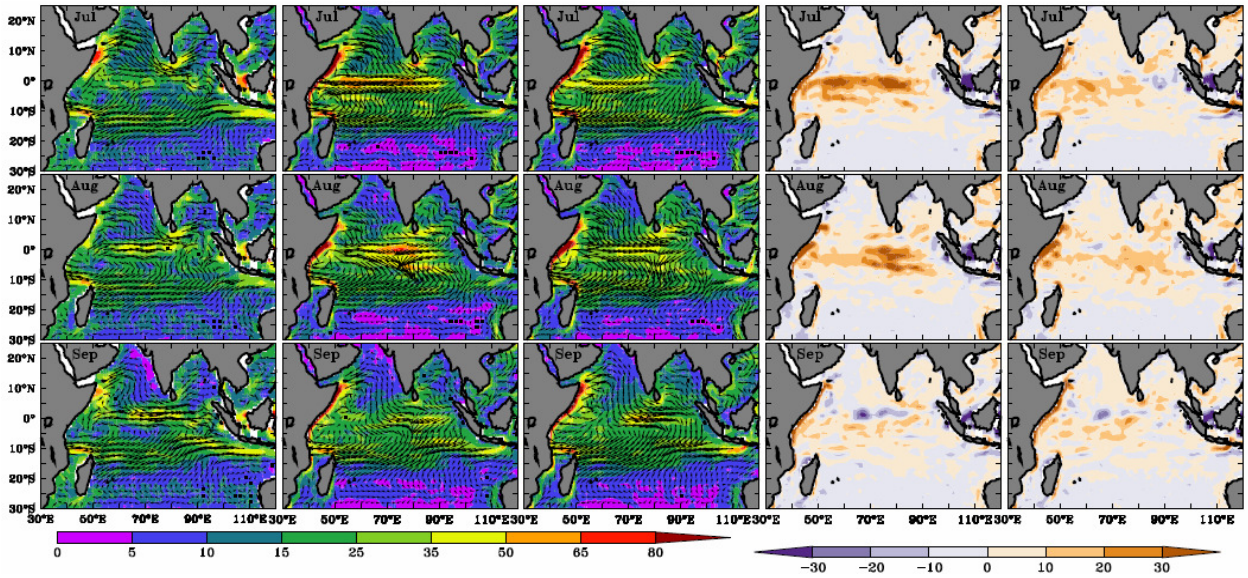

Figure 5.5.1. (continue) during July-September.

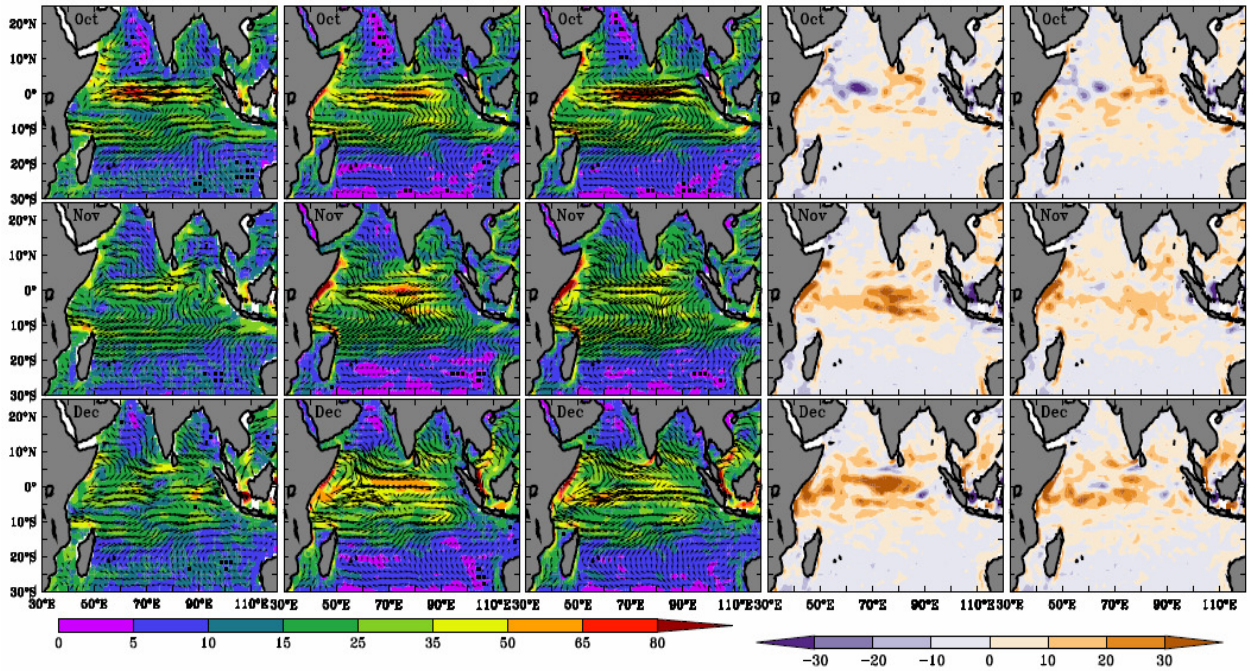

Figure 5.5.1. (continue) during October-December.

The monthly surface current pattern is compared with the monthly climatology of OSCAR currents obtained for the period 2004-2009. The monthly evolution of the surface currents in OSCAR, the NCEPEXP and the QSCATEXP along with their respective biases are shown in the Figure 5.5.1. Both model runs are able to capture the circulation pattern reasonably well. However, the equatorial flow simulated by the NCEPEXP during summer monsoon is westward unlike in the observations. This discrepancy, both in magnitude and

direction, in the NCEPEXP is improved in the QSCATEXP. On the other hand, biases are relatively small (< 10 cm s^{-1}) during March and September-October in both model experiments.

Seasonal cycle: The seasonal cycle of the surface currents are compared with the climatologies of drifter and OSCAR currents. The seasons are defined as winter Monsoon (December-January-February), spring inter-monsoon (March-April-May), summer monsoon (June-July-August-September) and fall inter-monsoon (October-November). The current patterns in the model experiments along with their corresponding biases relative to the observed currents are shown in Figure 5.5.2. As was the case with the monthly evolution of the currents, the mean seasonal surface currents are in agreement with the observations except at the equator. The SEC, located south of 10˚S, flows westward during all the seasons and this is captured by the model well. The model is also able to resolve the seasonal reversal of the coastal current systems and a detailed analysis of these currents will be given in section 5.5.3.2. During the Winter Monsoon, both the model simulations over-estimate the strength of the equatorial currents compared to the OSCAR currents (Figure 5.5.2.a). The difference is larger in NCEPEXP. Both model runs simulate the westward flowing current which extends throughout the equatorial regime. However, this current system is noticeable only west of 80°E in the OSCAR currents.

The eastward flowing Wrytki Jets which develop during inter-monsoon periods appear in both model simulations with the same timing. The speed of these jets is comparable with observations (Figure 5.5.2.b, 5.5.2.d). QSCATEXP produces slightly stronger and more spatially extended jets relative to NCEPEXP. The eastward flowing summer monsoon currents (Figure 5.5.2.c) just north of equator seen in the model are in agreement with the observations. There is a strong westward flow in NCEPEXP along the equator which does not occur in the observations. However, QSCATEXP does simulate the circulation pattern as

exhibited by the drifter and OSCAR currents. In summary, QSCATEXP has a relatively better simulation of the equatorial currents both in magnitude and direction than NCEPEXP.

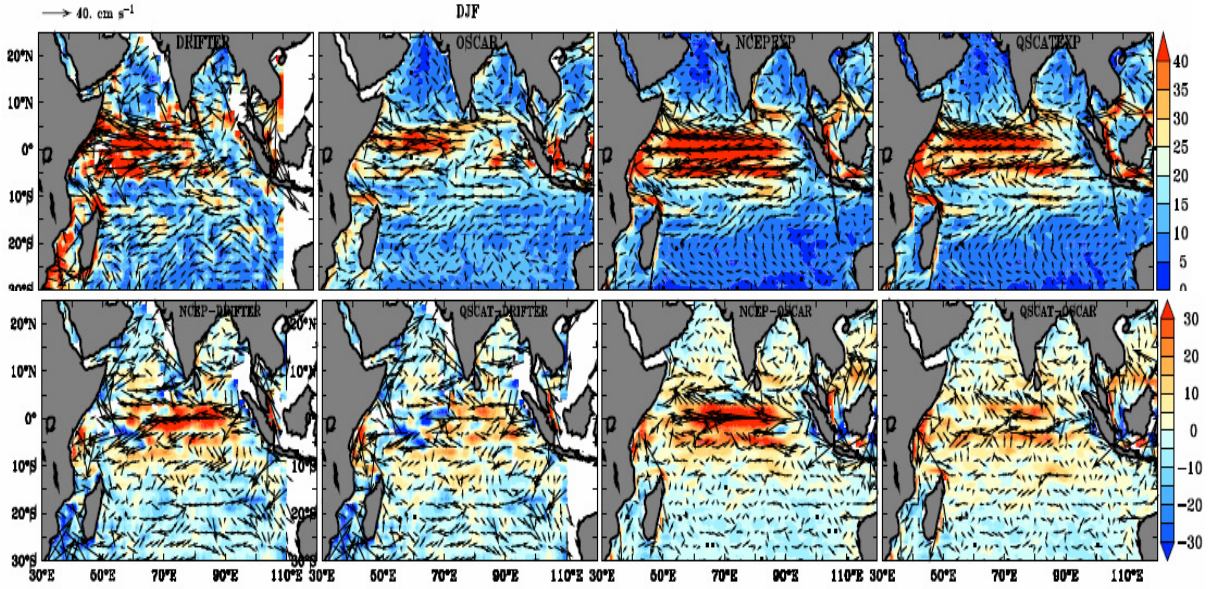

Figure 5.5.2.a. Climatology of surface currents (cm s^{-1}) derived from Drifter, multiyear average (2004-2009) of surface current derived from OSCAR, NCEPEXP and QSCATEXP (top panel; left to right) for the Winter Monsoon season (Dec-Jan-Feb). Lower panel shows the bias from Observations.

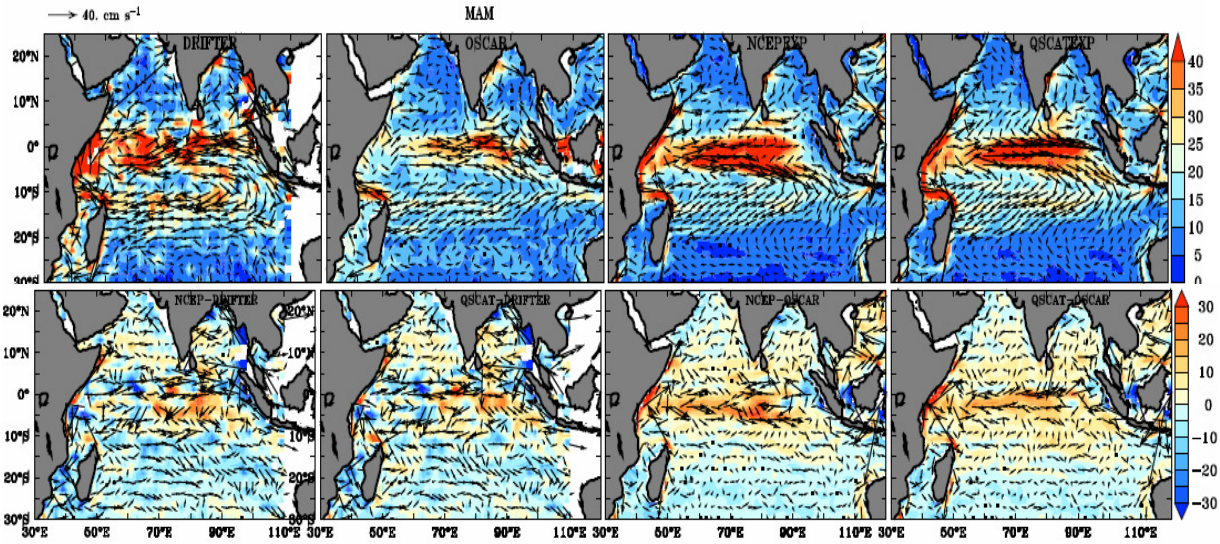

Figure 5.5.2.b. Same as Figure 5.5.2.a, but for the Spring inter-monsoon season (Mar-Apr-May).

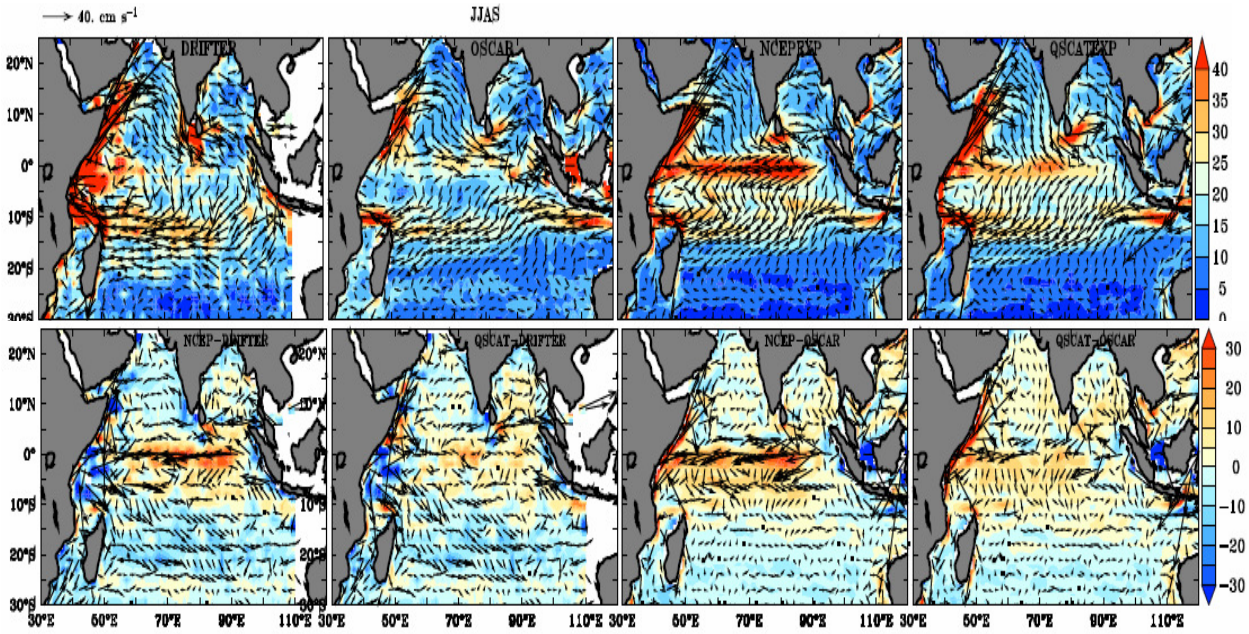

Figure 5.5.2.c. Same as Figure 5.5.2.a, but for the Summer Monsoon season (Jun-Jul-Aug-Sep).

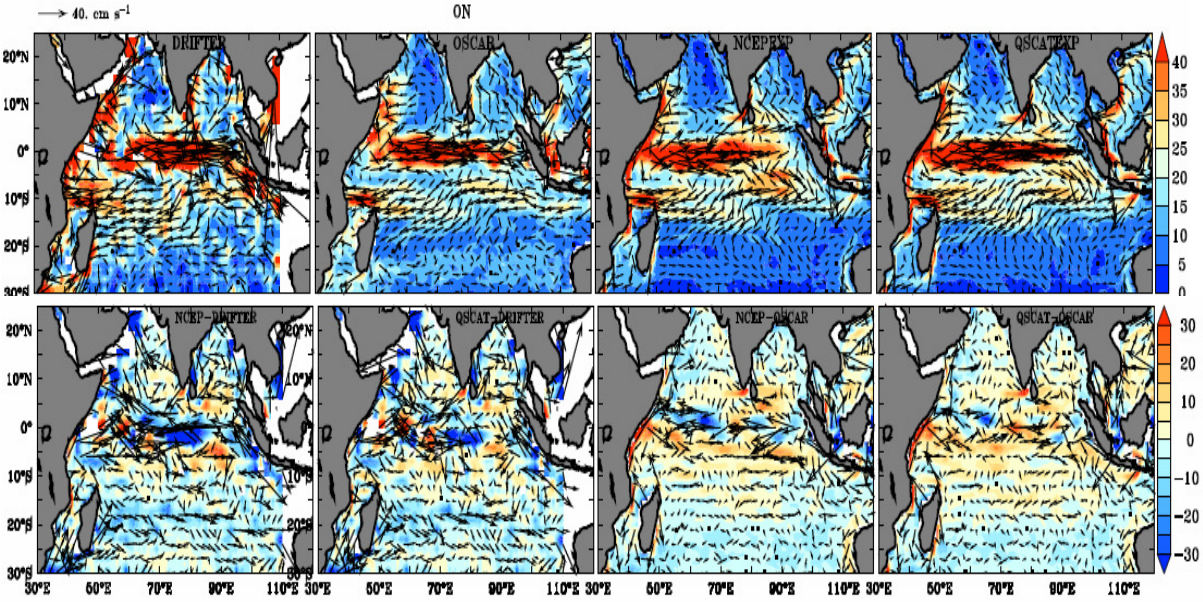

Figure 5.5.2.d. Same as Figure 5.5.2.a, but for the fall inter-monsoon season (Oct-Nov).

Annual Cycle: The annual average of the surface currents are shown in Figure 5.5.3. As seen in the monthly and seasonal evolution, both the model runs are able to capture the circulation pattern fairly well with the exception of the immediate equatorial region in the NCEPEXP. The QSCATEXP simulates the eastward flowing equatorial current as seen in the

observations, while the NCEPEXP produces westward currents west of 90ºE along the equator. Elsewhere, both model runs are comparable with the observations. Figure 5.5.4 shows the statistical measures such as the standard deviation, the RMSE and the correlation of the zonal surface currents for the period 2004-2009. The high variability along the equator in the OSCAR currents is replicated by both model runs. The RMSE is less than the standard deviation in the QSCATEXP whereas in the NCEPEXP, the RMSE is as large as the standard deviation. The improvement of the current in equatorial region in QSCATEXP over NCEPEXP is clearly visible from the RMSE pattern. Though a positive correlation with observations is found overall in both simulations, the QSCATEXP correlation exceeds 0.75 in the equatorial regions.

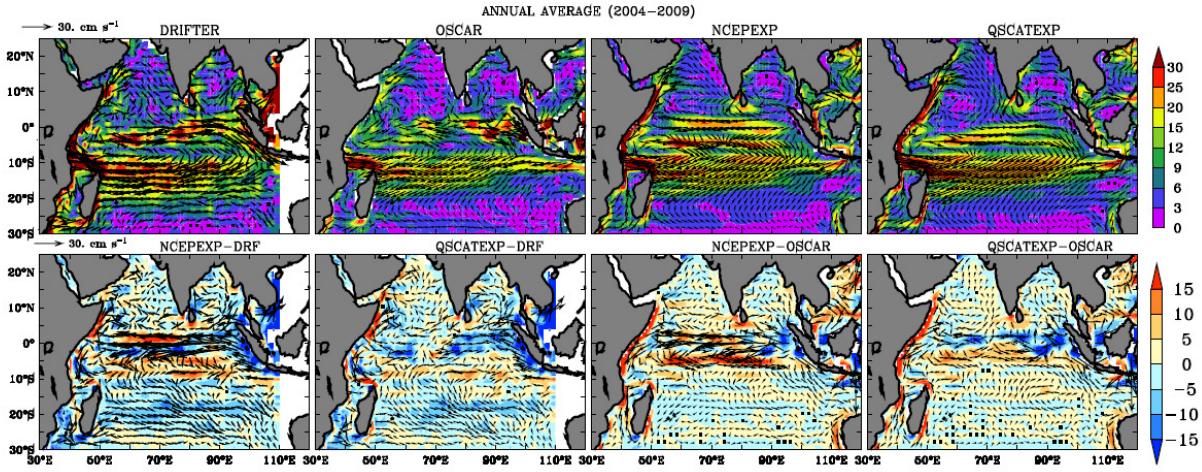

Figure 5.5.3. Annual averaged surface currents (cm s^{-1}) derived from drifter climatology, OSCAR, NCEPEXP and QSCATEXP (from left panel to right panel respectively). All the currents are averaged through the period 2004-2009. Lower panel shows the difference between model currents (NCEPEXP and QUIKEXP) and observations (Drifter and OSCAR).

The differences between the surface zonal currents generated by the model simulations show overestimated westward equatorial currents in the NCEPEXP (Figure 5.5.5.a). The reason for this large discrepancy between NCEPEXP and QSCATEXP have been analysed in detail. Figure 5.5.5.b shows the hovmollor diagram of the zonal surface currents in NCEPEXP, QSCATEXP and the difference between them. The hovmoller diagram of the

zonal surface currents along the equator (2˚S-2˚N) shows that differences as large as 60 cm s^{-1} occurred through the whole period 2004 to 2009. Any difference in the current patterns between the QSCATEXP and the NCEPEXP can be attributed to the difference in the respective momentum forcing. The surface zonal wind stress from NCEP and QuikSCAT along the equator (2˚S-2˚N) and difference between them are shown in Figure 5.5.5.c. The NCEP wind stress shows a large westward wind stress bias compared to QuikSCAT. In addition, wind stresses are greatly underestimated in NCEP compared to QuikSCAT. It was noted by *Smith et al*. [2001] that NCEP underestimates the surface winds over most of the tropics. *Goswami and Sengpta* [2003] also documented the deficiency of the NCEP reanalysis surface winds over the equatorial IO by comparing with QuikSCAT winds. They showed that the major differences between the two wind products occur in the equatorial IO east of 60˚E during both monsoon seasons and they attributed this difference to a systematic error in the precipitation in the NCEP reanalysis. It is reasonable to speculate that the difference in surface currents shown in the NCEPEXP and QuikSCAT is due to the error in NCEP2 surface winds in this region. However, a more detailed analysis is required to sort out the exact causes of this large current difference.

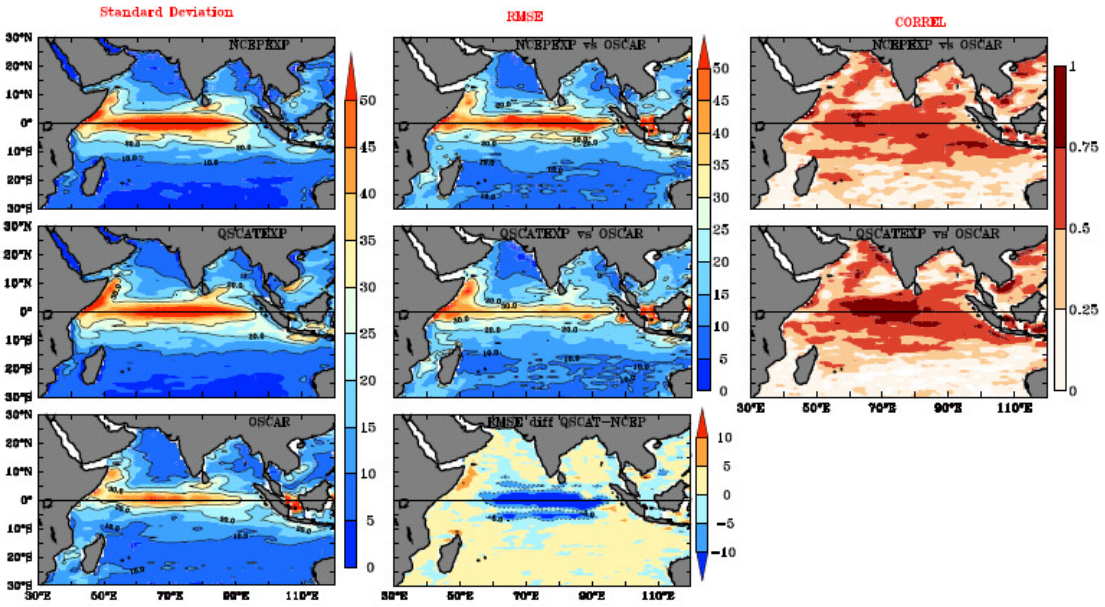

Figure 5.5.4. (left) The standard deviation of surface zonal currents (cm s^{-1}) derived from NCEPEXP, QSCATEXP and OSCAR (2004-2009). The RMSE (middle panels), correlation

(right panels) between the model surface zonal currents and OSCAR (top) NCEPEXP and (middle) QUIKEXP during 2004-2009. In the middle panel, last row shows the difference in RMSEs of QUIKEXP and NCEPEXP with respect to OSCAR current.

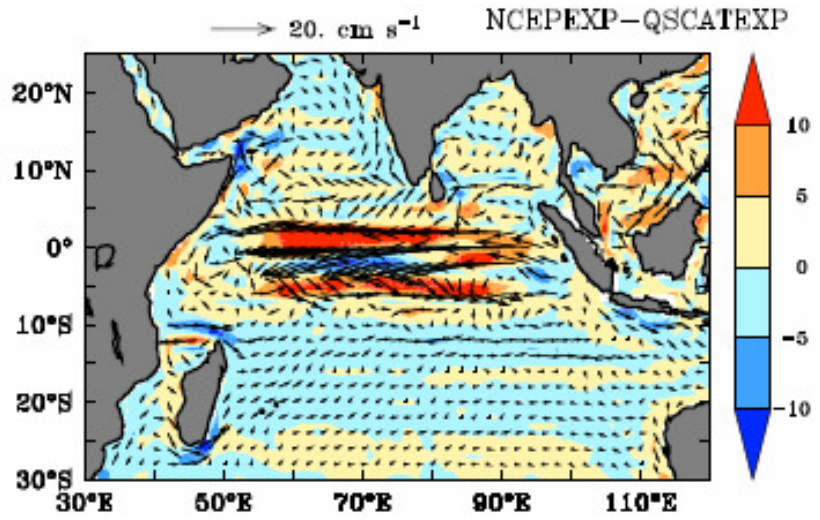

Figure 5.5.5.a. Difference between annually averaged (2004-2009) surface zonal currents (cm s^{-1}) derived from NCEPEXP and QSCATEXP.

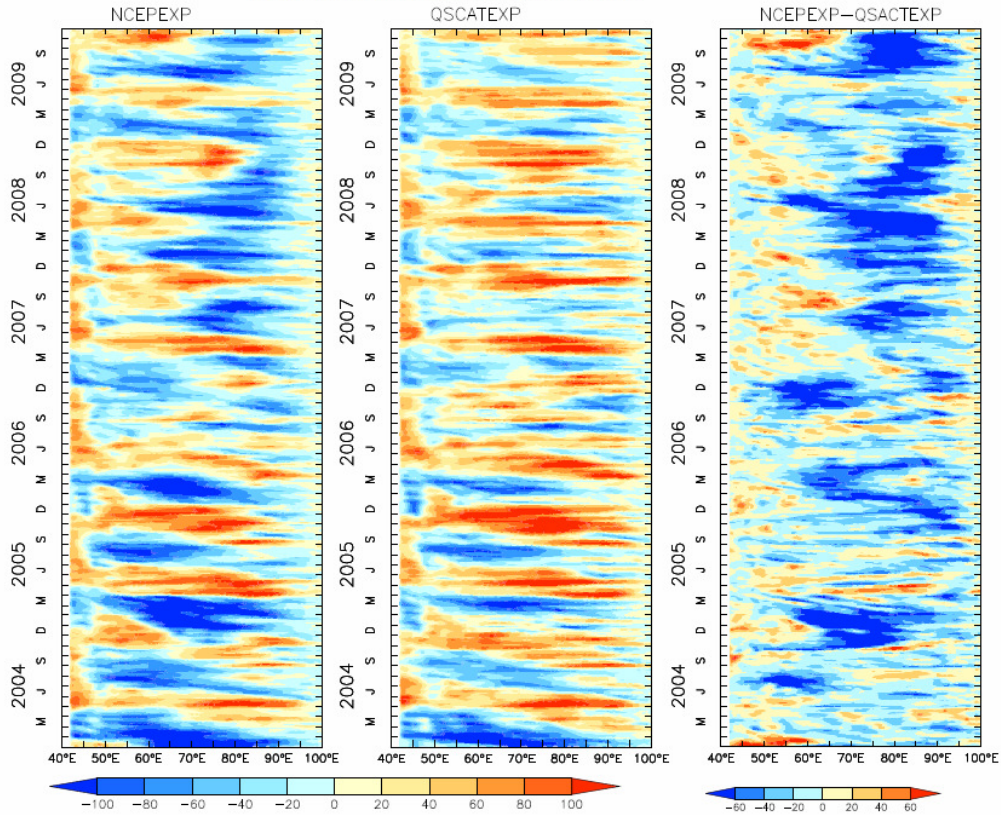

Figure 5.5.5.b. The surface zonal currents (cm s^{-1}) along the equator (2°S-2°N) simulated by NCEPEXP and QSCATEXP and the difference between them.

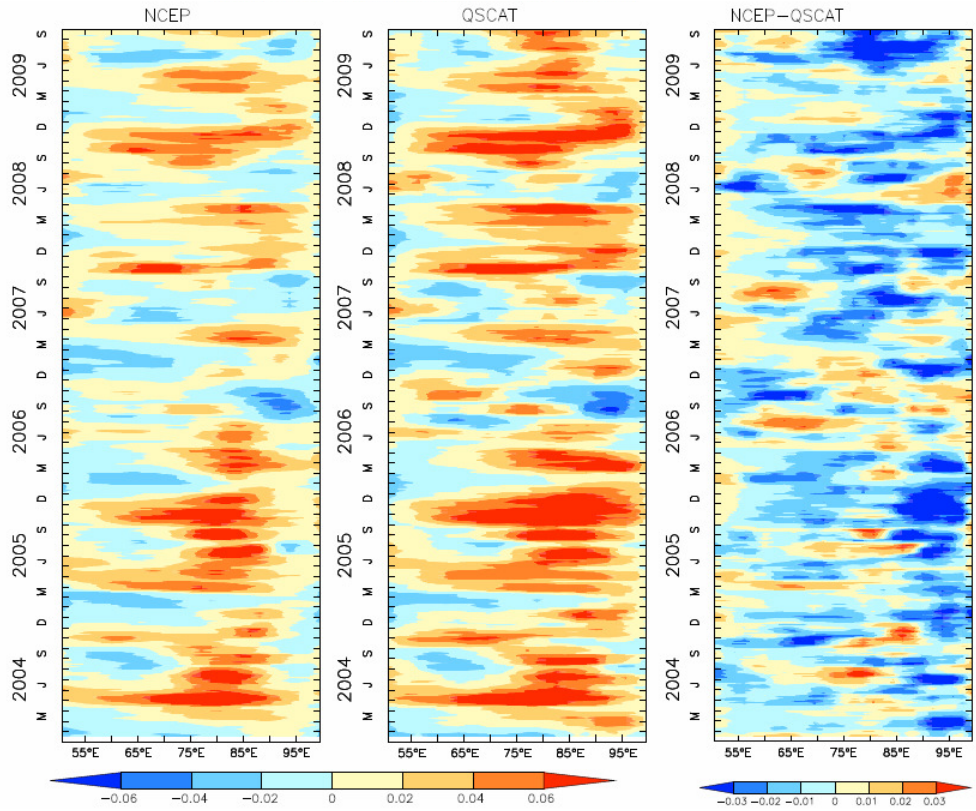

Figure 5.5.5.c. The zonal wind stress (N m^{-2}) along the equator (2°S-2°N) from NCEP2 and QuikSCAT scatterometer and the difference between them.

5.5.2 Spatial variability of surface currents in the northern Indian Ocean

The ocean surface current variability in the model simulations was analyzed for the three most dynamic regions of the IO- the Somali Current, the Arabian Sea and the Bay of Bengal. Comparisons are performed using near surface Ekman and geostrophic currents estimated from satellite QuikSCAT winds and AVISO SSHA.

Somali Current: The Somali current (SC) system is located off the Somali Coast and undergoes seasonal reversals with the monsoons. The SC flows equatorward during the winter monsoon and poleward during the summer monsoon with speeds that can exceed 100 cm s^{-1}. The SC can develop different gyres and cells depending on the season. During the summer monsoon, three cells will generally form, the Socotra cell, the Great Whirl and the Southern Gyre. Figure 5.5.6 shows the Somali current simulated by NCEPEXP, QSCATEXP and the near surface circulation estimated from satellite data during the summer (top panel) and

winter (bottom panel) monsoon seasons. The model simulations replicate the seasonal reversal of the Somali current, displaying poleward flow during the summer monsoon and equatorward flow during the winter monsoon (figure 5.5.6, lower panel). The gyres expected to prevail during the summer monsoon and seen in the currents computed from the satellite data are also captured by both simulations.

Arabian Sea: The main circulation features in the Arabian Sea during the monsoon seasons include the West Indian Coastal current (WICC), and the summer and winter monsoon currents. Both model simulations are able to generate the seasonal reversal of these currents with the monsoons (Figure 5.5.7). The reversal of the WICC is captured well by the model during both monsoons. During the winter monsoon, the anticyclonic flow in the south eastern Arabian Sea is well captured by both model runs.

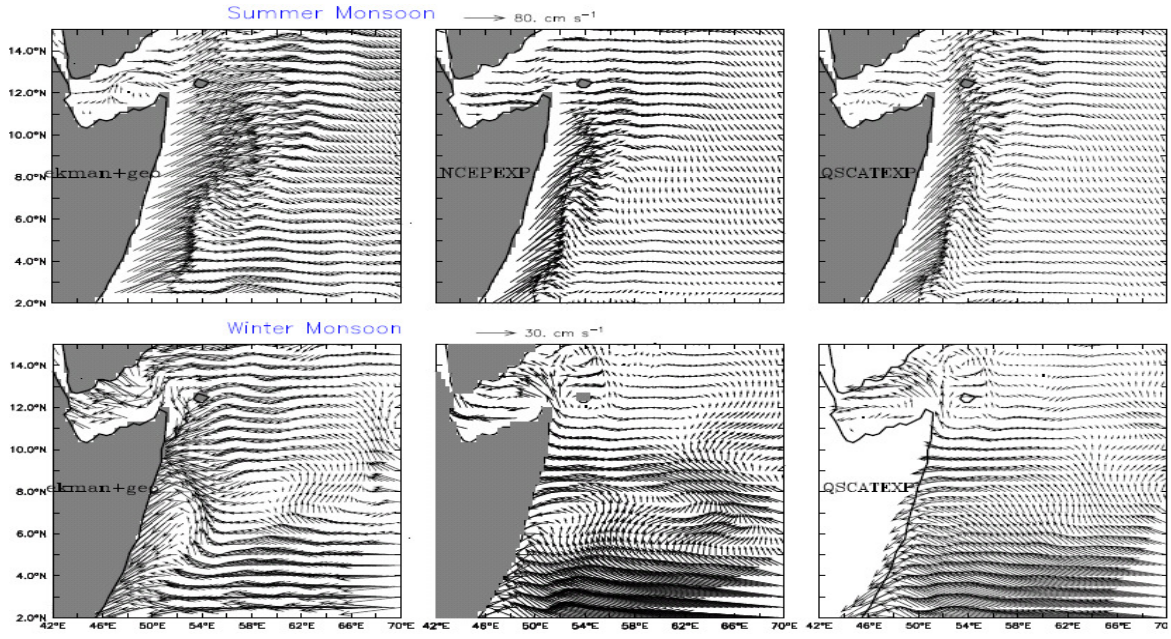

Figure 5.5.6. Comparison of surface currents (cm s^{-1}) over Somali region simulated by NCEPEXP and QSCATEXP with combined Ekman and geostrophic currents during Summer and Winter monsoons.

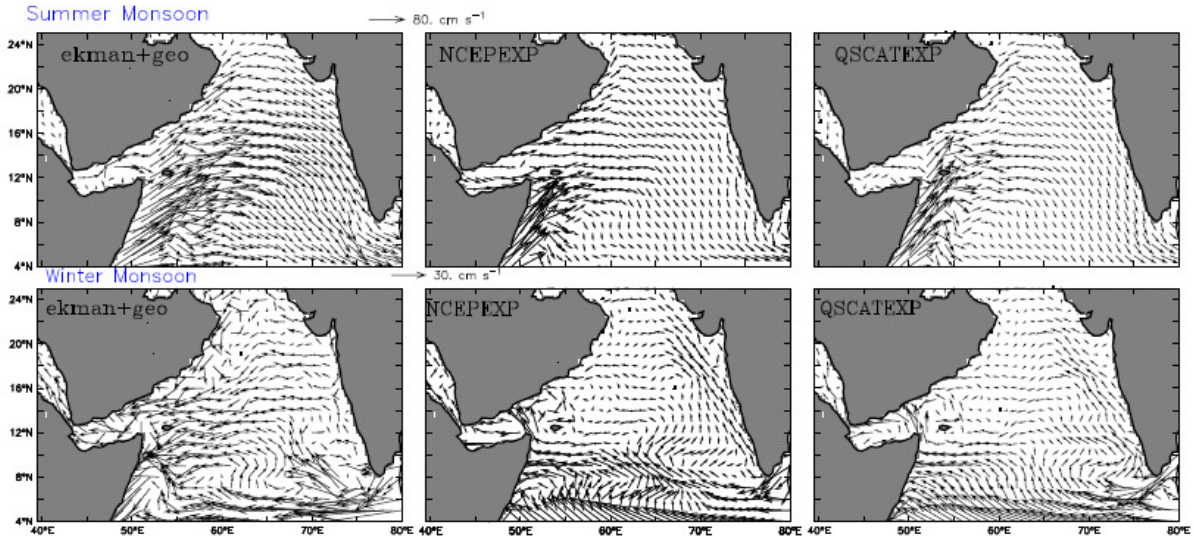

Figure 5.5.7. Comparison of surface currents (*cm* s^{-1}) over Arabian Sea simulated by NCEPEXP and QSCATEXP with combined Ekman and geostrophic currents during summer and winter monsoons.

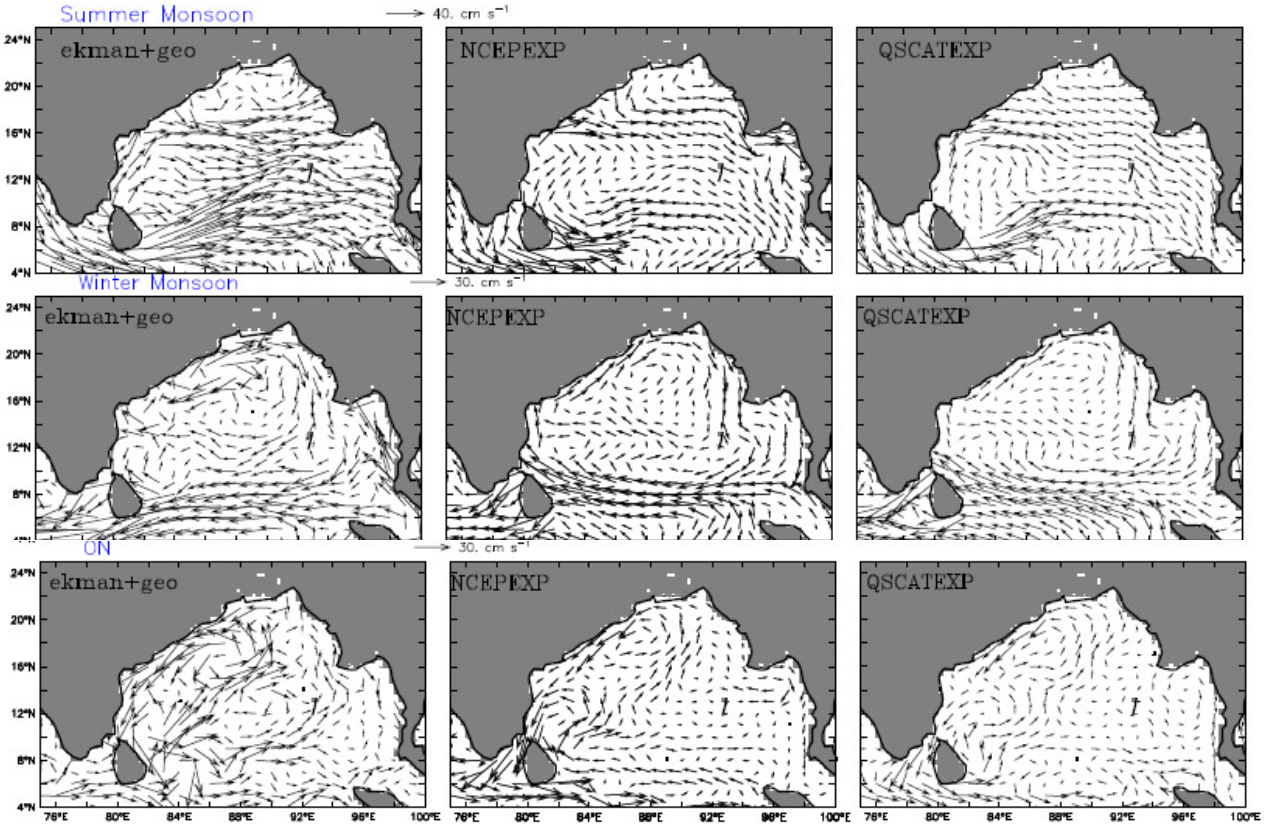

Figure 5.5.8. Comparison of surface currents (cm s^{-1}*) over Bay of Bengal simulated by NCEPEXP and QSCATEXP with combined Ekman and geostrophic currents during Summer monsoon (JJA), post-monsoon (ON) and Winter monsoons (JFM).*

Bay of Bengal: The circulation pattern in the Bay of Bengal during the summer and winter monsoons and during October-November is shown in Figure 5.5.8. Earlier studies show the existence of a coastal current along the eastern boundary of the Bay, known as the East India Coastal Current (EICC) [*Shetye et al.,* 1996]. The EICC also has a seasonal reversal, flowing north-eastward from February until September with a strong peak in March–April and south-westward from October to January with the strongest flow in November [*Shankar et al.,* 2002]. The model captures the seasonal cycle of the EICC, reasonably well. The anticyclonic gyre observed during the winter monsoon and the eastward current in the northern Bay during the summer monsoon are also reasonably well captured by the model.

The study by *Vinayachandran et al*. [1999] and *Rao et al.* [2006a] showed that during the summer monsoon, the so-called summer monsoon current (SMC) curves around Sri-Lanka and intrudes into the southwestern Bay. The intrusion of the SMC into the southwestern Bay is captured by both models. Following the end of the summer monsoon, the southward flow of the EICC carries low saline waters from the northern Bay around Sri Lanka to SEAS. The observational and modelling study by *Vinayachandran et al.* [2005] showed that bifurcation of the EICC around the west coast of Sri-Lanka, and the advection of low saline waters carried by the EICC current into the south central Bay. However, in the model low salinity water reaches SEAS as a strong leakage through the Palk Strait (Figure 5.5.8, middle panel). The Indo-Sri Lanka channel (ISLC) consists of the shallow (< 12 m) Palk Bay and Palk Strait to the north and the relatively deeper Adam's region to the south; the two regions separated by the Pamban Pass and Adam's Bridge. The Pamban Pass is a narrow pass of about 3 km width with shallow depths of < 6 m while Adam's Bridge is approximately 30 km in length with shallow depths of < 5 m [*Rao et al.,* 2011]. The study by *Rao et al.* [2011] further suggests that both the shallow Pamban Pass and Adam's Bridge in the ISLC act as barriers and limit the southward flow of low salinity waters into the Gulf of Mannar in the south during winter. The deeper bathymetry in this region in the model (40 m) might permit

more flow through the ISLC, instead of directing flow around Sri-Lanka. The resulting low saline water in the SEAS during these months (Figure 5.3.2) in the model simulation is likely the consequence of this unrealistic flow. This erroneous flow pattern could be corrected by reducing the depth of the Indo-Sri Lanka Channel or by simply closing it.

It is interesting to note that the winter monsoon current simulated by the model flows northward along the east coast of Sri-Lanka, but in the observations this current curves around the southern tip of Sri-Lanka and flows westward. The role of the winter monsoon current in carrying fresh water from eastern Bay to SEAS, particularly during later part of winter monsoon is documented by *Vinayachandran et al.* [2005]. The large positive bias in the salinity in SEAS as shown Figure 5.3.2, during January-February may be due to this unrealistic current around Sri-Lanka.

5.5.3 Intraseasonal and interannual variability

The existence of large intraseasonal and interannual variabilities in the zonal and meridional components of the surface current in the IO has earlier been reported [*Murty et al.,* 2002*; Sengupta et al.,* 2004]. The model's ability to capture these intraseasonal and interannual signals is assessed using RAMA observations. The time series observations of currents at 10 m depth are available in the Bay of Bengal, the south western IO, and the equatorial regions and validations are done at these locations.

Figure 5.5.9 shows the temporal evolution of the zonal and meridional components of the currents from the model and the RAMA buoys. Statistical parameters such as RMSE, standard deviation and correlation are given in the table 5.5.2. Using Taylor diagrams [*Taylor, 2001*] the statistical relationships are summarized graphically in Figure 5.5.10. It is clear from the time series that, at most locations, QSCATEXP currents agree more closely in amplitude and phase with RAMA currents than do the NCEPEXP currents. The superior performance of QSCATEXP is most notable at 12ºS, 67ºE; 1.5ºN, 80.5ºE and 0˚N, 80.5ºE where QSCATEXP successfully corrects the westward bias in the NCEPEXP currents.

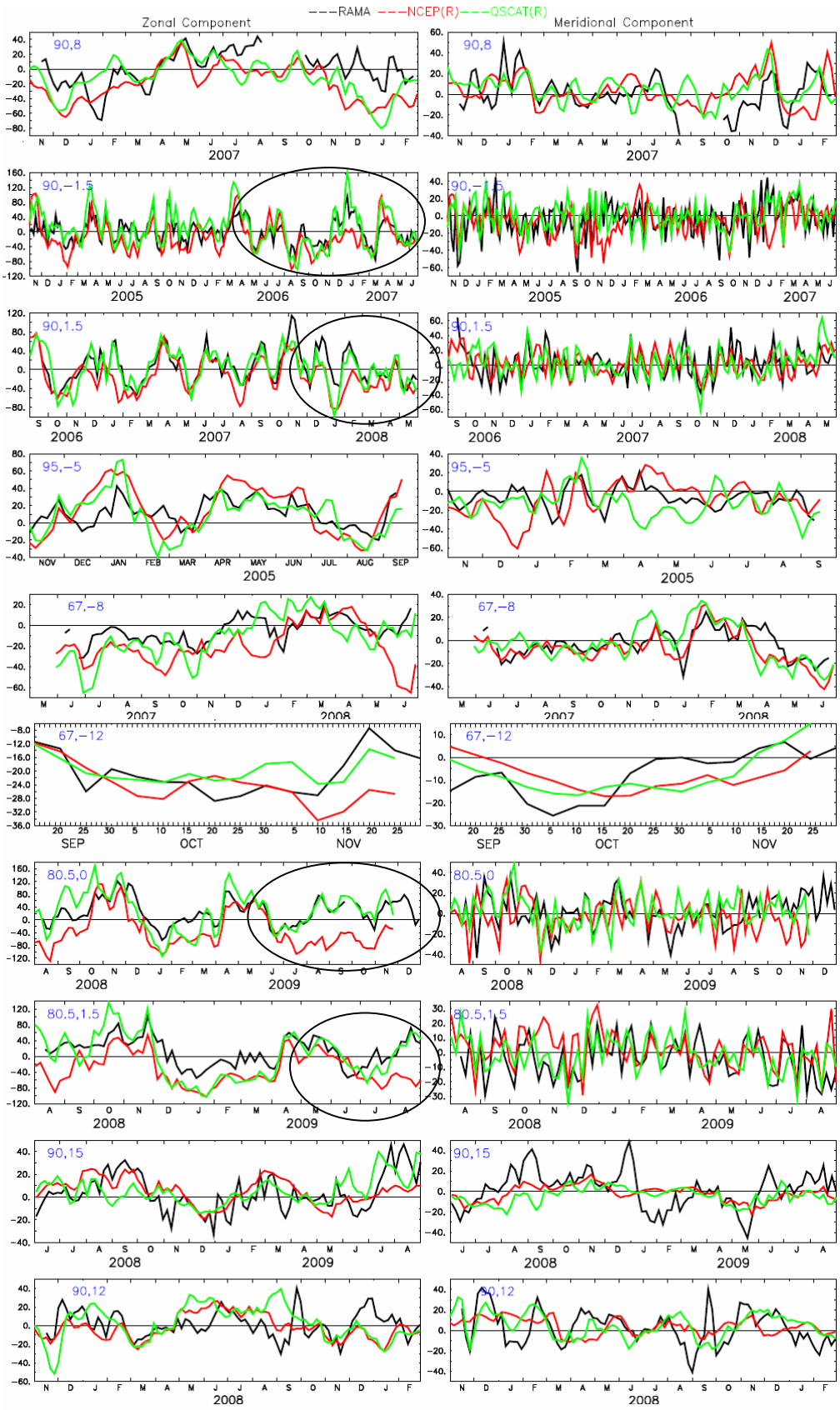

Figure 5.5.9. Surface currents (cm s^{-1}) simulated by NCEPEXP, QSCATEXP compared with currents observed by RAMA buoys.

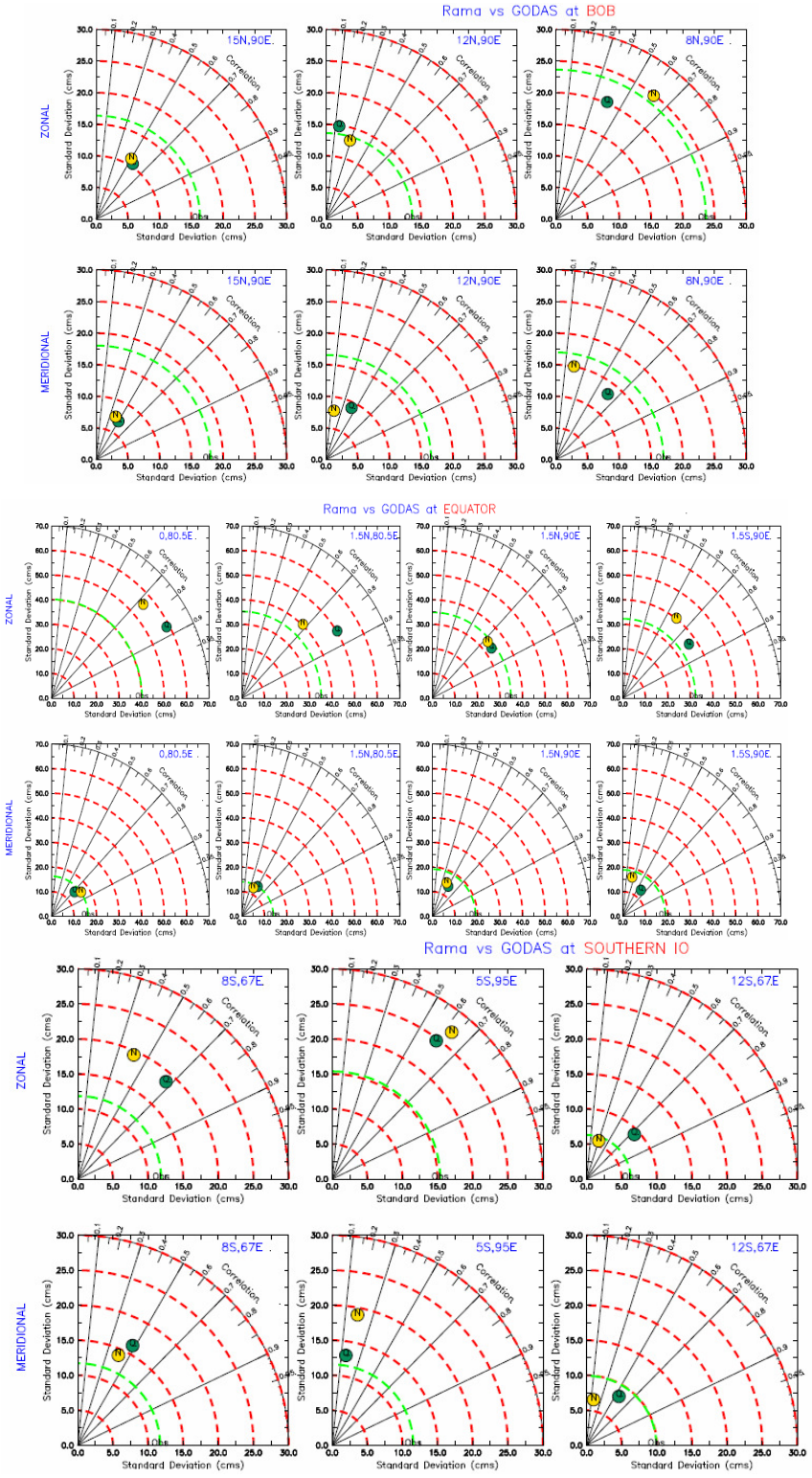

Figure 5.5.10. (Continue) Taylor diagrams indicating the statistical analysis of currents (cm s^{-1}) simulated by NCEPEXP (yellow circle) and QSCATEXP (green circle) at observations measured by TRITON buoys and RAMA buoys.

The standard deviations of the currents in model experiments are comparable with the observations at most buoys locations, particularly in the QSCATEXP. In general, the QSCATEXP currents correlate with RAMA currents better than those of NCEPEXP and the

RMSE of QSCATEXP currents is less than that of NCEPEXP. The statistics further emphasize the improvements in the model current field that occurred when QuikSCAT winds were introduced.

Table 5.5.2. Statistical comparison of model derived currents (cm s^{-1}) with currents derived from RAMA buoys.

Location		Standard Deviation			RMSE		Correlation	
		RAMA	NCEPEXP	QSCATEXP	NCEPEXP	QSCAEXP	NCEEXP	QSCATEXP
0, 80.5˚E	U	40.15	55.77	58.70	68.87	37.53	0.72	0.82
	V	16.27	16.42	15.21	21.89	17.62	0.01	0.4
1.5˚N, 80.5˚E	U	35.19	40.40	50.32	54.98	40.09	0.67	0.84
	V	13.98	12.70	13.96	15.84	13.65	0.40	0.50
1.5˚N, 90˚E	U	34.86	33.61	36.37	33.32	24.04	0.73	0.77
	V	19.18	15.09	18.92	18.95	20.84	0.42	0.40
1.5˚S, 90˚E	U	32.26	40.28	36.63	37.26	27.24	0.59	0.80
	V	18.90	16.41	15.90	21.92	15.40	0.25	0.44
15˚N, 90˚E	U	16.36	11.05	11.40	14.63	14.63	0.50	0.55
	V	18.03	07.46	7.76	16.78	16.73	0.41	0.50
12˚N, 90˚E	U	13.60	13.00	14.85	16.09	19.13	0.29	0.14
	V	16.55	07.84	11.55	17.15	15.78	0.16	0.44
8˚N, 90˚E	U	23.65	24.87	25.80	30.37	24.02	0.62	0.50
	V	16.96	15.02	13.20	20.68	19.99	0.19	0.40
8˚S, 67˚E	U	11.86	19.43	18.73	23.15	16.50	0.41	0.65
	V	11.71	14.10	16.44	10.44	13.54	0.73	0.48
5˚S, 95˚E	U	15.37	27.00	23.98	21.25	18.81	0.63	0.60
	V	11.54	18.98	12.99	20.39	15.25	0.19	0.12
12˚S, 67˚E	u	06.28	05.72	3.70	07.80	4.50	0.30	0.73
	v	09.93	06.60	8.90	10.96	8.90	0.16	0.55

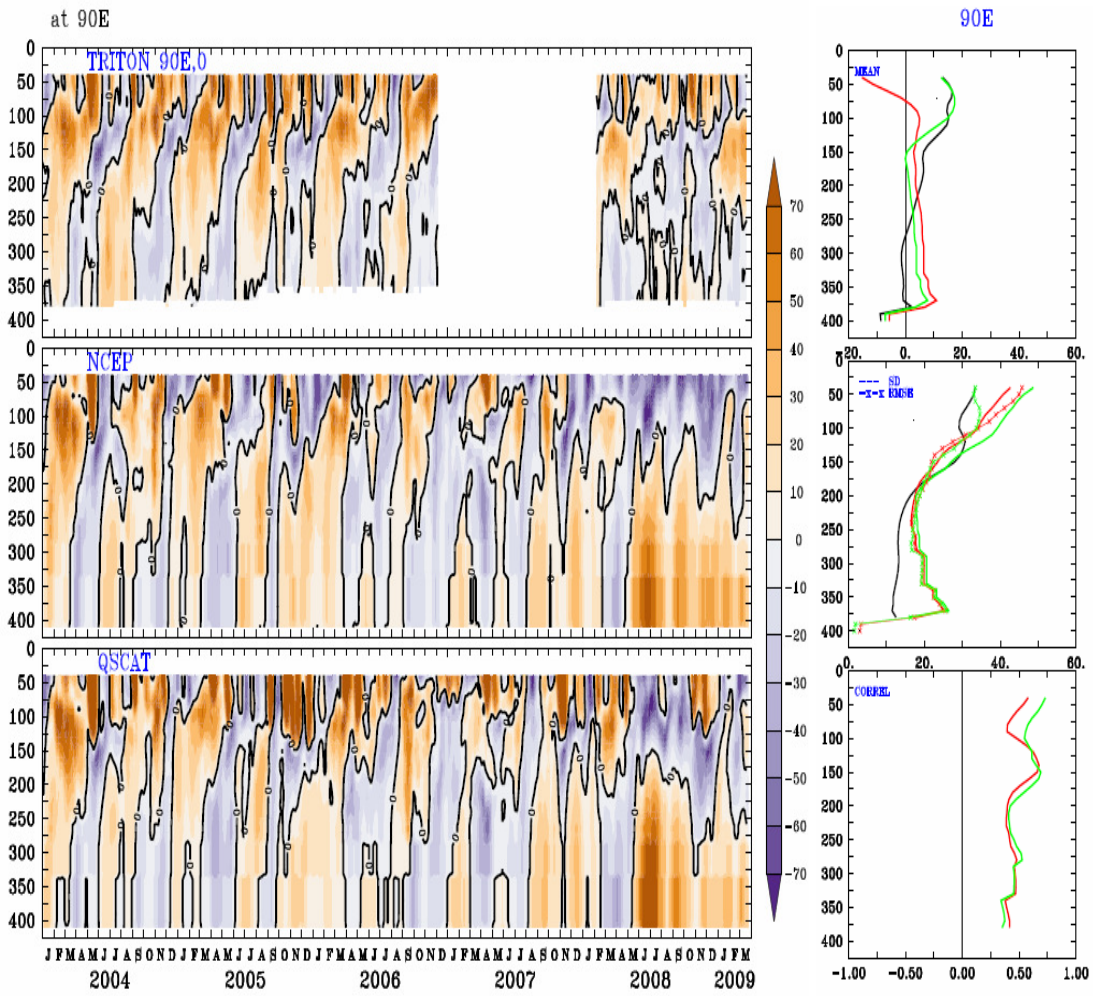

Figure 5.5.11.a. Profiles of zonal current (cm s^{-1}) from ADCP mooring, NCEPEXP and QUIKEXP at Equator, 90°E. The right side of plot shows the statistical parameters such as Mean (top) [QUIKEXP (green) NCEPEXP (red) and ADCP (black)], RMSE (middle) between model and observation [dashed line; QUIKEXP vs ADCP (green), NCEPEXP vs ADCP (red)] and standard deviation (middle) of model and observation [thin line; QUIKEXP vs ADCP (green), NCEPEXP vs ADCP (red)]and correlation(bottom) between model and observation [QUIKEXP vs ADCP (green), NCEPEXP vs ADCP (red)].

Neither of the model simulations could capture the large intraseasonal variability in the Bay of Bengal. However, the model could reproduce the seasonal variability seen in the buoy observations (see Figure 5.5.10; 15°N, 90°E). It is worth mentioning here that, the magnitude of the currents is relatively small (40 cm s^{-1}) in the Bay as seen from Figure 5.5.9. The relatively poor performance in the Bay may be associated with the inability of the model

to resolve the small scale variability prevailing in this region and also with the prescription of an average annual freshwater influx which cannot produce a realistic surface salinity.

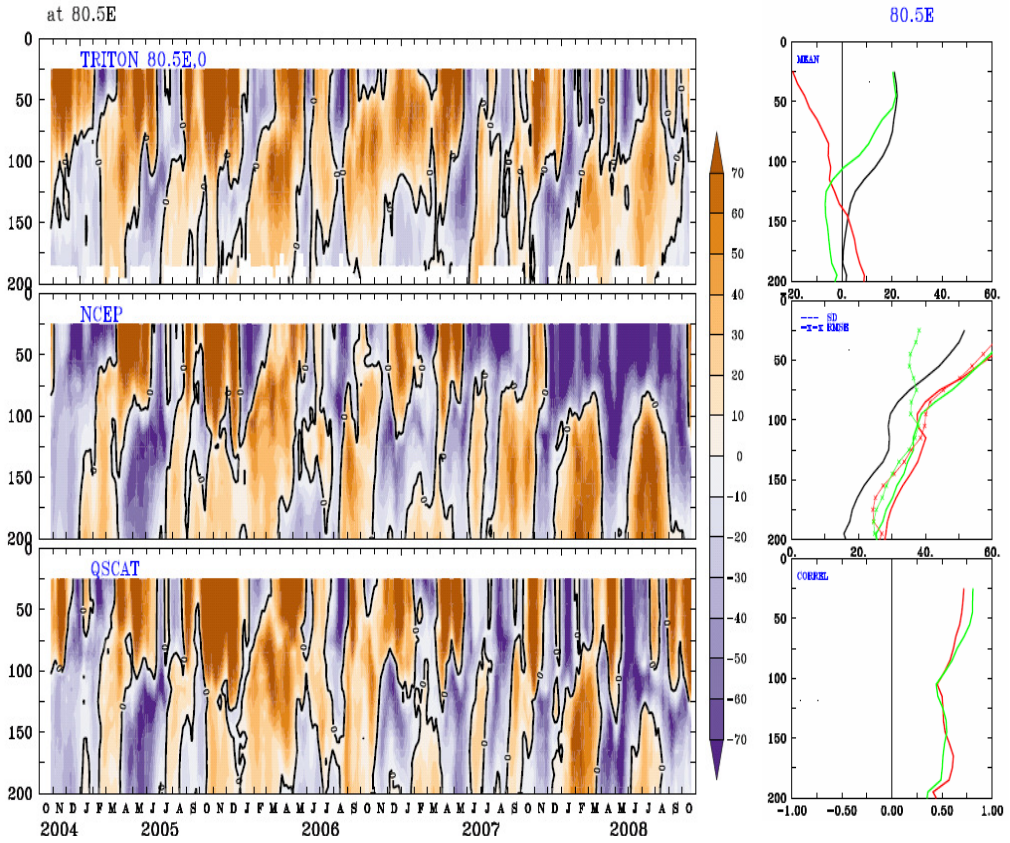

Figure 5.5.11.b. Same as Figure 5.5.11.a, but for Equator and 80.5°E.

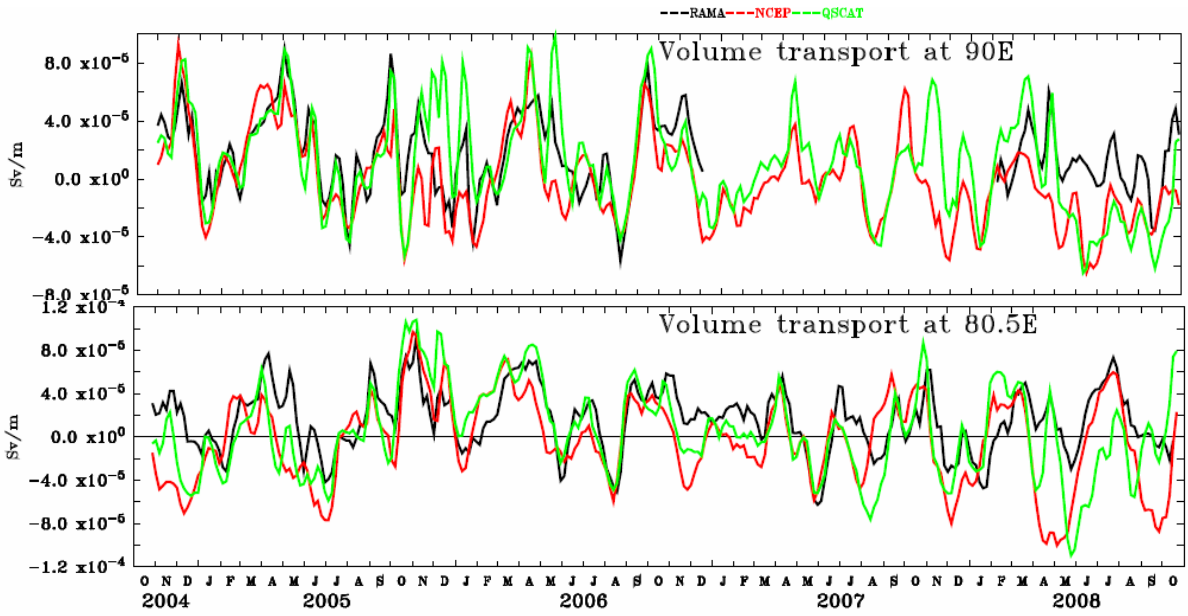

Figure 5.5.12. Volume transport (sv m^{-1}) comparisons of NCEPEXP and QSCATEXP with ADCP buoy locations at 90ºE, and 80.5ºE along equator.

Vertical profiles of the model currents are compared with ADCP observations from RAMA buoys at 90˚E and 80.5˚E on the equator. Figure 5.5.11 shows the zonal current profiles and their statistics for the model and the observations. An eastward flowing undercurrent is present in the equatorial region of the IO. This Equatorial Under Current (EUC) is better developed during the winter monsoon on the eastern side of the Ocean than on the western side [*Knauss and Taft,* 1964]. The presence of the EUC during the northeasterly and southwesterly monsoon is reported by *Reppin et al.* [1999] for the year 1994. A recent study by *Iskandar et al.* [2009], using the ADCP mooring at 0˚S, 90˚E reported evidence for the presence of the EUC between 90 m and 170 m during both monsoon seasons. The strong seasonality observed in the EUC by *Ishkander et al.* [2009] at 0˚, 90˚E is reproduced by the model simulations up through 2007. However, during 2008 and 2009, NCEPEXP fails to capture the undercurrent, while QSCATEXP simulates the EUC better. We speculate that the absence of the EUC in the NCEPEXP is due to the erroneous NCEP surface winds as discussed in the section 5.5.1. At 80.5˚E as well, QSCATEXP simulates the current pattern better than NCEPEXP. A statistical analysis done on the two simulations revealed that QSCATEXP currents are well correlated with observations and have smaller errors than those in NCEPEXP.

Volume transport estimates provide another way of validating the current profiles. Volume transport estimates using equation 2 at 80.5˚E and 90˚E on the equator using ADCP current measurements are compared to the model estimates (Figure 5.5.12). Volume transport estimates in both model simulations are in good agreement with observations.

Using an Ocean General Circulation Model, *Sengupta et al.* [2004] established that a biweekly mode of meridional currents on the the equator consists of packets of westward propagating wind forced Mixed Rossby Gravity (MRG) waves. They proposed that the atmospheric Quasi Biweekly Mode resonantly forces biweekly MRG waves in the ocean and so are responsible for the biweekly oscillations observed in the meridional currents in the

eastern equatorial region. The amplitude spectra of the meridional currents in both the model simulations and the observations at 80.5ºE and 90ºE show the biweekly oscillations (Figure 5.5.13). At 80.5˚E, QSCATEXP simulates biweekly modes at 12, 15 and 17 days in agreement with the observations, NCEPEXP also simulates the modes but with lesser accuracy. Similarly, at 90ºE, the biweekly oscillations simulated by QSCATEXP are also reasonably comparable with the observations but with a smaller amplitude.

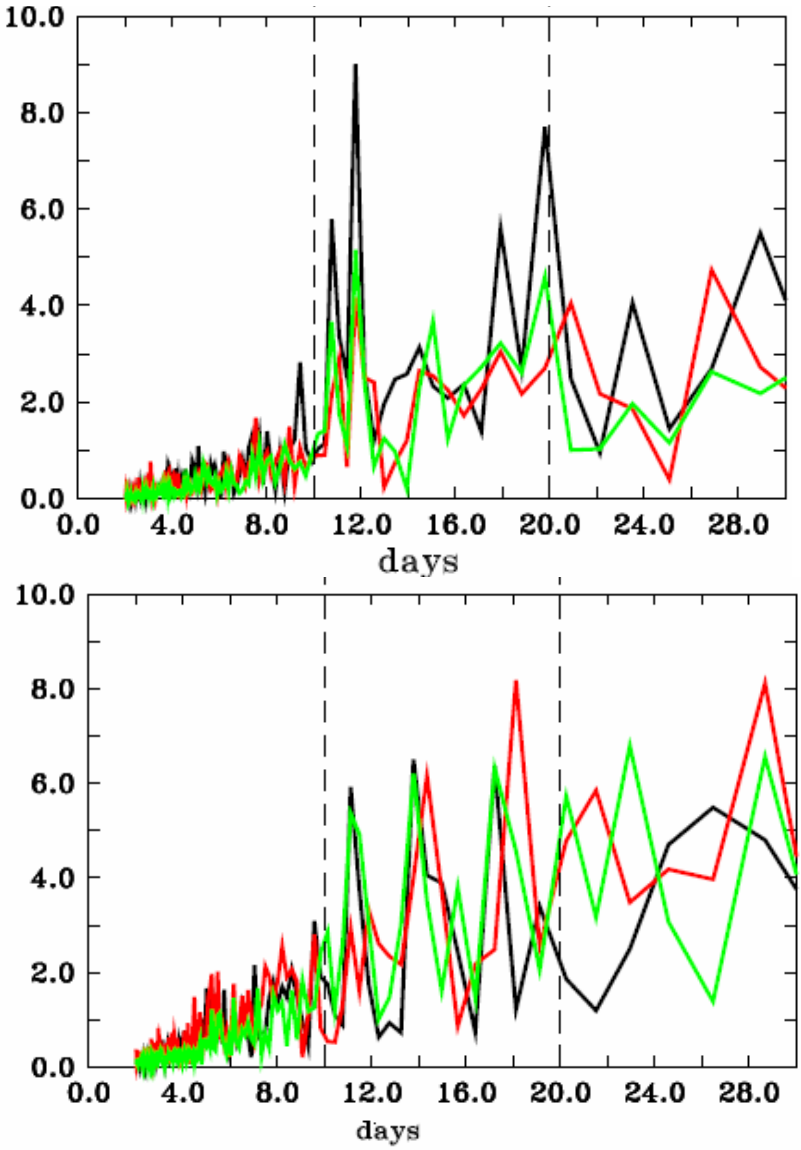

Figure 5.5.13. The FFT amplitude (cm s^{-1}) spectrum of meridional currents from NCEPEXP (red), QSACTEXP (green) and ADCP profiles (black) from RAMA mooring at 90˚E (top) and 80.5˚E (bottom) along the equator shows the biweekly oscillations.

5.6 Mixed Layer Depth and Isothermal Layer Depth

5.6.1 Mean monthly evolution

The ability of the model to reproduce the climatological monthly evolution of the MLD is evaluated using WOA09. The monthly evolution of the MLD in the two model runs and in the WOA09 climatology and the differences between them are shown in Figure 5.6.1. The spatial evolution of the observed MLD variability is accurately reproduced by both model runs. There is no notable difference in the MLD between these two model runs and the difference between the models and the observations is relatively small (model-WOA09; -5 to 15 m), except in some localized areas. The model generally has a deeper mixed layer compared to the observations. Large differences between the model and the observations are seen at some localities such as the southeastern Arabian Sea and the head-bay during the months of January and February (Figure 5.6.1). It is well known that during winter monsoon season, the MLD in the southeastern Arabian Sea is primarily controlled by a strong halocline in the near surface layer caused by the advection of low saline water from the Bay of Bengal by the EICC [*Rao and Sivakumar,* 2003]. Figure 5.3.2 shows the salinity difference between the model and WOA09. The region where there is a large difference in the MLD coincides exactly with the region where the surface salinity difference is large. The surface salinity in the model overestimates the observed value by more than 1 psu in the southeastern Arabian Sea during January and February. The near-surface stratification is not controlled by salinity in the model. To investigate further, the subsurface salinity and temperature has also been compared at two locations; one where the discrepancy exists (a box of 2ºN-6ºN; 72ºE-76ºE) and another where there is no discrepancy (a box of Equator-4ºN; 56ºE-60ºE). The results are shown in Figure 5.6.2.a and 5.6.2.b. It is clear from Figure 5.3.2 that, during January and February, in the south eastern Arabian Sea, the strong halocline, which is seen in the observations, is not reproduced in the model. Hence, the near surface stratification is not controlled by salinity in the model (Figure 5.6.2.a). Temperature also shows a small

difference with the observations (Figure 5.6.2.b). The weaker stratification in the model salinity compared to that observed translates into a weaker stratification in density and a larger MLD. Elsewhere, in regions where the model and observed MLD do not differ, the vertical structures of salinity and temperature also do not differ. Except this kind of discrepancy in some localized areas, the model does a good job in reproducing the observed MLD. The model grid has been prepared in such a way that there is a wide opening for the Palk Strait. This study suggests that, the salinity and MLD errors in the eastern Arabian Sea could be rectified by closing the Palk Strait in the model grid. In the Head Bay, the overestimation of the model MLD begins in July and reaches maximum in January-February. This temporal evolution of the MLD difference (model-observation) coincides with that of the salinity difference (Figure 5.3.2). This analysis also implies the importance of seasonal variability in the river discharge supplied to the model.

Figure 5.6.3 shows the standard deviation of the MLD and the annual average of the MLD for both the observations and the model runs. The model runs show similar spatial patterns and magnitudes of the MLD. Although the model overestimates the standard deviation, the model does well in reproducing the spatial patterns in the observations.

Figure 5.6.4 shows the bias (model-observations), the correlation between the model and observations and the RMSE of the model compared to observations. A bias of about 5 m is typical throughout the entire IO with the exception of some localized regions such as the head-bay, the eastern equatorial IO and the southeastern IO. As has been shown, these are regions where the salinity simulation is poor. The correlation with observations is also poor in these regions and in the eastern Arabian Sea as well. However, other regions show very good correlations of greater than 0.8. The RMSE shows a spatial pattern, which coincides with the bias, as expected.

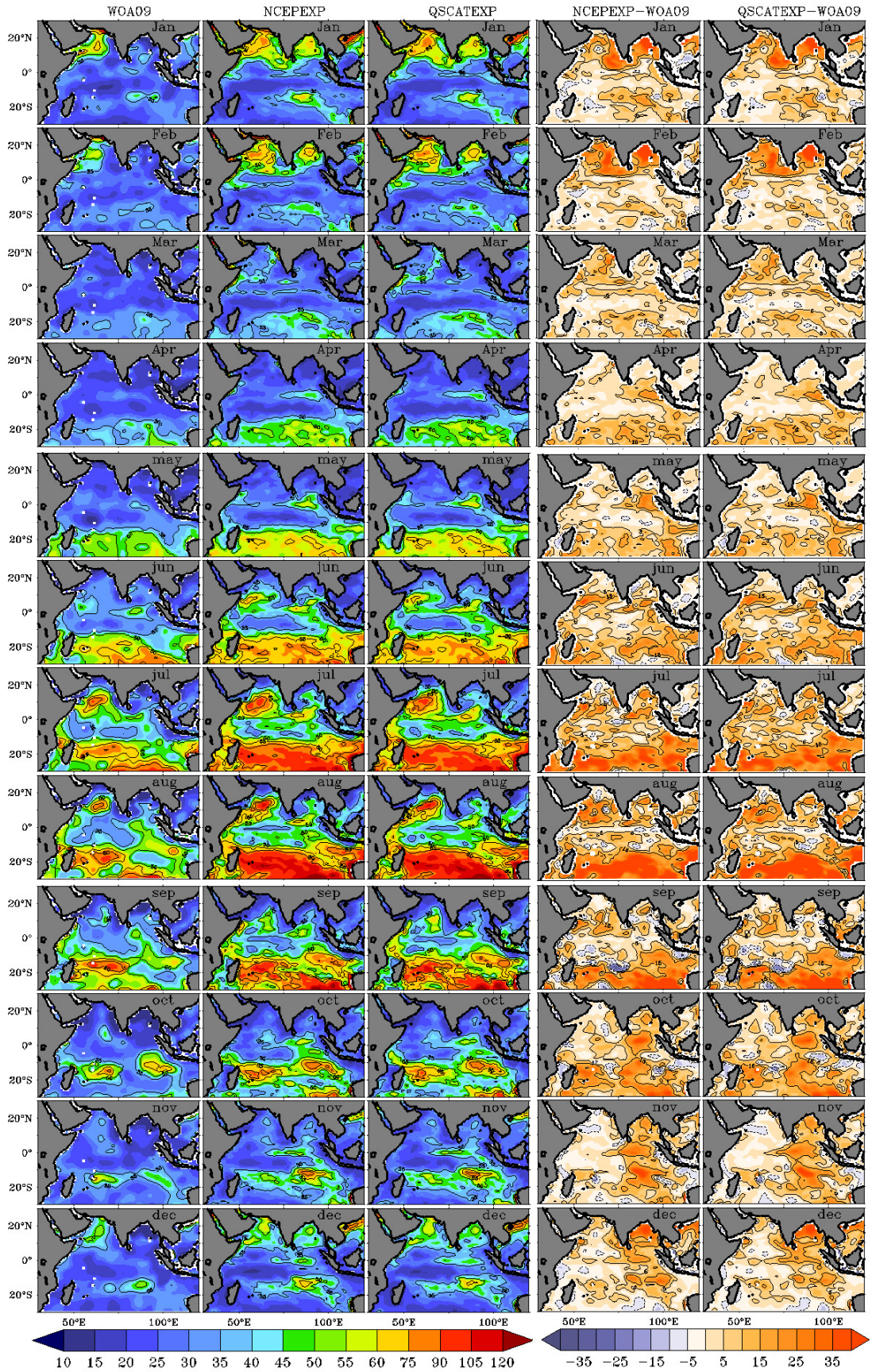

Figure 5.6.1. The monthly evolution of multiyear average (2004-2009) of MLD (m) derived from 2 model runs and WOA09 climatology and the difference in MLD obtained from model and observation.

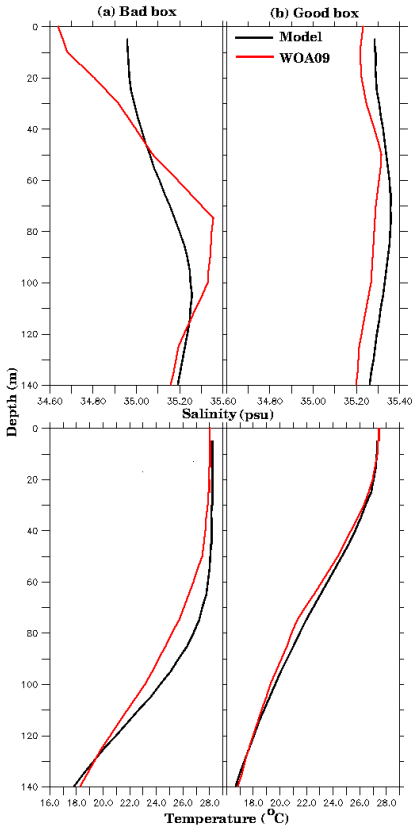

Figure 5.6.2. The difference between model and observation (WOA09) in the vertical profiles of salinity (psu) (January (Top) and February averaged) at a location where MLD (m) discrepancy is there (left panel) and where MLD discrepancy is not there (right panel). Difference between model and observation in the vertical profiles of temperature (ºC) (January and February averaged) (Bottom) at a location where MLD discrepancy is there (left panel) and where MLD discrepancy is not there (right panel).

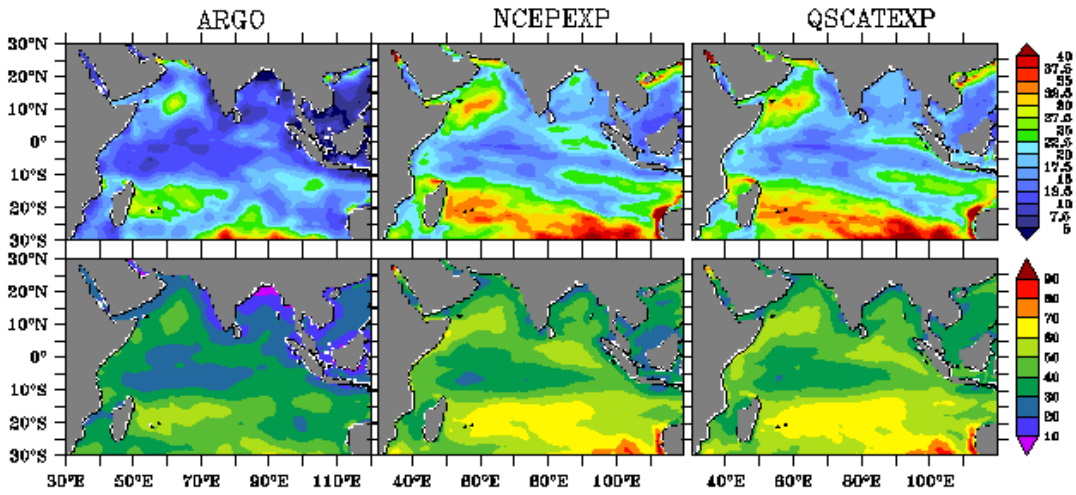

Figure 5.6.3. The standard deviation (top panel) in the MLD (m) and the average MLD (bottom panel) in the observation as well as in model runs.

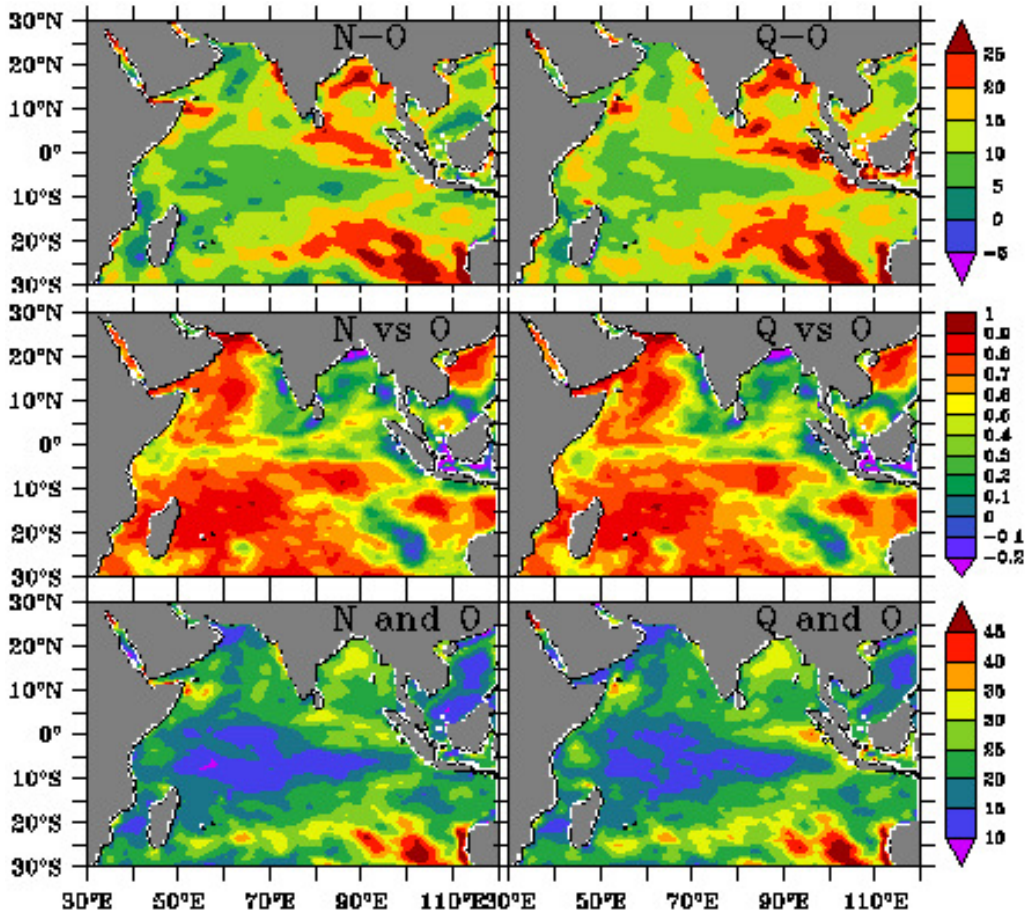

Figure 5.6.4. Bias (model-observation) (top panel) in MLD (m), correlation between the model MLD and observation (middle panel) and root mean square error in the model MLD compared to observation (bottom panel).

5.6.2 Intra-seasonal and inter-annual variability in MLD

5.6.2.1 At selected regions (using 5-day model output) using Argo gridded product

Figure 5.6.5 shows the time series of the MLD at 8 selected regions in the IO basin. The mean, the standard deviation, the correlation between the model and the observations, and the RMSE in the model with respect to the observations at each location are shown in Table 5.6.1. These statistical parameters are graphically represented using a Taylor diagram (Figure 5.6.6). The plots along with these statistical parameters clearly show that the model does a reasonably good job in capturing intra-seasonal as well as inter-annual variability in the MLD. CBOB shows a notable disagreement between the model and the observations

during the December-February period (the model MLD is too deep) in all the years. This may be due to the use of an average annual river-discharge into the model instead of monthly values. Both the model simulations show a similar performance as revealed in the Taylor diagram. A very good correlation of more than 0.8 is observed in the ITF, SEC, SEYC, CAS and SOM regions. The LAK and CBOB show correlations as poor as 0.3 and the WYRT shows a value of 0.6. The poor correlations in LAK and CBOB might be associated with the salinity problem discussed previously.

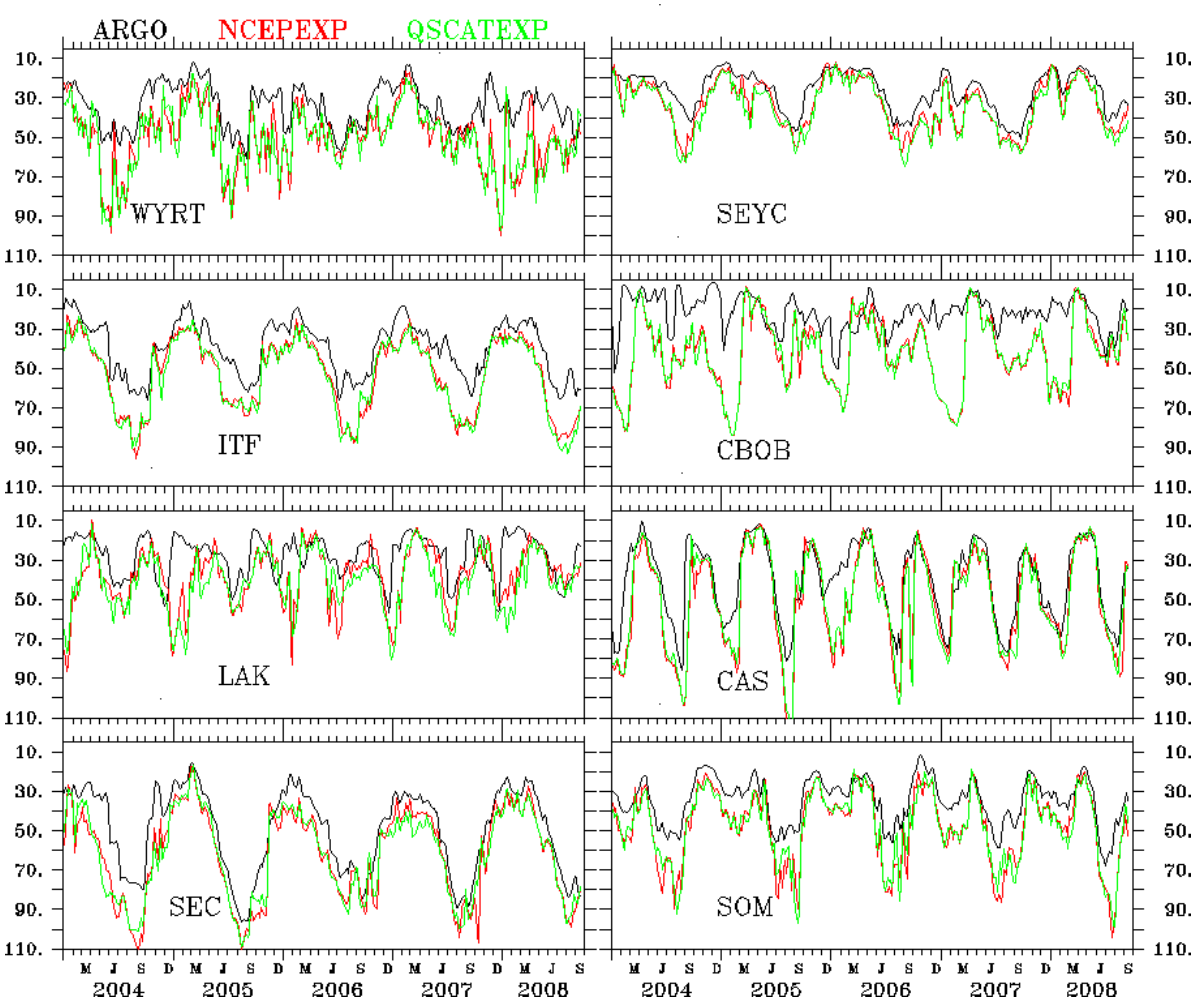

Figure 5.6.5. The time series of MLD (m) averaged over 8 selected regions (as indicated in the legend) in the IO basin.

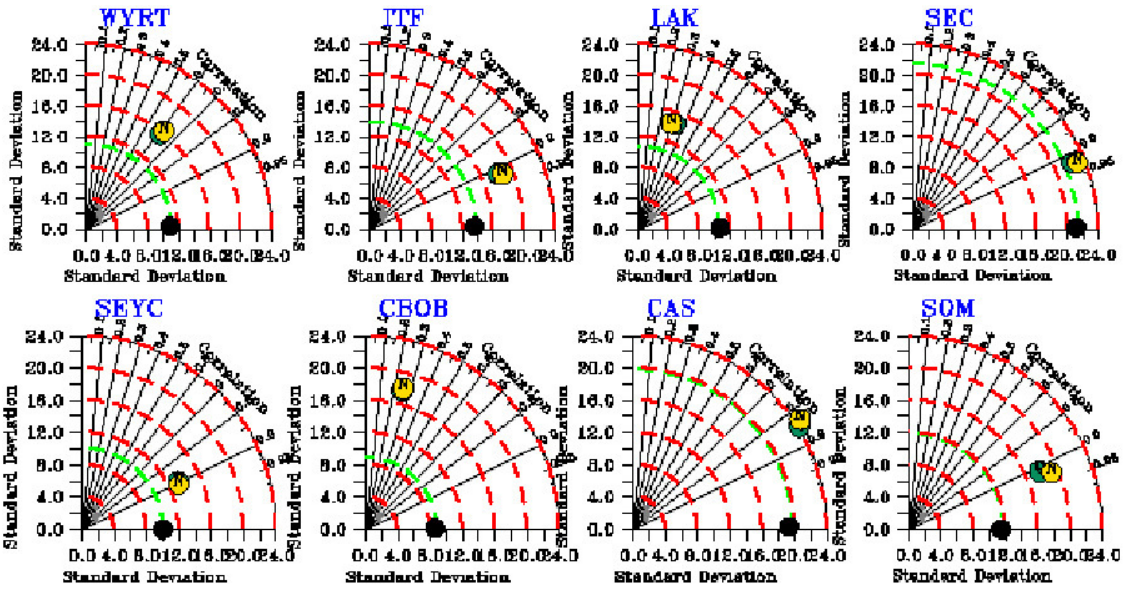

Figure 5.6.6. Taylor diagram showing the MLD (m) performance of two model-runs in comparison with observation averaged over 8 selected regions in the IO (as indicated in the legend).

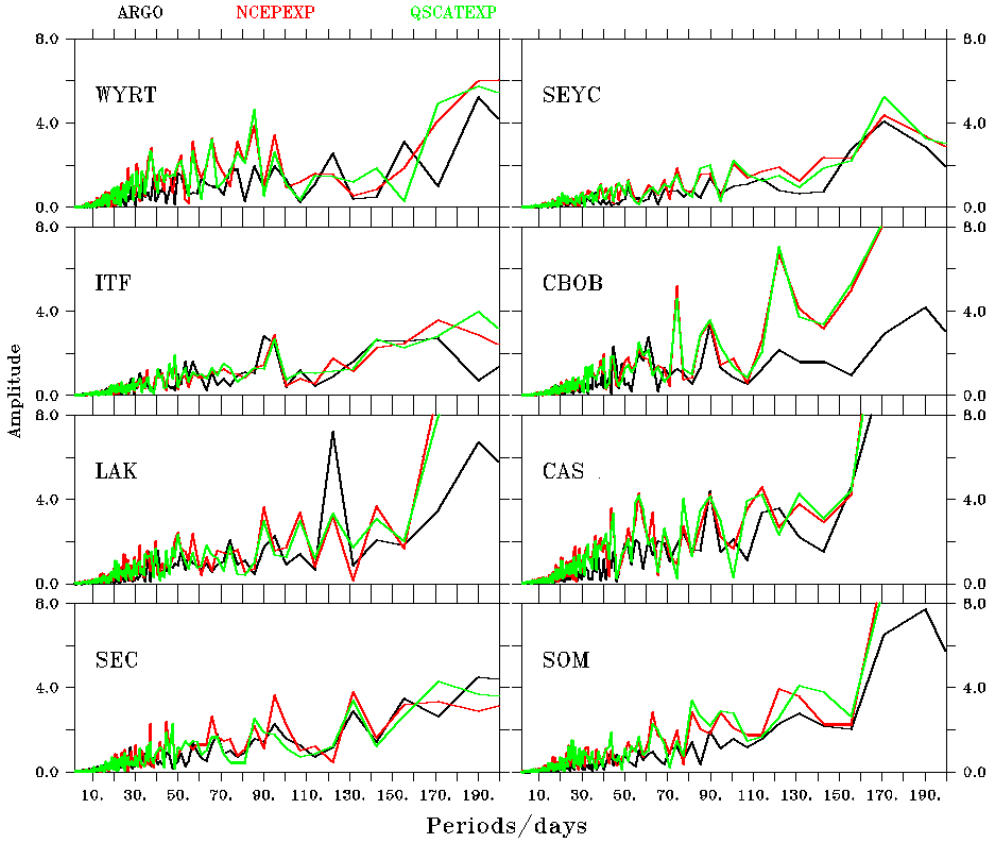

Figure 5.6.7. The FFT amplitude spectrum of MLD (m) at selected locations in the IO basin.

Table 5.6.1. Statistical parameters for the comparison of MLD (m) derived from the model with that derived from optimally interpolated Argo gridded data.

	MEAN			STD			RMSE		Correlation	
Location	Argo	NCEP EXP	QSCAT EXP	Argo	NCEP EXP	QSCAT EXP	Argo & NCEP EXP	Argo & QSCAT EXP	Argo & NCEP EXP	Argo & QSCAT EXP
WYRT	34.27	50.63	51.87	11.03	16.21	15.61	20.81	21.77	0.61	0.61
ITF	39.76	52.80	54.16	13.87	18.6	18.08	15.51	16.57	0.92	0.91
LAK	28.08	38.34	40.68	10.71	14.45	14.48	18.45	19.76	0.30	0.34
SEC	49.98	61.26	62.39	21.39	23.01	22.27	15.03	14.95	0.92	0.92
SEYC	26.40	32.56	35.44	10.05	13.17	13.26	8.192	10.82	0.90	0.89
CBOB	21.76	42.08	42.51	8.869	18.09	17.79	27.49	27.39	0.25	0.25
CAS	40.80	48.89	50.06	19.76	24.74	24.21	17.38	16.46	0.83	0.85
SOM	34.74	47.30	46.89	11.84	19.03	17.76	15.87	15.56	0.92	0.91

Figure 5.6.7 shows the amplitude spectra of MLD at the 8 selected locations. It is clearly seen from the figure that most of the intra-seasonal and inter-annual variabilities have been captured by the model. Generally, the variabilities are captured very realistically by the model. The 90-day periodicity has been captured very well at all the locations. The disagreement at CBOB is also reflected in its spectrum, especially at longer periods. At LAK, although the 120 day periodicity has been picked up by the model runs, the amplitude is only about half that of the observations.

5.6.2.1 At RAMA buoy locations (using daily model output)

Figure 5.6.8 shows the time series of the MLDs derived from all 14 available RAMA buoys in the IO along with those from the model runs. For these comparisons, we have used the daily output from the model for the years 2008 and 2009. Table 5.6.2 gives the statistical parameters for the comparison of model and RAMA MLDs. In the northern IO the

correlations average about 0.5, while in the Southern IO the correlations are about 0.6. Along the equator, in the central IO, the correlations are 0.5, while in the eastern IO, it drops to 0.24. Figure 5.6.8, in conjunction with Table 5.6.2, shows that the MLD has been replicated by the model reasonably well. During January and February of both the years, in the head-bay, the model shows a deeper MLD compared to the observations. This discrepancy decreases as it goes towards equator. The reason for this discrepancy, once again, is inadequacy of using an annual average river outflow in the model and it further emphasizes the importance of prescribing a seasonally varying climatology. Assimilation of observed salinities would have improved the salinity structure and hence MLD. At 8°S, 55°E, where the Seychelles-Chagos thermocline ridge exists, a temporally constant MLD is observed with an average value of 15 m from November 2008 to May 2009, after that it deepens very consistently in the RAMA data as well as in the model. The same behaviour occurs at a location 4°s further south, but here the model and observed MLDs differ by nearly 5 m.

Figure 5.6.9 shows the time series of the ILD derived from all the available RAMA buoys from the IO along with the model derived ILD. The statistical parameters for this comparison are shown in Table 5.6.3. It is very clear from the figure and table that the ILD is reproduced by the model very realistically except at 12°S, 67°E (here, the correlation is only 0.21). Although the model does not capture the observed variability resulting in a very poor correlation, the model and observed magnitudes are comparable at this location.

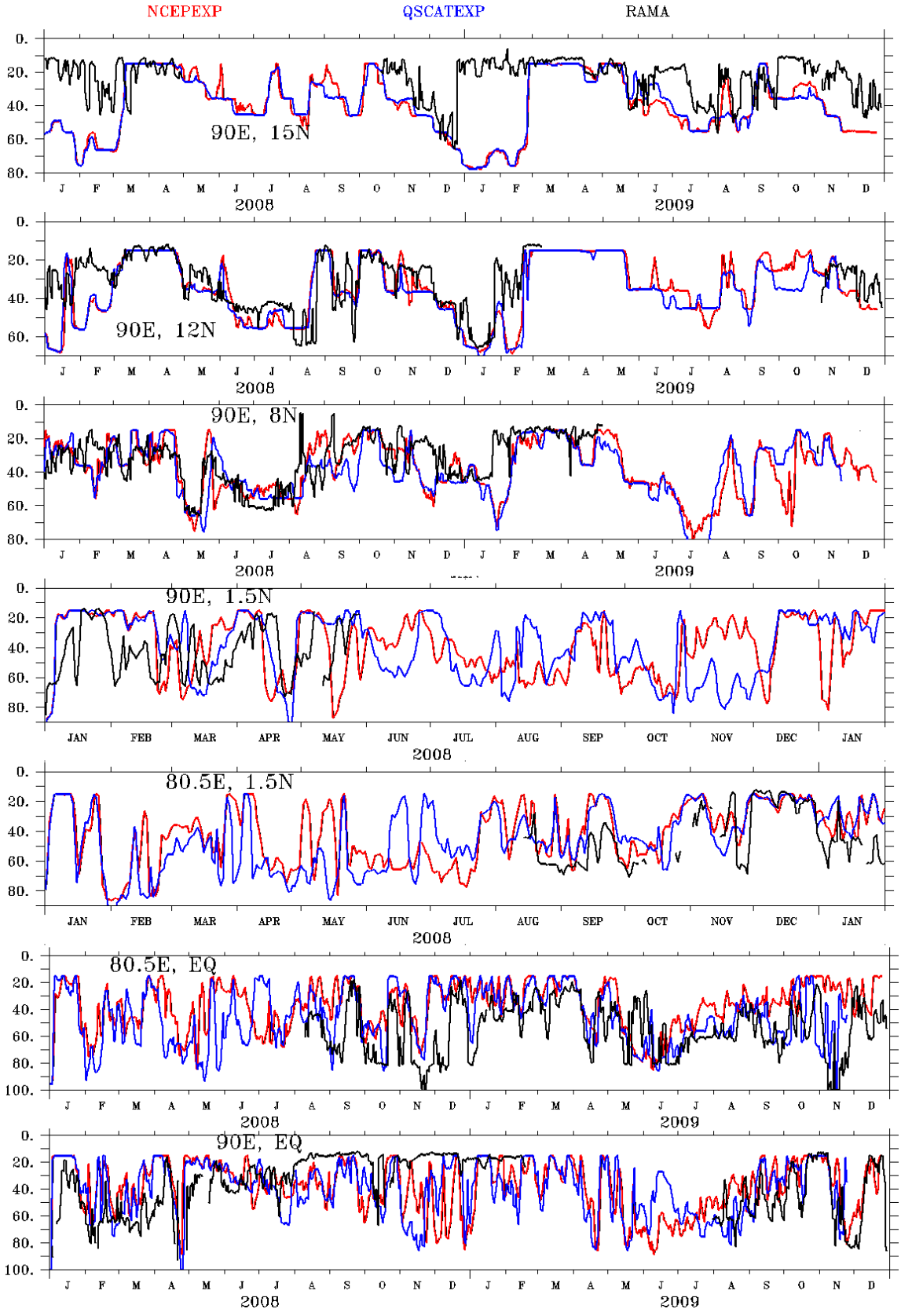

Figure 5.6.8. Time series of MLD (m) derived from all the available RAMA buoys from IO along with model derived MLD.

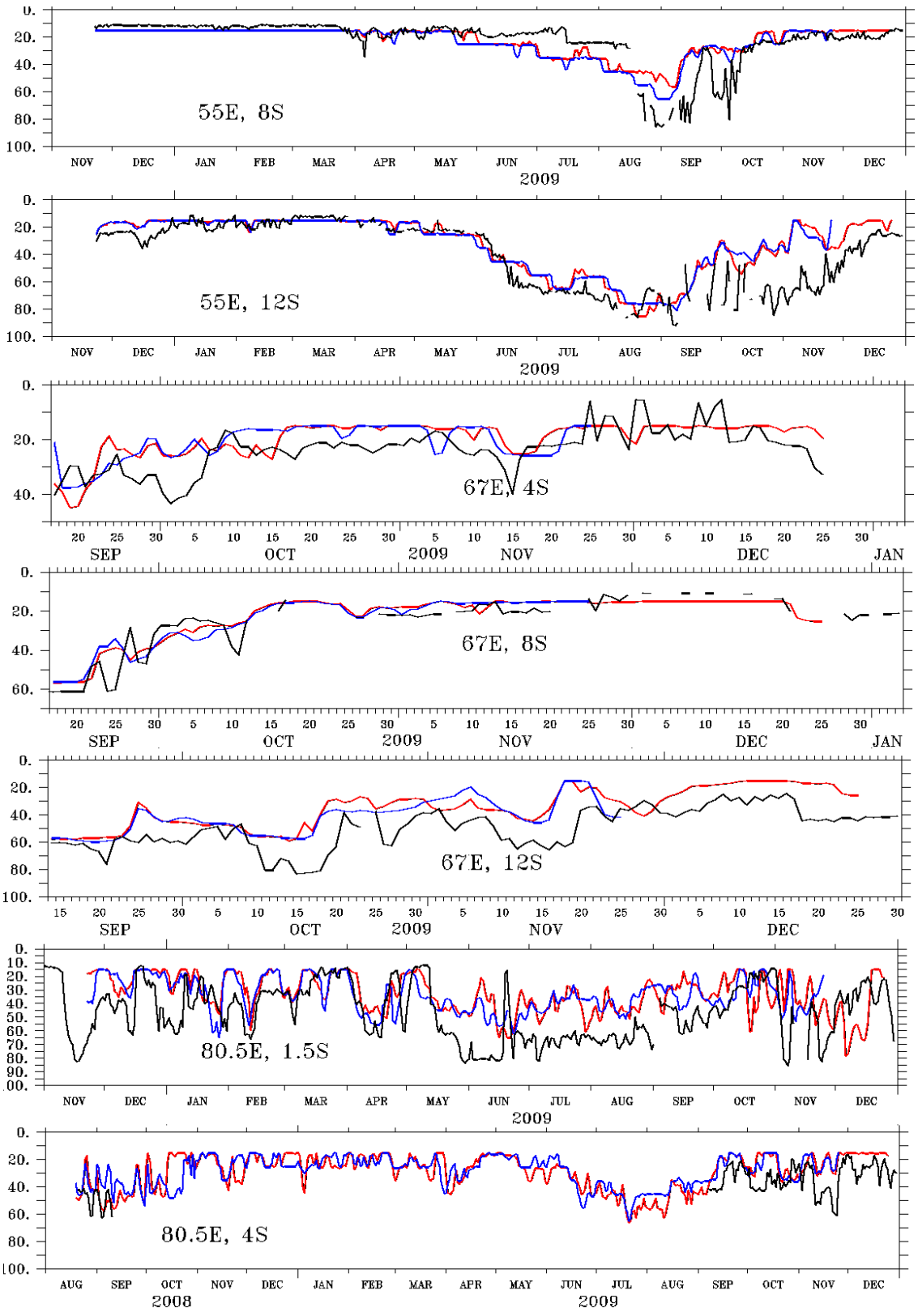

Figure 5.6.8. (Continue) Time series of MLD (m) derived from all the available RAMA buoys from IO along with model derived MLD.

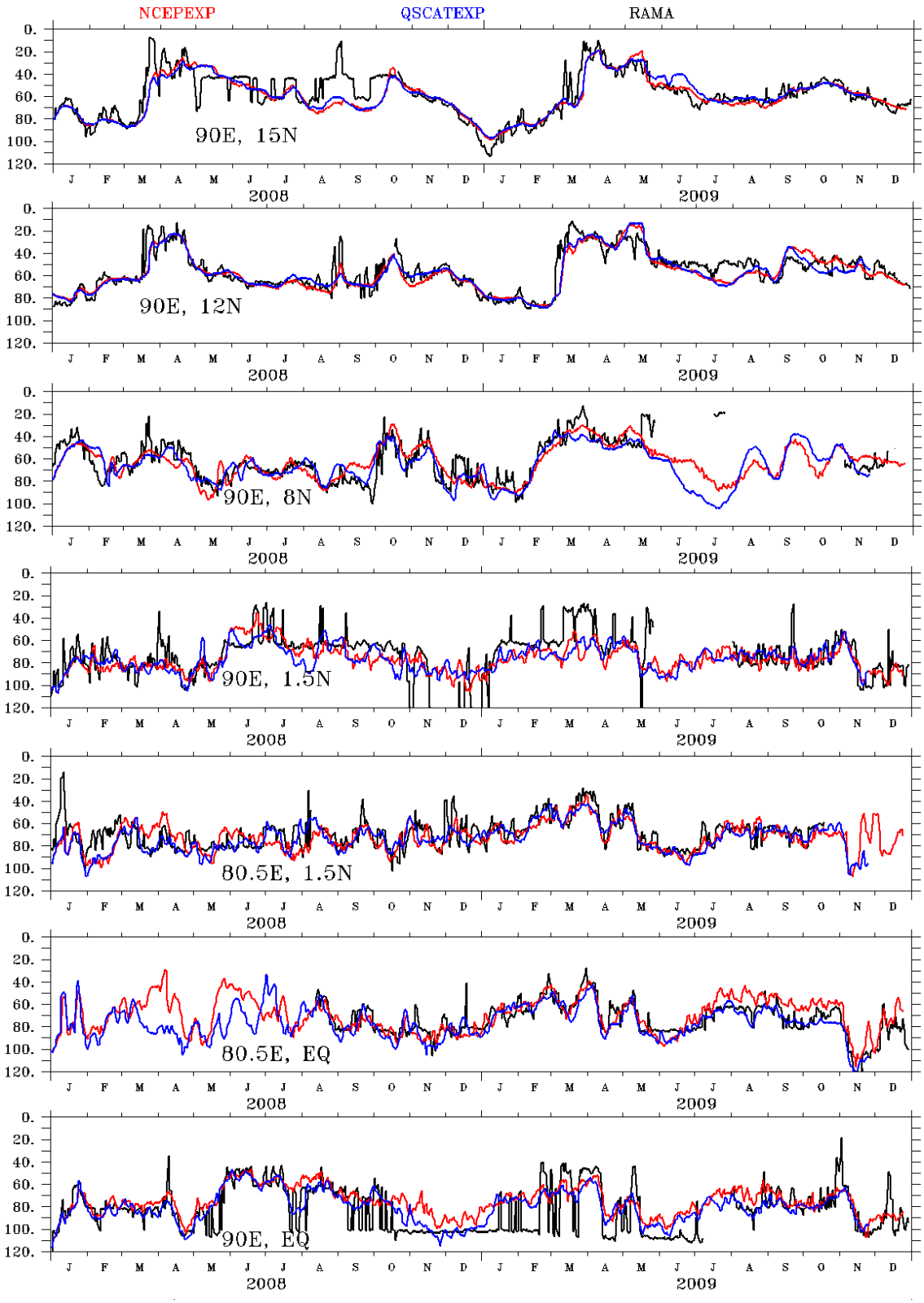

Figure 5.6.9. Time series of ILD (m) derived from all the available RAMA buoys from IO along with model derived ILD.

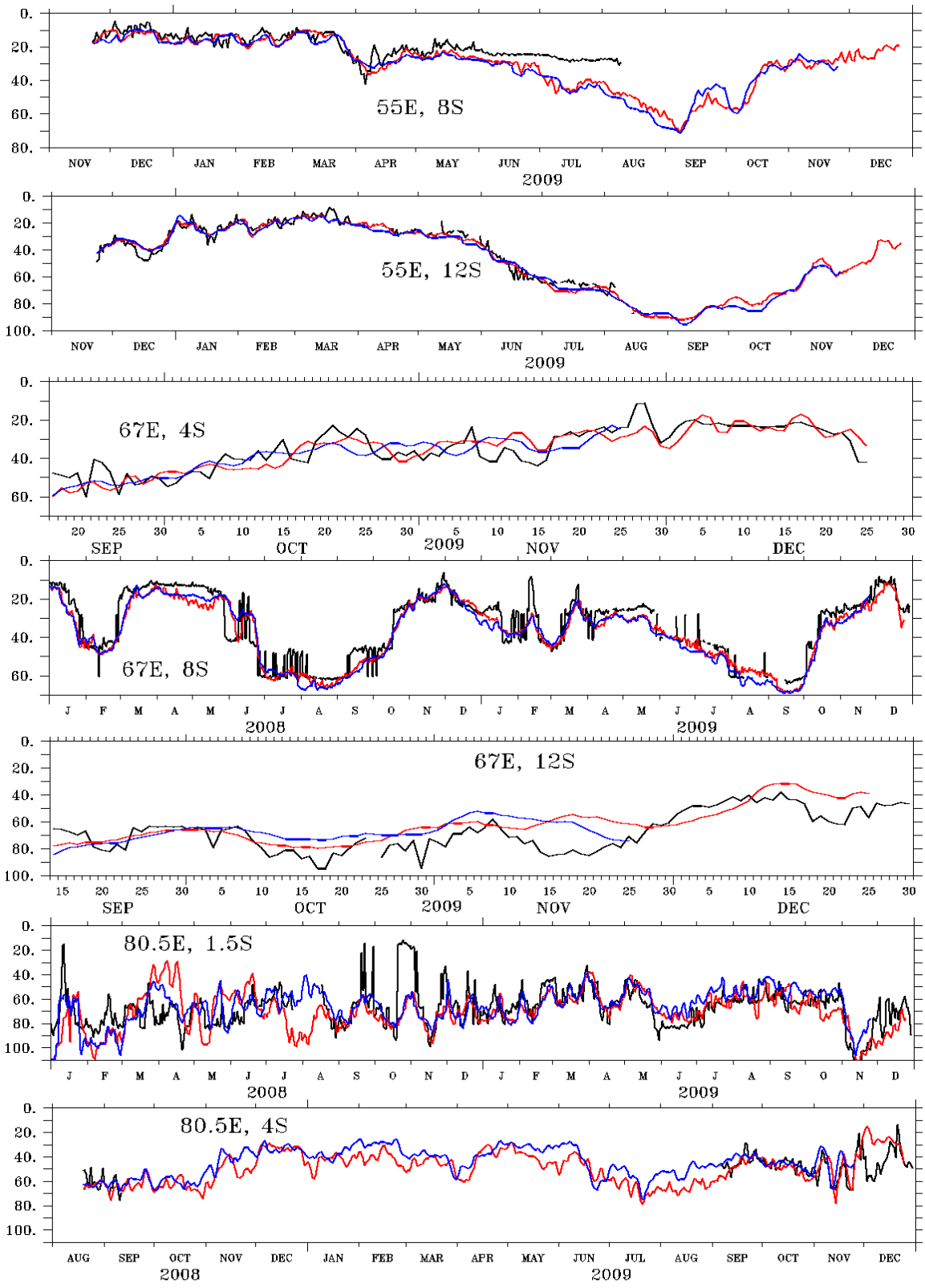

Figure 5.6.9. (continue) Time series of ILD (m) derived from all the available RAMA buoys from IO along with model derived ILD.

Table 5.6.2. Statistical parameters for the comparison of MLD (m) derived from the model with that derived from RAMA data.

Location	MEAN			STD			RMSE		Correlation	
	RAMA	NCEP EXP	QUIK EXP	RAMA	NCEP EXP	QUIK EXP	RAMA & NCEP EXP	RAMA & QUIK EXP	RAMA & NCEP EXP	RAMA & QUIK EXP
1.5°S, 80.5°E	45.21	6.26	37.31	21.18	17.10	16.30	23.83	22.91	0.37	0.45
15°N, 90°E	23.51	39.82	39.26	11.81	18.17	17.80	27.10	27.19	0.63	0.57
12°N, 90°E	32.56	34.49	35.97	14.17	16.09	15.83	14.22	14.43	0.65	0.67
8°N, 90°E	32.15	37.84	39.04	14.47	15.96	16.56	14.04	15.00	0.56	0.53
1.5°N, 90°E	41.75	41.55	40.49	19.49	21.00	20.97	23.83	21.67	0.36	0.42
EQ, 80.5°E	54.89	37.20	45.50	19.73	17.67	21.19	28.85	23.43	0.36	0.49
EQ, 90°E	35.77	38.62	40.17	20.89	19.74	20.06	24.49	23.92	0.16	0.24
8S, 55°E	22.26	22.22	24.41	16.47	10.44	12.77	11.89	11.65	0.70	0.74
12°S, 55°E	40.57	32.77	33.65	24.21	20.81	20.39	15.96	16.12	0.83	0.84
4°S, 67°E	23.65	19.63	21.11	7.981	6.477	6.475	7.85	8.330	0.58	0.53
8°S, 67°E	30.45	27.21	28.65	16.35	14.23	14.81	8.34	8.407	0.87	0.86
12°S, 67°E	49.89	35.14	41.84	14.60	13.83	12.27	18.57	18.44	0.71	0.59
1.5°S, 80.5°E	45.21	36.26	37.31	21.18	17.10	16.30	23.83	22.91	0.37	0.45
80.5°E, 4°S	35.85	29.20	29.05	11.18	13.02	10.97	14.84	15.78	0.58	0.43

Table 5.6.3. Statistical parameters for the comparison of ILD (m) derived from the model with that derived from RAMA data.

Location	MEAN			STD			RMSE		Correlation	
	RAMA	NCEP EXP	QUIK EXP	RAMA	NCEP EXP	QUIK EXP	RAMA & NCEP EXP	RAMA & QUIK EXP	RAMA & NCEP EXP	RAMA & QUIK EXP
1.5°S 80.5°E	57.93	61.21	59.67	20.95	17.08	17.17	11.25	11.15	0.83	0.83
15°N, 90°E	56.97	57.64	57.57	19.29	17.94	16.46	9.376	8.58	0.86	0.87
12°N, 90°E	63.92	63.71	65.64	18.52	15.56	16.05	14.40	15.69	0.67	0.61
8°N, 90°E	72.68	77.01	76.74	24.54	11.78	11.34	16.91	17.19	0.63	0.61
1.5°N, 90°E	64.60	73.02	73.23	16.36	11.80	12.42	12.03	10.61	0.57	0.69
EQ, 80.5°E,	66.26	68.98	76.47	20.84	16.18	14.38	9.978	8.25	0.80	0.87
EQ, 90°E	74.46	74.96	80.40	26.96	12.79	13.92	16.25	13.91	0.71	0.73
8°S, 55°E	22.11	29.92	31.12	8.529	15.36	15.50	7.26	8.30	0.85	0.84
12°S, 55°E	35.84	47.99	48.35	18.65	25.35	25.23	3.84	4.04	0.98	0.97
4°S, 67°E	34.68	37.94	39.43	10.78	10.28	8.744	6.746	6.37	0.77	0.75
8°S, 67°E	36.02	38.24	38.51	16.49	15.36	16.29	6.727	6.76	0.93	0.93
12°S, 67°E	53.06	68.09	67.75	23.22	7.456	7.182	12.56	12.6	0.22	0.21
1.5°S, 80.5°E	61.80	69.24	65.60	19.05	15.22	13.83	16.11	14.2	0.48	0.57
4°S, 80.5°E	40.37	51.74	44.83	18.62	11.68	11.54	7.522	7.62	0.72	0.72

6. Website for ocean analysis products

The main objective of the GODAS-MOM at INCOIS is to provide an accurate estimate of the ocean state, which could be used to initialize a coupled model for the seasonal monsoon prediction and also to understand the variability of the ocean at different time scales.

In this regard, the temperature, salinity, sea surface height and velocity structure of the global ocean since January 2003, which were simulated by GODAS-MOM, when it is forced with QuikSCAT and NCEP2 winds, are being made available for oceanographic research and other operational activities. Interested users can access these data sets through the Live Access Server (LAS) using the link http://las.incois.gov.in/las/getUI.do. The data sets are available under the subdirectory "ocean analysis" in "choose data set". The LAS makes it relatively easy to create basic graphics and to download subsets of the data. We also offer OPeNDAP, formerly known as DODS (Distributed Oceanographic Data Server). At present, only monthly and pentad data sets are available through our website. The datasets are available at present in NetCDF, ASCII and arcGrid format. The data products at daily resolution will be made available in the web shortly. The derived products such as the ILD, the MLD, the depth of the 20°C isotherm and the steric height anomaly are made available through LAS. The Figure 6.1.a and Figure 6.1.b shows a screen shot, which gives an overview of the visualization capabilities of GODAS-MOM at INCOIS.

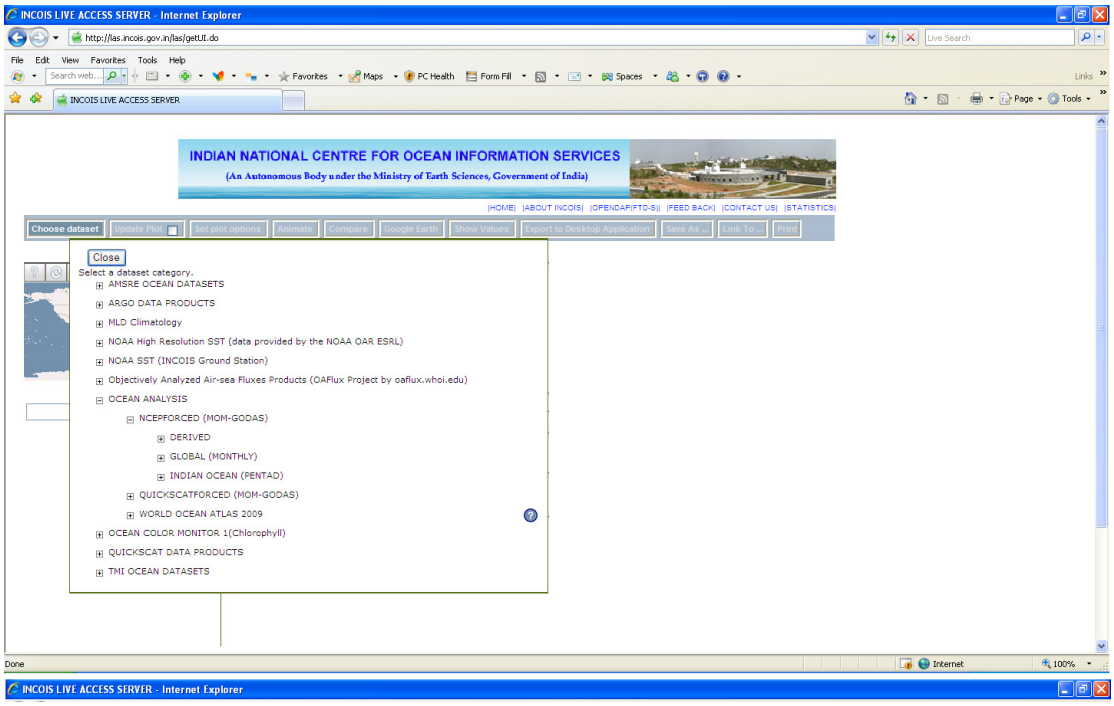

Figure 6.1.a. INCOIS webpage from where MOM-GODAS ocean analysis product can be downloaded.

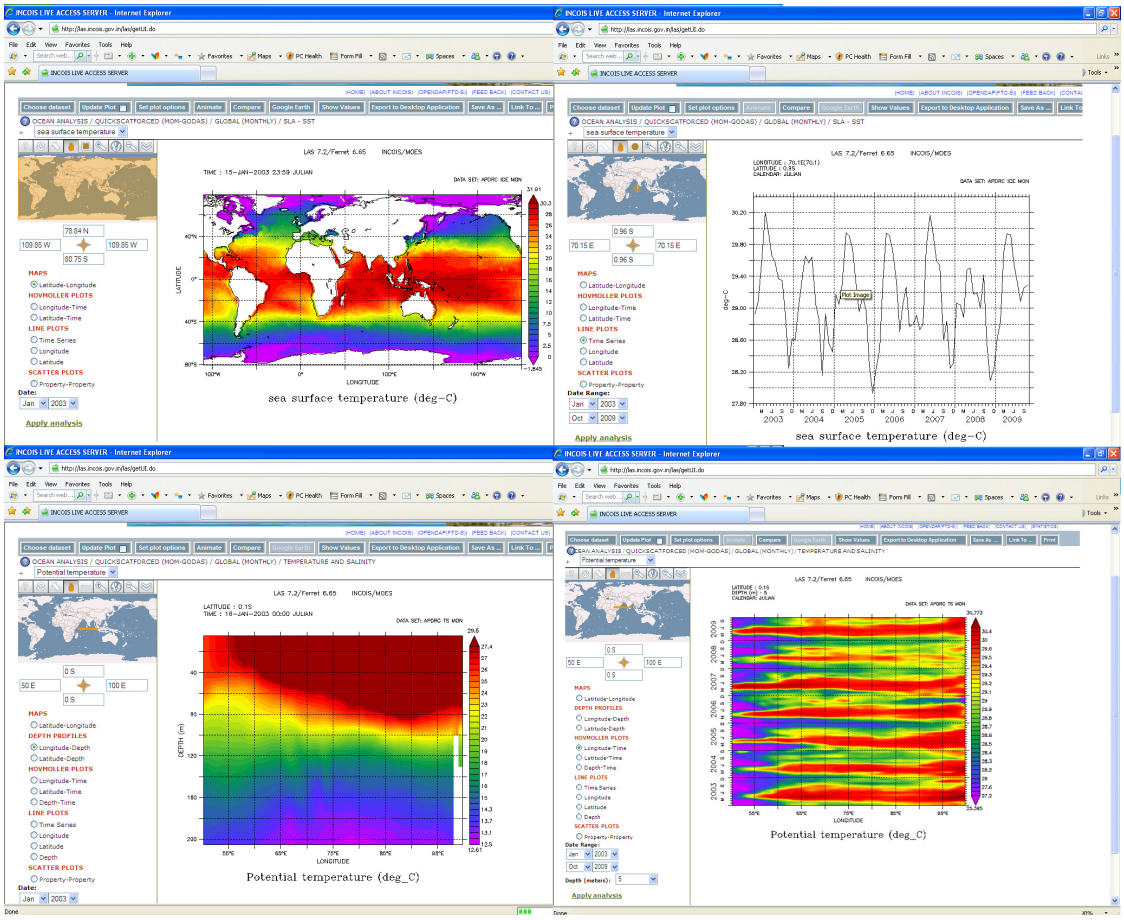

Figure 6.1.b. Examples of GODAS-MOM LAS visualization capabilities.

7. Summary and Conclusion

A new version of the GODAS, which is based on the GFDL MOM4p0 and a 3DVAR data assimilation scheme, is configured at INCOIS. In this report, we present the validation of the GODAS-MOM ocean state in the Tropical IO. Two cases are examined, forced with two different wind products: the NCEP/NCAR reanalysis momentum fluxes and the QuikSCAT scatterometer winds. The validation reveals that, in both experiments, the model simulates most of the observed features of SST, D20, SSHA, vertical temperature structures, MLD, ILD and currents with reasonably good accuracy in the Tropical IO at both seasonal and interannual time scales. The analysis further shows that there was a considerable improvement in the ocean current field when the model was forced with the QuikSCAT winds. The validation also suggests the need for further improvement to the GODAS-MOM. A brief list of recommendations for the improvement of the model is described below.

1) The analysis showed that forcing the model with an annual river discharge leads to large errors in the salinity field in the Bay of Bengal. The wrong representation of the salinity stratification in the head bay, causes a poor representation of the model mixed layer, and it may eventually leads to an error in the mixed layer heat budget in the near surface layer. The consequences are errors in the SST and the MLD in the Bay of Bengal, especially in the head bay. Hence it is recommended that a seasonally varying freshwater river discharge be used instead of an annual average.

2) *Momin et al.* [2010] studied the impact of satellite-derived precipitation on the variability of the sea surface salinity in the tropical IO using an OGCM. Their analysis suggests that the forcing with satellite precipitation (GPCP) captures the high-frequency variability much better than that forced by precipitation from the NCEP reanalysis. They further suggested that the regions of high-frequency variability in sea surface salinity coincide with the regions of high-frequency variability in the satellite precipitation. Their study further emphasizes that the low-frequency part of the sea surface salinity variability is governed by advective processes and that satellite derived precipitation does not have a significant impact on this scale of variability. The GODAS-MOM is forced with NCEP2 precipitation and evaporation. Forcing with satellite derived precipitation instead of NWP model derived precipitation will likely lead to an improvement in the model ocean salinity.

3) The widening of the Indo-Sri Lanka channel leads to errors in the representation of currents in the model, which, in turn, caused large errors in the salinity filed, particularly in the southeastern Arabian Sea. According to earlier studies, *Rao and Sivakumar* [1999] and *Kurian and Vinayachandran* [2007], this is the region where a "mini" warm pool forms during the spring, which plays a significant role in the progress of the monsoon and the formation of the monsoon onset vortex [*Rao and Sivakumar, 1999; Shenoi et al.,* 1999]. A poor representation of the salinity field in

this region can disrupt the thermohaline structure of model. One of the primary objectives of this ocean analysis is to provide ocean initial conditions for the coupled model, which will be used for monsoon forecasts. These forecasts are likely proven to be sensitive to the ocean heat content in the Arabian Sea. Our analysis strongly recommends the closing of the Indo-Sri Lanka channel for a better representation of the thermohaline structure in the SEAS.

4) In the GODAS-MOM the top level (5 m) of the model temperature is strongly relaxed using daily Reynolds SST [*Reynolds et al.*, 2007]. Figure 7.1 shows the statistical analysis of SST derived from NCEPEXP (MSST) and Reynold SST (RSST) with respect to TMIAMSRE (TSST). Figure shows that there are isolated cool, -0.3ºC (warm, 0.3ºC) bias between the RSST and TSST particularly in the thermocline ridge region (Oman coast). The model shows relatively more bias with respect to TSST particularly in these two locations. In addition, the correlation between RSST and TSST clearly reflects the pattern of correlation between MSST and TSSST. One reason for a weaker correlation (although it is still greater than 0.6) between RSST and TSST in the equatorial belt must be due to the large rainfall activity in the Eastern Equatorial IO. The Figure 7.2 shows the average (2004-2008) value of the OLR in the Tropical Indian Ocean. It is interesting to note that relatively large convective activity in the Eastern Equatorial IO must create differences in the SST retrievals between RSST and TSST, since the former depends primarily on AVHRR (infrared band) and latter depends on the microwave band. Microwaves can "see" through the clouds while the infrared cannot [*Wentz et al.,* 2000]. It is in the EEIO region that RSST and TSST show a relatively large RMSD. This could be one cause of the poor correlations between the model and the observations (left panel) in Figure 7.1. We have to do more analysis, such as compare RSST with TSST and RAMA SST and gain more insight into which is the better product, so that product can be used in the GODAS-MOM.

We have relaxed the model to the Reynolds SST and it must have created differences in the above mentioned areas (Eastern Equatorial IO , Oman coast, thermocline ridge region) with respect to TMIAMSRE SST). In short, we should conduct an experiment where we relax the model to TMIAMSRE SST.

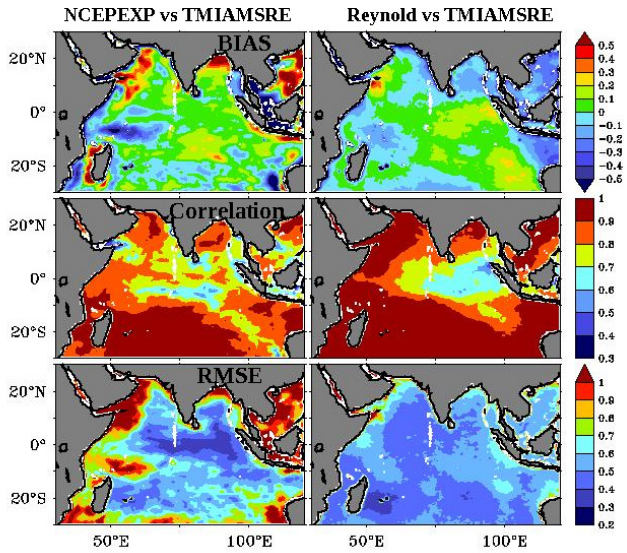

Figure 7.1. Bias (ºC) (top), Correlation (middle) and RMSE (ºC) (bottom) between NCEPEXP & TMIAMSRE and Reynolds SST & TMIAMSRE.

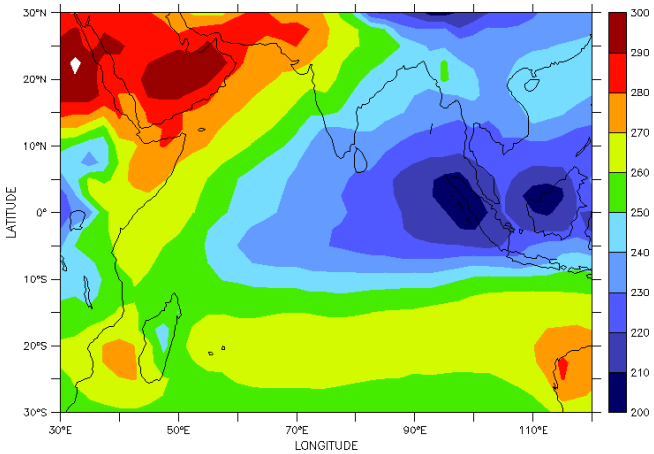

Figure 7.2. Outgoing longwave radiation (W m^{-2}) averaged during 2004-2008.

5) *Papa et al.* [2010] developed a technique to retrieve the river discharge rate from altimetry by regressing the altimetry derived river water height on the observed river discharge. For periods when *in situ* observations are not available (2003-2008), the

regression curves provide the means for estimating discharge rates. Their comparison of estimated river discharge rates with observed values shows a reasonably good agreement. Studies shown large interannual variations in river discharge from the Ganga-Brahmaputra, emphasizing the importance of forcing the model with interannual river discharge rates instead of annual or seasonal rates to achieve a better simulation of the salinity field in the Bay of Bengal.

6) The analysis suggests that a higher resolution model would improve the simulation of small scale eddy activity at higher latitudes and consequently the current field.

7) In agreement with earlier studies, our analysis shows that there are considerable improvements in the current field, when the model is forced with QuikSCAT winds instead of NCEP2 momentum fluxes. Unfortunately, after November 2009, the QuikSCAT wind data were no longer available. A new scatterometer, the Advanced SCATterometer (ASCAT) onboard the MetOp-A satellite, provides surface wind speed and direction over the global ocean with a spatial resolution of 25 km. A study by *Bentamy* [2008] shows that the ASCAT winds are reasonably skilful at resolving surface winds over the ocean surface (RMSE of magnitude and direction is around 2 m s^{-1} and 20° respectively). This data set is continuously available from 17 October 2007 onwards. The GODAS-MOM forcing with ASCAT wind should improve the ocean analysis, especially the surface currents.

8) It is well known that there are significant errors in the NCEP2 heat flux, which will contribute to errors in the model SST [*Sun et al.,* 2009*; Swain et al.,* 2009; *Mcphaden et al,* 2009]. Forcing the model with the recently developed heat flux data TropFlux [*Praveen kumar et al.,* 2011] or OA flux [*Yu,* 2007], which have better accuracy, may provide better oceanic conditions.

9) A systematic effort could be made to reduce the systematic bias in the model state by modifying the background viscosity.

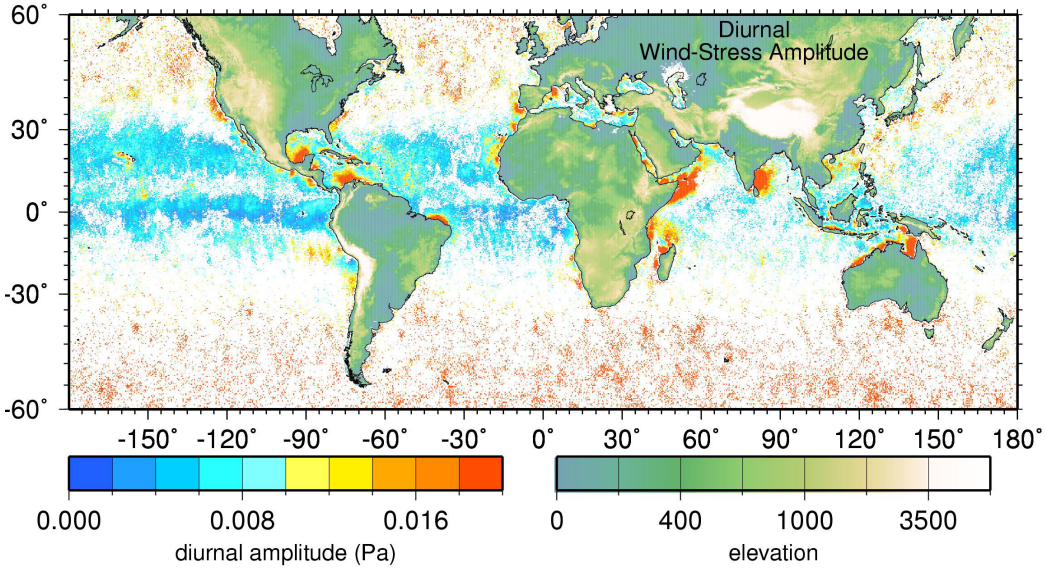

Figure 7.2. Strength of diurnal wind cycle, with major axis plotted in color in locations where it is statistically significant. Adapted from Gille et al. [2005].

10) Figure 7.2 shows the amplitude of the diurnal wind stress from *Gille et al.* [2005]. The figure shows that statistically significant diurnal wind variations occur along coastlines all over the world, they are commonly referred to as the land/sea breeze. A study by *Hunter et al.* [2007] showed that such diurnal winds forced significant motions in the coastal ocean. Open ocean winds also undergo substantial diurnal variability in tropics (between 30°S to 30°N). It is expected that they would play a role in mixed layer dynamics. *Lee et al.* [2005] showed the effects of high-frequency wind sampling in a near-global ocean model. They forced the model first with a 12-hourly averaged wind product and then, in a separate experiment, with winds sub-sampled from the same product at 24 hourly intervals. Their study showed that, in tropical and coastal regions, the changes in upper ocean structure due to the wind forcing was primarily caused by the differences in advection resulting from aliasing in the annual mean wind, which varies according to the sub-sampling strategy. These studies indicate the importance of forcing the model with diurnal winds. At present, for high

frequency wind data, we have only the output of NWP models. However, the diurnal signal in the NWP wind field will have to be studied carefully before employing them in the ocean analysis.

11) The GODAS-MOM assimilates temperature and synthetic salinity profiles obtained from in-situ observations. By assimilating sea surface height anomalies as well, the ocean analysis will greatly improve its representation of the ocean state.

12) At present, GODAS assimilates observed temperature and synthetic salinity based on the local climatological temperature and salinity correlation. The assimilation of observed salinity will improve significantly the ocean analysis.

Acknowledgment

The encouragement and facilities provided by the Director, INCOIS are gratefully acknowledged. This report was possible due to MoU between MoES & NOAA. We sincerely thank Dr. Shailesh Nayak, Secretary, MoES for making "Ocean Data Assimilation" as one of the implementation agreement between INCOIS and NCEP. We thank Dr. Hasibur Rahaman, INCOIS for his fruitful suggestions and comments, which helped in improving the manuscript. Thanks are also due to Dr. A. Suryachandra Rao, IITM and Dr. P.S. Swati, CMMACS for their valuable comments. The GODAS experiments are designed and ran on INCOIS-High erformance computing machine. Authors thank INCOIS-HPC team for their timely help in porting the model. Special thanks to Raju Devender for making GODAS-MOM outputs on Live Access Server. Graphics are generated using Ferret.

References

Agarwal, N., R. Sharma, S. Basu, A. Sarkar, and V. K. Agarwal (2008), Evaluation of relative performance of QuikSCAT and NCEP re-analysis winds through simulations by an OGCM, *Deep Sea Res., I.* 54(8), 1311–1328.

AVISO, Ssalto/Duacs User Handbook (2009), (M)SLA and (M)ADT Near-Real Time and Delayed Time Products. Reference, CLS-DOS-NT-06.034, AVISO Altimetry, France, 51.

Balmaseda, B. A., O.J. Alves, A. Arribas, T. Awaji, D.W. Behringer, N. Ferry, Y. Fujii, T. Lee, M. Rienecker, T. Rosati, and D. Stammer (2009), Ocean Initialization for Seasonal Forecasts, *Oceanography,* 22, 3, 154–159.

Balmaseda, M.A., and D. Anderson (2009), Impact of initialization strategies and observations on seasonal forecast skill, *Geophys. Res. Lett.,* 36, L01701, doi:10.1029/2008GL035561.

Behringer, D.W., M. Ji, and A. Leetmaa (1998), An improved coupled model for ENSO prediction and implications for ocean initialization. Part I: The ocean data assimilation system, *Mon. Wea. Rev*., 126, 1013-1021.

Behringer, D. W. (2007), The Global Ocean Data Assimilation System at NCEP, paper presented at the 11th Symposium on Integrated Observing and Assimilation Systems for Atmosphere, Oceans, and Land Surface, *Am. Meteorol. Soc.,* San Antonio, Tex.

Bentamy, A. (2008) Characterization of ASCAT measurements based on buoy and QuikSCAT wind vector Observations, *Ocean Sci. Discuss.,* 5, 77–101.

Bonjean, F., and G. S. E. Lagerloef (2002), Diagnostic model and analysis of the surface currents in the tropical Pacific Ocean, *J. Phys. Oceanogr.,* 32, 2938-2954.

Carton, J. A., and A. Santorelli (2008), Global Decadal Upper-Ocean Heat Content as

Viewed in Nine Analyses, *J. Climate*, 21, 6015–6035. doi: 10.1175/2008JCLI2489.1

Chelton, D. B., M. G. Schlax, M. H. Freilich, and R. F. Milliff, (2004), Satellite measurements reveal persistent small-scale features in ocean winds, *Science*, 303, 978–983.

Cutler A. N., and J. C. Swallow (1984), Surface currents of the Indian Ocean (to 25°S, 100°E), *I.O.S. Tech. Rept. 187*

de Boyer Montégut, C., J. Vialard, S. S. C. Shenoi, D. Shankar, F. Durand, C. Ethé, and G. Madec (2007), Simulated seasonal and interannual variability of mixed layer heat budget in the northern Indian Ocean, *J. Climate*, 20, 3249-3268.

Derber, J., and A. Rosati (1989), A global oceanic data assimilation system, *J. Phys. Oceanogr.,* 19, 1333–1347, doi:10.1175/1520-0485.

Dong, Changming and Lie-Yauw Oey (2005), Sensitivity of Coastal Currents near Point Conception to Forcing by Three Different Winds: ECMWF, COAMPS, and Blended SSM/I–ECMWF–Buoy Winds, *J. Phys. Oceanogr.,* 35, 1229–1244.

Emery, W. J., and R. E. Thomson (1998), Data analysis methods in physical Oceanography, Pergamon, Kidlington, U.K.

Fairall, C. W., E. F. Bradley, J. E. Hare, A. A. Grachev, J. B. Edson (2003), Bulk Parameterization of Air–Sea Fluxes: Updates and Verification for the COARE Algorithm. *J. Climate*, 16, 571–591.

Francis. P.A., S. Gadgil (2009), The aberrant behaviour of the Indian monsoon in June 2009, *Curr. Sci.,* Vol. 97, No.9.

Fu, L. L. and A. Cazenave (2001), Satellite altimetry and Earth sciences, A Handbook of 503 techniques and applications, *International Geophysics Series,* 69, Academic, San 504 Diego.

Gadgil, S., and J. Srinivasan (2011), Seasonal prediction of the Indian monsoon, *Curr. Sci.,* 100, 3, 2011.

Gille, S. T., S. G. Llewellyn Smith, and N. M. Statom (2005) Global observations of the land breeze, *Geophys. Res. Lett.,* 32(5). L05605, 10.1029/2004GL022139.

Goswami, B N, and D. Sengupta (2003), A Note on the Deficiency of NCEP/NCAR Reanalysis Surface Winds over the Equatorial Indian Ocean, *J. Geophys. Res.,* 108(C4), 3124, doi:10.1029/2002JC001497.

Griffies, S., A. Gnanadesikan, R.C. Pacanowski, V. D. Larichev, J. K. Dukowicz, and R. D. Smith (1998), Isoneutral diffusion in a z-coordinate ocean model, *J. Phys. Oceanogr.*, 28(5), 805-830.

Griffies, S., and R. W. Hallberg (2000), Biharmonic friction with a Smagorinsky-like viscosity for use in large-scale eddy-permitting ocean models, *Mon. Weather Rev.,* 128, 8, 2935-2946.

Griffies, S. M., M. J. Harrison, R. C. Pacnowski, and A. Rosati (2004), A technical Gudie to MOM$, GFDL ocean Group Technical Report No. 5, NOAA/Geophysical Fluid Dynamics Laboratory, available online at www.gfdl.noaa.gov/~fms.

Huang, R. X., and S. Russell (1994), Ventilation of the subtropical North Pacific, *J. Phys. Oceanogr.,* 2, 2589-2605,

Huang, B., Y. Xue, and D. W. Behringer (2008), Impacts of Argo salinity in NCEP Global Ocean Data Assimilation System: The tropical Indian Ocean, *J. Geophys. Res.,* 113, C08002, doi:10.1029/2007JC004388.

Hunter, E., R. Chant, L. Bowers, S. Glenn, and J. Kohut (2007), Spatial and temporal variability of diurnal wind forcing in the coastal ocean, *Geophys. Res. Lett.,* 34, L03607, doi:10.1029/2006GL028945.

Iskandar, I., W. Mardiansyah, Y. Masumoto, and T. Yamagata (2005), Intraseasonal Kelvin waves along the southern coast of Sumatra and Java, *J. Geophys. Res.,* 110, C04013, doi: 10.1029/2004JC002508

Iskandar, I., Y. Masumoto, and K. Mizuno (2009), Subsurface equatorial zonal current in the eastern Indian Ocean, *J. Geophys. Res.,* 114, C06005, doi:10.1029/2008JC005188.

Jiang, C., L. Thompson, and K. Kelly (2008), Equatorial influence of QuikSCAT winds in an isopycnal ocean model compared to NCEP2 winds, *Ocean Modell.,* 24, 65–71, doi:10.1016/j.ocemod. 2008.05.003.

Joseph, P. V., K. P. Sooraj, C. A. Babu, and T. P. Sabin (2005), A cold pool in the Bay of Bengal and its interaction with the active-break cycle of the monsoon, *CLIVAR Exchanges*, 34, 10(3), 10– 12.

Johnson, E. S., F. Bonjean, G. S. E. Lagerloef, J. T. Gunn, and G. T. Mitchum (2007), Validation and error analysis of OSCAR sea surface currents, *J. Atmos. Oceanic Technol.,* 24, 688–701.

Kanamitsu, M., W. Ebisuzaki, J. Woollen, S. K. Yang, J. J. Hnilo, M. Fiorino, and G. L. Potter (2002), NCEP-DOE AMIP-II reanalysis (R-2), *Bull. Amer. Meteor. Soc.,* 83, 1631–1643.

Kang, I., and J. Kug (2000), An El-Nino Prediction System using an intermediate ocean and a statistical atmosphere, *Geophys. Res. Lett.,* 27(8), 1167–1170.

Kara, A. B., P. A. Rochford and H. E. Hurlbutt (2000a), Mixed layer depth variability and barrier layer formation over the North Pacific Ocean, *J. Geophys. Res.,* 105, C7, 16,783-16,801.

Kara, A. B., P. A. Rochford, and H. E. Hurlburt (2000b), An optimal definition for ocean mixed layer depth, *J. Geophys. Res.*, 105(C7), 16, 803–16, 821.

Kessler, W. S. (1990), Observations of long Rossby waves in the northern tropical Pacific, *J. Geophys. Res.,* 95:5183–5217.

Knauss, J. A., and B. A. Taft (1964), Equatorial undercurrent of the Indian Ocean, *Science,* 143, 354–356.

Lagerloef, G. S. E., G. Mitchum, R. Lukas and P. Niiler (1999), Tropical Pacific near-surface currents estimated from altimeter, wind and drifter data, *J. Geophys. Res.,* 104, 23,313-23,326.

Large W.G., J. C. McWilliams and S. C. Doney (1994), Oceanic vertical mixing: a review and model with a nonlocal boundary layer parameterization, *Rev. Geophys.,* 32, pp. 363–403.

Lee, T., and W. T. Liu (2005), Effects of high-frequency wind sampling on simulated mixed layer depth and upper ocean temperature, *J. Geophys. Res.,* 110, C05002, doi:10.1029/2004JC002746.

Li, X., C. Yi, J. C. McWilliams, L.L. Fu (2001), A Comparison of Two Vertical-Mixing Schemes in a Pacific Ocean General Circulation Model, *J. Climate,* 14, 1377–1398. doi: 10.1175/1520-0442

Locarnini, R. A., A. V. Mishonov, J. I. Antonov, T. P. Boyer, H. E. Garcia, O. K. Baranova, M. M. Zweng, and D. R. Johnson (2010), World Ocean Atlas 2009, Volume 1: Temperature. S. Levitus, Ed. NOAA Atlas NESDIS 68, U.S. Government Printing Office, Washington, D.C., 184 pp.

Lumpkin, R. and Z. Garraffo (2005), Evaluating the Decomposition of Tropical Atlantic Drifter Observations, *J. Atmos. Oceanic. Techn.,* I 22, 1403-1415

Masson, S., P. Delecluse, J.-P. Boulanger, and C. Menkes (2002), A model study of the seasonal variability and formation mechanisms of the barrier layer in the eastern equatorial Indian Ocean, *J. Geophys. Res.*, 107(C12), 8017, doi:10.1029/2001JC000832.

McPhaden, M. J; G. Meyers, K. Ando, Y. Masumoto, V. S. N. Murty, M. Ravichandran, F. Syamsudin, J. Vialard, L. Yu, and W. Yu (2009), RAMA The Research Moored Array for African–Asian–Australian Monsoon Analysis and Prediction A new moored buoy array in the historically data-sparse Indian Ocean provides measurements to advance monsoon research and forecasting, *Bull. Amer. Meteorol. Soc.,* 90, pp 459-480 doi:10.1175/2008BAMS2608.1.

Momin, I.M. Agarwal, N. Sharma, R. Basu, S. Agarwal, V.K (2010), Impact of Satellite-Derived Precipitation on Simulated Sea-Surface Salinity in the Tropical Indian Ocean, *IEEE Geosci. Remote Sens. Lett.* 4, doi: 10.1109/LGRS.2010.2043921.

Murray, R.J. (1996), Explicit generation of orthogonal grids for ocean models, *J. Comput. Phys.,* 126, 251-273.

Murty, V. S. N., A. Suryanarayana, M. Sarma, V. Tilvi, V. Fernando, G. Nampoothiri, A. Sardar, D. Gracias, and S. Khalap (2002), First results of Indian current meter moorings along the equator: Vertical current structure variability at equator, 93°E during February–December 2000, 1*, paper presented at 6th Pan Ocean Remote Sensing Conference,* Natl. Aeronaut. and Space Admin., Bali, Indonesia.

Nanjundiah, R. S. (2009), A quick look into assessment of forecasts for the Indian summer monsoon rainfall in 2009, CAOS Report, CAOS, IISc, Bangalore, October.

NOAA (1988), Data Announcement 88-MGG-02, Digital relief of the Surface of the Earth. NOAA, National Geophysical Data Center, Boulder, Colorado, 1988.

Pacanowski, R. C. and S. M. Griffies (1998), MOM 3.0 Manual, NOAA/Geophysical Fluid Dynamics Laboratory, Princeton, USA.

Papa, F., F. Durand, W. B. Rossow, A. Rahman, and S. K. Bala (2010), Satellite altimeter-derived monthly discharge of the Ganga-Brahmaputra River and its

seasonal to interannual variations from 1993 to 2008, *J. Geophys. Res.*, 115, C12013, doi:10.1029/2009JC006075.

Parekh, A., A. Sarkar, S. Shah, and M. S. Narayanan (2004), Low period variability in Tropical Rainfall Measuring Mission Microwave Imager measured sea surface temperature over the Bay of Bengal during summer monsoon, *Curr. Sci.*, *87*(6), 791–795.

Pond, S., and G. L. Pickard (1983), Introductory dynamical oceanography (2nd ed.). Oxford: *Pergamon Press.*

Prasad T. G., and M. Ikeda (2001), Spring evolution of Arabian Sea High in the Indian Ocean, *J. Geophys. Res.*, 106, 31085–31098.

Praveen Kumar B., J. Vialard, M. Lengaigne ,V.S.N. Murty and M. J. McPhaden (2011), TropFlux: Air-Sea Fluxes for the Global Tropical Oceans – Description and evaluation against observations, *Clim. Dyn.,* in press.

Rajeevan, M., and L. Sridhar (2008), Interannual relationship between Atlantic sea surface temperature anomalies and Indian summer monsoon, *Geophys. Res. Lett.,* 35, L21704, doi:10.1029/2008GL036025.

Rao, R. R., and R. Sivakumar (1999), On the possible mechanisms of the evolution of a mini-warm pool during the pre-summer monsoon season and the onset vortex in the southeastern Arabian Sea, *Q. J. R. Meteorol. Soc.*, *125*(555 Part A), 787–809

Rao, R. R., and R. Sivakumar (2003), Seasonal variability of sea surface salinity and salt budget of the mixed layer of the north Indian Ocean, *J. Geophys. Res.*, 108(C1), 3009, doi:10.1029/2001JC000907.

Rao, R. R., M. S. Girish Kumar, M. Ravichandran, B. K. Samala, and G. Anitha (2006a), Observed intraseasonal variability of mini-cold pool off the southern tip of India and its intrusion into the south central Bay of Bengal during summer monsoon season, *Geophys. Res. Lett.*, *33*, L15606, doi:10.1029/2006GL026086.

Rao, R. R., M. S. Girish Kumar, M. Ravichandran, B. K. Samala, and N. Sreedevi (2006b), Observed mini-cold pool off the southern tip of India and its intrusion into the south central Bay of Bengal during summer monsoon season, Geophys. *Res. Lett.,* 33, L06607, doi:10.1029/2005GL025382.

Rao. R. R, M. S. GirishKumar, M. Ravichandran, A.R.Rao, V. V..Gopalakrishna P. Thadathil (2010), Interannual variability of Kelvin wave propagation in the wave guides of the equatorial Indian Ocean, the coastal Bay of Bengal and the southeastern Arabian Sea during 1993–2006, *Deep-Sea Res., I*, 57, 1–13, doi:10.1016/j.dsr.2009.10.008.

Rao, R. R., M. S. Girish Kumar, M. Ravichandran, V.V.Gopalakrishna and P.Thadathil (2011), Is the low salinity waters pass through the Indo-Sri Lanka Channel during winter?, *Int. J. Remote Sens.,* doi: 10.1080/01431161.2010.

Rao, S. A., J. J., Luo, S. K., Behera, T., Yamagata (2008), Generation and termination of Indian Ocean dipole events in 2003, 2006 and 2007, *Clim. Dyn.,* DOI:10.1007/s00382-008-0498-z.

Reppin, J., F. A. Schott, J. Fischer, and D. Quadfasel (1999), Equatorial currents and transports in the upper central Indian Ocean: Annual cycle and interannual variability, *J. Geophys. Res.,* 104, 15,495– 15,514.

Reynolds, R. W., T. M. Smith, C. Liu, D. B. Chelton, K. S. Casey and M. G. Schlax (2007), Daily high-resolution blended analyses for sea surface temperature, *J. Clim.,* 20, 5473-5496.

Saha S., and co-authors (2010), The NCEP Climate Forecast System Reanalysis, *Bull. Amer. Meteorol. Soc.,* 91, 8, doi: 10.1175/2010BAMS 3001.2.

Sakova, I. V., G. Meyers, and R. Coleman (2006), Interannual variability in the Indian Ocean using altimeter and IX1-expendable bathy-thermograph (XBT) data:

Does the 18-month signal exist?, *Geophys. Res. Lett.,* 33, L20603, doi:10.1029/2006GL027117

Schott, F. A., S.-P. Xie, and J. P. McCreary Jr. (2009), Indian Ocean circulation and climate variability, *Rev. Geophys.*, 47, RG1002, doi:10.1029/2007RG000245.

Senan, R., D. S. Anitha, and D. Sengupta, (2001), Validation of SST and wind speed from TRMM using north Indian Ocean moored buoy observations, *CAOS Report* 2001AS1, 30, [http://caos.iisc.ernet.in/hpg/students/retish.html].

Sengupta, D., and M. Ravichandran (2001), Oscillations in the Bay of Bengal sea surface temperature during the 1998 summer monsoon, *Geophys. Res. Lett.*, *28*, 2033–2036.

Sengupta, D., R. Senan, V. S. N. Murty, and V. Fernando (2004), A biweekly mode in the equatorial Indian Ocean, *J. Geophys. Res.,* 109, C10003, doi:10.1029/2004JC002329

Shankar, D., and S.R. Shetye (1997), On the dynamics of the Lakshadweep high and low in the southeastern Arabian Sea, *J. Geophys. Res.,* 102 (C6), 12,551–12,562.

Shankar, D., P. N. Vinayachandran, and A. S. Unnikrishnan (2002), The monsoon currents in the north Indian Ocean, *Prog. Oceanogr.,* 52(1), 63– 120.

Shankar, D., S. R. Shetye, and P. V. Joseph (2007), Link between convection and meridional gradient of sea surface temperature in the Bay of Bengal, *J. Earth Syst. Sci.,* 116, 385–406.

Sharma, R. N., S. Agarwal, S. Basu, and V. K. Agarwal (2007), Impact of satellite derived forcings on numerical ocean model simulations and study of sea surface salinity variations in the Indian Ocean, *J. Clim.,* 20:871–890.

Shenoi, S. S. C., D. Shankar, and S. R. Shetye (1999), On the sea surface temperature high in the Lakshadweep Sea before the onset of the southwest monsoon, *J. Geophys. Res.*, 104(C7), 15,703–15,712, doi:10.1029/1998JC900080.

Shenoi, S. S. C., D. Shankar, and S. R. Shetye (2002), Difference in heat budgets of the near-surface Arabian Sea and Bay of Bengal: Implications for the summer monsoon*, J. Geophys. Res.,* 107(C6), 3052, doi:10.1029/2000JC000679.v.

Shetye, S. R., A. D. Gouveia, D. Shankar, S. S. C. Shenoi, P. N. Vinayachandran, D. Sundar, G. S. Michael, and G. Nampoothiri (1996), Hydrography and circulation in the western Bay of Bengal during the northeast monsoon, *J. Geophys. Res.,* 101, 14,011– 14,025.

Smagorinsky, J. (1963), General circulation experiments with the primitive equations: I. The basic experiment, *Mon. Wea. Rev.*, 91, 99-164.

Smith, W. H. F., and D. T. Sandwell (1997), Global Seafloor Topography from Satellite Altimetry and Ship Depth Soundings, *Science,* 277, 1956–1962

Smith, S. R., D. M. Legler, and K. V. Verzone (2001), Quantifying uncertainties in NCEP reanalyses using high quality research vessel observations, *J. Clim.,* 14, 4062–4072.

Sun, B., L. Yu and R. Weller (2003), Comparisons of Surface Meteorology and Turbulent Heat Fluxes over the Atlantic NWP Model Analyses versus Moored Buoy Observations, *J. Clim.,*,16, pp 679-695.

Swain, D and S. H. Rahman, and M. Ravichandran (2009), Comparison of NCEP turbulent heat fluxes with in situ observations over the south-eastern Arabian Sea, Meteorol. *and Atmos. Phy*., 104 (3-4). pp. 163-175. ISSN 0177-7971.

Taylor, K.E. (2001), Summarizing multiple aspects of model performance in a single diagram, *J. Geophys. Res.,* 106 (D7), 7183-7192.

Vecchi, G. A., and D. E. Harrison (2002), Monsoon breaks and subseasonal sea surface temperature variability in the Bay of Bengal, *J. Clim.,* 15, 1485– 1493.

Vialard, J., S. S. C. Shenoi, J. P. McCreary, D. Shankar, F. Durand, V. Fernando, and S. R. Shetye (2009), Intraseasonal response of the northern Indian Ocean coastal

waveguide to the Madden-Julian Oscillation, *Geophys. Res. Lett.,* 36, L14606, doi:10.1029/2009GL038450.

Vinayachandran, P. N., Y. Masumoto, T. Mikawa, and T. Yamagata (1999), Intrusion of the Southwest Monsoon Current into the Bay of Bengal, *J. Geophys. Res.,* 104(C5), 11,077– 11,085.

Vinayachandran, P. N., T. Kagimoto, Y. Masumoto, P. Chauhan, S. R. Nayak, and T. Yamagata (2005), Bifurcation of the East India Coastal Current east of Sri Lanka, *Geophys. Res. Lett.,* 32, L15606, doi:10.1029/ 2005GL022864.

Vinayachandran, P. N., and N. H. Saji (2008), Mechanisms of South Indian Ocean intraseasonal cooling, *Geophys. Res. Lett.*, 35, L23607, doi:10.1029/2008GL035733.

Vörösmarty, C. J., B. Fekete, and B. A. Tucker (1996), River discharge database, Version 1.0 (RivDIS v1.0), Volumes 0 through 6. A contribution to IHP-V Theme: 1. Technical documents in hydrology series, Tech. Rep., UNESCO, Paris.

Wentz, F. J., C. L. Gentemann, D. K. Smith and D. B. Chelton (2000), Satellite Measurements of Sea Surface Temperature Through Clouds, *Science,* 288(5467), 847-850.

Wentz, F.J., D. K. Smith, C. A. Mears, and C. L. Gentemann (2001), Advanced algorithms for QuikSCAT and SeaWinds/AMSR, *Geoscience and Remote Sensing Symposium, IEEE 2001 International*, vol. 3, pp. 1079–1081, doi:10.1109/IGARSS.2001.976752, Inst. Of Electr. and Electr. Eng., New York.

Wyrtki, K. (1973), An equatorial jet in the Indian Ocean, *Science*, Vol. 181, pp. 262-264.

Yang, J. L. Yu, C. J. Koblinsky, D. Adamec (1998), Dynamics of the seasonal variations in the Indian Ocean from TOPEX/POSEIDON sea surface height and an ocean model, *Geophys. Res. Lett.,* 25, 1915-1918.

Yu, L. (2003), Variability of the depth of the 20°C isotherm along 6°N in the Bay of Bengal: its response to remote and local forcing and its relation to satellite SSH variability, *Deep-Sea Res.-II,* 50, pp. 2285–2304, doi:10.1016/S0967-0645(03)00057-2.

Yu, L., and R. A. Weller (2007), Objectively Analyzed air-sea heat Fluxes for the global ocen-free oceans (1981–2005), *Bull. Ameri. Meteor. Soc.,* 88, 527–539.